Wave spectral evolution in shallow and intermediate waters at select coastal regions of India

A THESIS SUBMITTED IN PARTIAL FULFILLMENT FOR THE DEGREE OF

DOCTOR OF PHILOSOPHY

IN THE SCHOOL OF EARTH, OCEAN AND ATMOSPHERIC SCIENCES

GOA UNIVERSITY

By

Anjali Nair M

Ocean Engineering Division
CSIR- National Institute of Oceanography
Donapaula-403004, Goa, India

JULY 2022

DECLARATION

I, Anjali Nair M hereby declare that this thesis represents work which has been carried out by me and that it has not been submitted, either in part or full, to any other University or Institution for the award of any research degree.

Place: Taleigao Plateau.
Date : 29-07-2022

Anjali Nair M

CERTIFICATE

I hereby certify that the above Declaration of the candidate, Anjali Nair M is true and the work was carried out under my supervision.

Dr. V Sanil Kumar
(Research Guide)
Chief Scientist & Head
Ocean Engineering Division
CSIR – National Institute of Oceanography
Dona Paula 403 004, Goa

Acknowledgements

At this stage of earning a doctoral degree, I would like to thank people who have been there with me as constant support. Here is my note of gratitude and love to those people; without them, this wouldn't have been possible.

First and foremost, I would like to express my deep gratitude to Dr. V. Sanil Kumar, my research supervisor, for his valuable guidance, encouragement, and patience throughout the journey. His subject knowledge and experience in this field have helped me to come up with a good number of publications during this period. I appreciate the valuable time, ideas, and motivation he has provided for my Ph.D.

My sincere thanks to the doctoral research committee members Prof. (HAG). Harilal B Menon (Dean, School of Earth Ocean and Atmospheric Sciences, Goa University) Dr. P. Vethamony (Retd. Chief Scientist, NIO, Goa) and Dr. M. R Ramesh Kumar (Retd. Chief Scientist, NIO, Goa) for providing valuable comments at various stages of my research work.

I am so thankful to Jai Singh and Dr. Gowthaman, Technical staff, OED, NIO, Goa for their help in collecting wave data required for the study.

I would like to express my gratitude to the present NIO Director Prof. Sunil Kumar Singh, and former NIO Directors S.W.A. Naqwi and Dr. Prasanna Kumar for their support, encouragement, and the facilities of research provided. I wish to express my gratitude to the HRM, Library, and ITG, CSIR NIO for their assistance as and when required. I would like to thank CSIR for the senior research fellowship (SRF), which gave me financial independence during my research career.

I am grateful to the Vice-Chancellor, Goa University, The Dean, School of Earth, Ocean and Atmospheric Sciences, and the other staff for their support to ease the official formalities in the department.

Wave rider buoy data used in the study was collected under the project funded by Indian National Centre for Ocean Information Services (INCOIS). I would like to thank Director, INCOIS, Hyderabad, and Dr. T.M. Balakrishnan Nair, Scientist G, INCOIS, for allowing me to use the data for research work.

I would like to acknowledge the helpful comments and questions from the editors of the journals and anonymous reviewers of manuscripts that form part of this thesis.

I am extremely thankful to my dear friends Shanas, Jishad, Gautham, and Amrutha, who have always helped me to solve my problems regarding programming and modelling. I thank all my friends in the OED lab, Aditi, Naseef, Jesbin, George, Duphrin, Aravind, Neenuja, Athulya, Anoop, Yadhu, and Rajeev, for all the love and support at the workplace. I would like to express my love to our Puttu mess, Swathy, Savio, Adithyan, Sherin, Jeffy, Nikhil, Robin, Azmi, and all other friends at NIO colony for keeping me happy throughout this journey.

Last but not least, I would like to thank my family and my in-laws for being the strong pillar of support throughout this journey. I am forever grateful to my Amma, Achan, and chechi, who always believed in me and have been there as my support system. I have no words to thank my Amma, who brought up a shy little introvert child to the confident woman I am today. I express all my love to my dear husband Vineeth for all the love, encouragement, and motivation he has given me and also for listening to all my problems with great patience. I thank God for blessing me with these wonderful people in my life and for being my strength in my lows.

To

Amma and Achan

Abstract

Spectral representation of sea surface waves which can provide information about different wave systems present at a location is an important input in offshore structure design, coastal management studies and climatic studies. In the case of structural design, spectral information is an important input in the estimation of induced loads on marine structures and the response of floating bodies to the wave action. Nowadays third-generation wave models are widely used for the operational forecast of the sea state and wave climate projections. In the case of third generation models for non-stationary computations, the shape of the initial spectra used is default JONSWAP spectra. The evolution of wave spectrum and the spectral shape depends on intricate ocean-atmosphere interaction processes such as exchange of momentum flux between the ocean surface and atmosphere, dissipation due to white-capping, bottom friction and vegetation, and energy spread through non-linear interactions, which determines the shape of the spectrum. The waves off the coastal regions of India are influenced by seasonally reversing monsoon winds, sea-land breeze, and extreme events like tropical cyclones. The wave spectral characteristics off the east and west coasts off India and its evolution during sea-land breeze cycle and tropical cyclones (TC) are studied using measured wave rider buoy data, modelled data, and ECMWF - ERA5 Reanalysis data. Wave spectra obtained off the east and west coasts of India are swell dominated during monsoon, whereas both wind-seas and swells co-exist during the non-monsoon period. The wave spectra obtained are mostly double-peaked except during the monsoon period off the west coast and also it undergoes diurnal and inter-annual variation. The wave spectral slope, which has great importance in ocean remote sensing studies and ocean surface processes studies was considered to be a constant (-4 or -5) in the earlier times. Later with more field observations, the spectral slope was found to be varying, indicating a non-equilibrium nature of surface wind waves in the field. In this study the slope of the wave spectrum observed is -3 during monsoon and -4 (steep) during cyclones. The wave spectral evolution during a sea-land breeze cycle is studied using SWAN (Simulating Waves Nearshore) wave model simulated by winds from the WRF model (Weather Research and Forecasting). Simulated source terms vary according to the intensification and weakening of sea breeze, with energy from wind input having a maximum influence on wave spectra and white-capping having the least during the sea-breeze phase. Whereas during the land-breeze phase, it is only the non-linear interactions responsible for the exchange of energy within the spectrum. The evolution of wave spectra in the near-shore and deep waters during the growth and decay of TC is studied

using the measured wave rider buoy data and ECMWF - ERA5 Reanalysis data during the cyclones PHAILIN and KYARR. The wave system generated due to cyclones reaches the near-shore waters and interacts with the pre-existing swells to form a single-peaked spectrum during cyclones. The waves in the deep waters during cyclones are dominated by the wind-sea, with large waves found in the right quadrant to the TC heading direction. TC generated waves in the deep waters, are mostly young wind-seas with the youngest of waves found in the left quadrants, and the wave-field does not exactly follow the wind field but depends on the velocity of forward motion of TC. The combination of the JONSWAP and Donelan spectrum with modified parameters describes the wave spectrum off the east and west coast of India. But during the cyclone, as the wave spectra observed is steeper towards the high frequency part, Donelan spectra deviates from the measured spectra and the JONSWAP spectrum with modified parameters describes the whole wave spectrum well with high values of Υ (≥ 3).

Contents

List of Tables

List of Figures

Chapter 1: Introduction

1.1 Waves

The wind-driven waves on the ocean surface are one of the most important phenomena observed on earth, which has a significant role in various fields like fishing, shipping, recreation, offshore structure design, coastal management, climatic studies, etc. These waves can be generated by various forcing mechanisms such as pressure fluctuations induced by winds, earthquakes, and the gravitational force between the earth and other celestial bodies. Ocean surface waves are classified into different types based on their periodicity, and it ranges from tiny ripples to long period tides and tsunamis (Munk, 1951). Among these, the waves having a period between 1 to 30s are called gravity waves, for which the restoring force acting is gravity. Wind-generated gravity waves are present everywhere on the sea at all the time. These waves are generated somewhere in the ocean and propagate thousands of kilometres away from the wave generation area. Based on that, they are classified into wind-sea and swell. Gravity waves in the generating area are called wind-sea, and the waves travelled out of their generating area are known as swell. The intensity of gravity waves depends on the intensity of wind blowing, duration of the wind, and the area over which the wind blows with a constant speed, otherwise known as fetch (Holhuijsen, 2007). The waves thus generated have their characteristics, such as wave height, wave period, wavelength, and direction. The vertical distance from the top of the crest to the bottom of the trough is called wave height (H). The time interval between the passage of two successive crests or trough through a point is called period (T). Wavelength is the horizontal distance between two consecutive crests or troughs (λ). Wave direction is the angle, with respect to the north, at which the wave approaches the coast.

1.2 History of ocean surface wave study

Wind blowing over the sea surface generates small wavelets, which develop with space and time by absorbing energy from wind and transferring energy among spectral components to form the ocean surface waves. In the early days, the study of ocean surface waves was challenging due to their random properties and complex evolution mechanism. The modern studies on ocean surface waves began in the 1940s with the study of Sverdrup and Munk (1947), who studied the statistical properties of wind waves and introduced significant wave height, which is the statistical mean to describe the random properties of ocean surface waves. In the 1940s, some important studies were conducted by Wuest (1949), Francis

(1949), and Ursell (1956) on the process of wave generation, based on which Philips (1957) and Miles (1957) proposed their major theories. Philips (1957) proposed that pressure fluctuations in the wind resonantly generate wind waves on the water surface, whereas Miles (1957) showed that the coupling between the surface waves and wind generates a special pressure distribution along the wave surface and leads to the exponential growth of the waves. Later, Miles (1960), by combining the theories of Philips (1957) and Miles (1957), showed that the growth of waves is linear in the initial stage and exponential later. After Sverdrup and Munk (1947), the statistical theory of wind waves greatly advanced, and Longuet-Higgins (1952) gave the first theoretical derivation of the statistical distribution of wave heights. It was Pierson (1952) and Neuman (1953) who presented a spectral model for wind waves. Later, Philips (1958) proposed the equilibrium range in the spectrum of wind waves based on a simple consideration of wave breaking. From the end of the 1960s to the 1970s, many experimental studies were done to study the wind wave spectrum, such as the evolution of spectrum (Mitsuyasu 1968,1969; Hasselmann et al., 1973), the spectral form at a finite fetch (Hasselmann et al., 1973), and the similarity form of the directional spectrum (Mistuyasu et al., 1975; Hasselmann et al., 1980; Donelan et al., 1985).

1.3 Ocean wave Spectrum

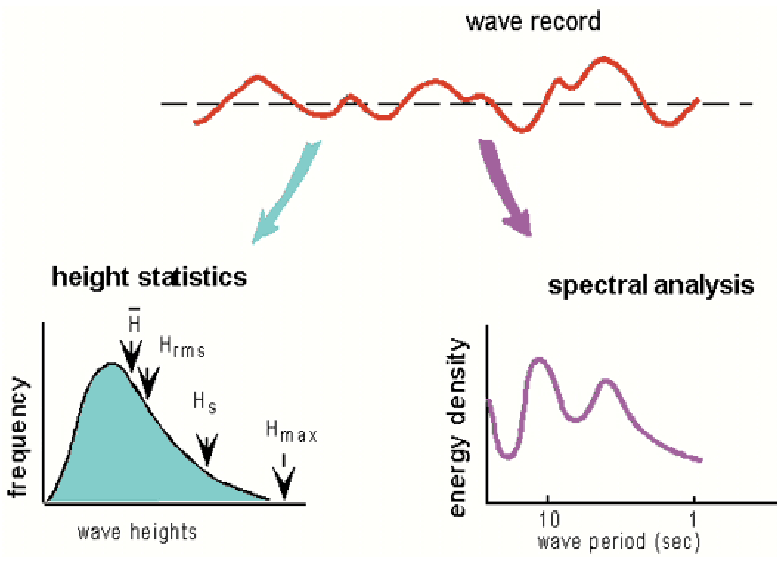

Figure 1.1 A schematic diagram on spectral analysis

Ocean surface is composed of a mixture of irregular and random waves with varying frequencies and amplitude. This poses a challenge in describing the surface. To study more about these waves, it has to be described in a simplified manner. This led to the concept of the ocean wave spectrum. According to this concept, the ocean surface elevation can be obtained as a summation of sine or cosine waves representing different periods, amplitudes, phase, and propagation directions (Sverdrup and Munk, 1947; Pierson, 1952; Neumann, 1953). An ocean wave spectrum can be defined as the distribution of energy at different frequencies. It is calculated using Fourier analysis proposed by Joseph Fourier. According to the Fourier analysis, any function can be approximated over a time interval as the sum of simple sine or cosine functions.

Applying it on the ocean surface waves; if η(t) is the surface elevation measured for the duration [0, T], then it can be decomposed as

$$\eta(t) = a_0 + \sum_1^{\infty}[a_n \cos(n\sigma t) + b_n \sin(n\sigma t)] \quad (1.1)$$

Where the Fourier coefficients a_0, a_n, and b_n are given by

$$a_0 = \frac{1}{T}\int_0^T \eta(t)dt = 0 \quad (1.2)$$

$$a_n = \frac{2}{T}\int_0^T \eta(t)\cos(n\sigma t)\,dt \quad (1.3)$$

$$b_n = \frac{2}{T}\int_0^T \eta(t)\sin(n\sigma t)\,dt \quad (1.4)$$

Here cos(nσt) and sin(nσt) are orthogonal functions over [0,T], where n=1,2,3.. are integers.

'nσ' are harmonics of the fundamental frequency.

$$\sigma = 2\pi f \quad (1.5)$$

f = 1/T is the fundamental frequency.

$$A_n = \sqrt{a_n^2 + b_n^2} \quad (1.6)$$

$$\beta_n = tan^{-1}(b_n, a_n) \quad (1.7)$$

Where A_n is the amplitude of the wave components of the frequency and β_n the related initial phase.

The related energy density of this wave component $E_n = \frac{1}{2}\rho g A_n^2$ (1.8) ‘ρg’ is a constant value, so the energy density in a discrete energy density spectrum is represented by $A_n^2/2$

Hence the resultant wave elevation is given by

$$\eta(t) = A_0 + \sum_1^\infty A_n \cos(n\sigma t - \beta_n) \tag{1.9}$$

1.4 Theoretical wave spectrum

The spectral description of sea-state was introduced during the mid-1950s. Phillips (1958) suggested that, for the deep-water wind waves, there is a region of the spectrum in which the wave energy density has an upper limit and is given by

$$E_m(f) = \alpha g^2 (2\pi)^{-4} f^{-5} \tag{1.10}$$

Where g = acceleration due to gravity, f=frequency, α = constant (8×10^{-3})

This region is called the equilibrium range, beyond which, at each frequency, deep-water wave breaking will occur. That is, the addition of more energy in the spectrum at that frequency will cause wave breaking, and the energy at that frequency will be transferred to other frequency bins through dissipation and wave-wave interactions.

1.4.1 Pierson-Moskowitz spectrum (PM spectrum)

Later, Pierson & Moskowitz (1964) proposed a spectrum for fully developed deep water waves by including the Philips equilibrium range.

$$E_{PM} = E_m \, e^{-5/4 \left(f/f_m \right)^{-4}} \tag{1.11}$$

Where f_m = frequency of spectral peak

The additional term provided the low-frequency forward face of the spectrum and a broad, smooth peak.

f_m can be empirically determined as $f_m = \frac{0.82\, g}{2\pi U}$ (1.12)

To attain a fully developed condition, the wind has to blow for a long time at a constant speed. But at higher wind speed, the wind rarely held steady for the required length of time necessary for the fully developed condition. Also, the fetch over wind the wind is blowing needn't be always long enough to form fully developed seas. These were the major drawbacks of the PM spectra.

1.4.2 JONSWAP spectrum

It was Hasselmann et al. (1973) who extended the PM spectrum to represent a partially developed wave condition or else called a growing sea state. He used the data from Joint North Sea Wave Project (JONSWAP) and modified the PM spectra by adding another factor called the peak enhancement factor. Peak enhancement factor 'γ' defines the ratio of the maximum spectral energy to the maximum spectral energy of the corresponding Pierson-Moskowitz spectrum. The effect of peak enhancement is to increase the peak of the Pierson-Moskowitz spectrum. The JONSWAP spectrum is given by

$$E_J(f) = E_m(f)\, e^{-5/4\left(f/f_m\right)^{-4}}\, \Upsilon^{exp\left(-\left(f/f_m-1\right)^2/2\sigma^2\right)} \quad (1.13)$$

Where $\alpha = 0.076\left(\frac{gX}{U^2}\right)^{0.22}$ (1.14)

$$f_m = 3.5\left(\frac{g}{U}\right)\left(\frac{gX}{U^2}\right)^{-0.33} \quad (1.15)$$

$$\Upsilon = 7.0\left(\frac{gX}{U^2}\right)^{-0.143} \quad (1.16)$$

U = wind speed and X = fetch distance

$\sigma = \sigma_a = 0.07$, for $f_m \geq f$

$\sigma = \sigma_b = 0.09$, for $f_m < f$

The generally recommended values for α and ϒ are α = 0.0081 and ϒ = 3.3.

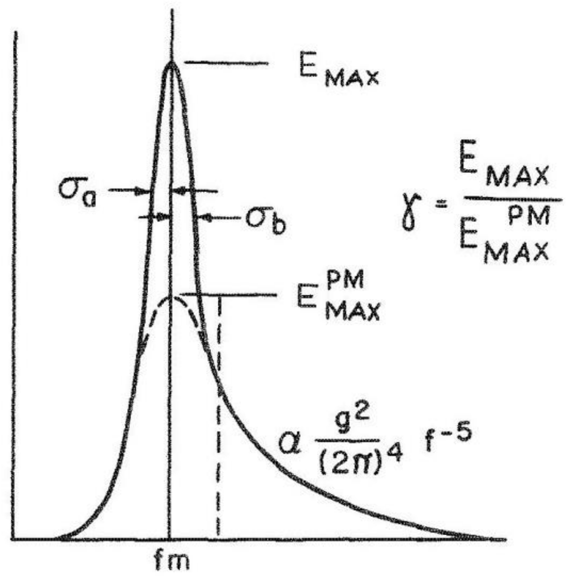

Figure 1.2 Comparison between Pierson-Moskowitz and JONSWAP spectra (Hasselmann et al. 1973)

Wave spectrum in shallow water

Kitaigorodski et al. (1975) introduced a frequency-dependent factor $\phi(2\pi f, h)$ to transform the deep-water equilibrium range $E_m(f)$ to a finite depth equilibrium range. Hence the expression for equilibrium range in shallow water is given by, where 'h' is the water depth.

$$E_m(f,h) = E_m(f)\ \phi(2\pi f, h) \tag{1.17}$$

Thompson and Vincent (1983) gave a simple approximation for $\phi(2\pi f, h)$ which is given by

$$\phi(2\pi f, h) = \frac{1}{2}{\omega_h}^2 \quad \text{for } \omega_h \leq 1 \tag{1.18}$$

$$= 1 - \frac{1}{2}(2-\omega_h)^2 \quad \text{for } \omega_h > 1 \tag{1.19}$$

$$\omega_h = 2\pi f \left(\frac{h}{g}\right)^{1/2} \tag{2.20}$$

1.4.3 TMA Spectrum

Bouws et al. (1985) came up with the first approximation of finite depth wind-sea spectral shape by substituting Kitaigorodski et al. (1975) expression in the JONSWAP spectrum for deep water. He named their finite water depth spectral shape as TMA spectrum after the first three letters of the data sets used for field validation (Texel, MARSEN, and ARSLOE). MARSEN stands for the "Marine Remote Sensing Experiment at the North Sea" and ARSLOE for the "Atlantic Remote Sensing Land-Ocean Experiment." The Texel data set consists of a series of measurements made near the Texel lightship west of Rotterdam during a storm in the North Sea. The TMA spectrum is given as

$$E_{TMA} = \alpha g^2 (2\pi)^{-4}\, \phi(2\pi f, h) e^{-5/4\left(f/f_m\right)^{-4}} \gamma^{exp\left(-\left(f/f_m - 1\right)^2 / 2\sigma^2\right)} \qquad (1.21)$$

Where $\alpha = 0.0078\, k^{0.49}$ (1.22)

$$\gamma = 2.47\, k^{0.039} \qquad (1.23)$$

$$k = \frac{U^2}{g} k_m \qquad (1.24)$$

U = Wind speed at 10m elevation, g = acceleration due to gravity

$k_m = \frac{2\pi}{L_m}$ (Wave number for waves at peak frequency) (1.25)

L_m = wavelength associated with f_m

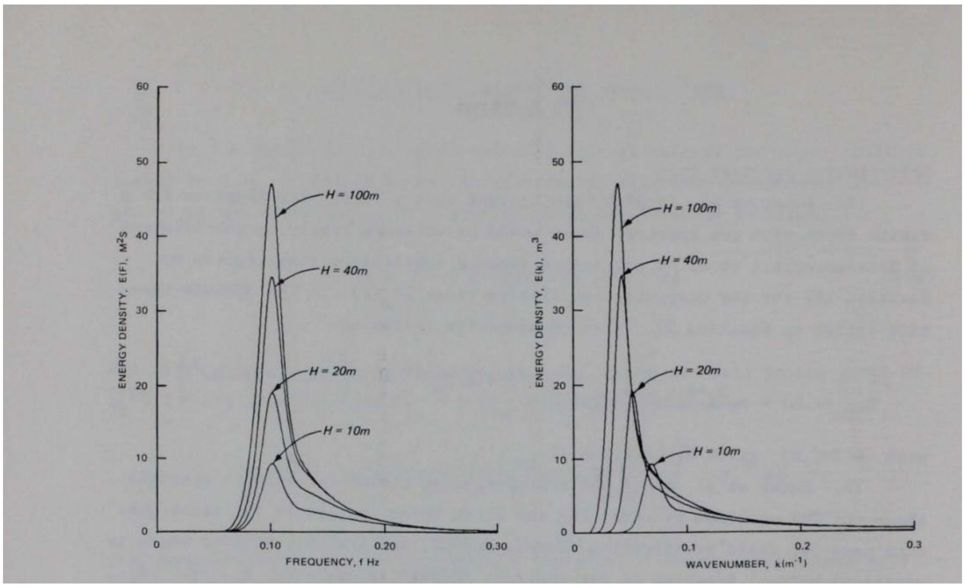

Figure 1.3 TMA spectrum for different water depths (Hughes, 1984)

1.4.4 Donelan Spectrum

Donelan et al. (1985) introduced a revised JONSWAP spectrum by incorporating Toba's formulation (Toba, 1973) as saturation range.

$$S(f) = \alpha g^2 (2\pi)^{-4} f^{-4} f_p \, e^{-5/4 \left(f/f_m\right)^{-4}} \gamma^{exp\left(-\left(f/f_m - 1\right)^2 / 2\sigma^2 f_p{}^2 \right)} \quad (1.26)$$

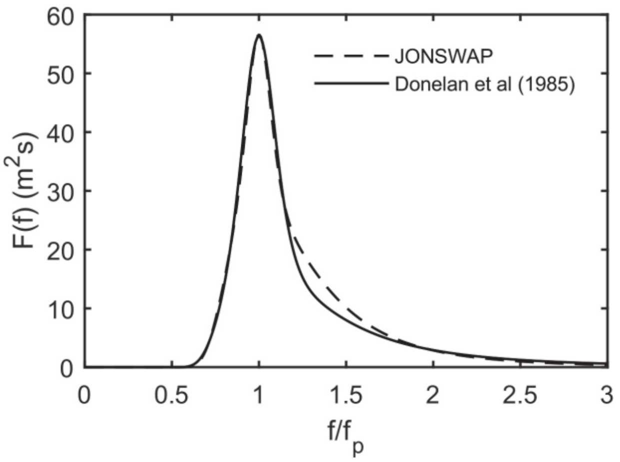

Figure 1.4 Comparison between JONSWAP and Donelan spectrum (Young and Babanin, 2020)

1.5 Background and Motivation

Knowledge of the ocean wave conditions is essential for the design of marine structures as well as climate studies. In the case of marine structures, waves are the most important environmental load which can affect the installation and maintenance of these structures. The greater response of a structure during strong wave conditions like storms can affect its performance or may completely damage the structure. So, for the safe operation of these systems, it is important to know the expected wave loads during different wave conditions and hence the sea state.

The sea-state cannot be explained as a single wave system, as it consists of one or more wind-sea and swell systems (Soares 1991). Earlier, averaged parameters like significant wave height (H_{m02}) and the mean wave period (T_{m02}) were used to describe the sea-states. But in the case of mixed sea states, having both wind-seas and swells, the use of integrated parameters for sea state description will be inappropriate since two wave fields having the same H_{m02} and T_{m02} can be either wind-sea dominated or swell dominated (Holthuijsen 2007; Semedo et al. 2011; Kumar et al. 2014a). This led to the need for the spectral representation of sea states which gives a complete description of the sea surface having waves with different frequencies and directions (Ochi 2005) thus providing information about different wave systems present at a location.

The evolution of waves and the corresponding spectral shape is due to the complex ocean-atmosphere interactions, even though the physics of these interactions are not fully understood yet (Cavaleri et al., 2012). While the wave spectral shape and peak frequency of the wave spectrum are of great importance in Ocean Engineering studies, the spectral nature of the high-frequency part of the wind-generated waves plays a major role in the air-sea interaction and ocean remote sensing studies. The shape of a wave spectrum varies according to the factors affecting the growth and decay of waves. On this basis, several spectral shapes have been proposed for different sea states (Chakrabarti, 2005). These factors include the transfer of energy through non-linear interactions, dissipation due to white capping (Gunson and Symonds 2014), and the momentum flux between the ocean and the atmosphere, which govern the high-frequency wave components of the spectrum (Cavaleri et al., 2012). Non-linear interaction is a process by which energy is redistributed over the spectrum through the exchange of energy between a resonant set of wave components, whereas white-capping is a steepness induced wave breaking process that occurs in deep water when the wave height is much larger than the wavelength. Several studies have discussed the process of white-capping (Ardhuin et al., 2007; Cavaleri et al., 2007; Donelan and Yuan, 1994), but it continues to exist as one of the least understood processes.

As described earlier, so many theoretical wave spectra have been proposed so far with different values of slope for the high-frequency tail of the spectra. For an ocean wave spectrum, peak frequency is defined as the frequency at which spectral energy density is maximum, whereas high frequency region is considered as frequency above 0.2 Hz and low frequency region as frequency below 0.2 Hz (Kitaigorodski et al. 1975). According to Phillips (1985), the equilibrium ranges for the low-frequency ($f < 0.2$ Hz), and high-frequency ($f > 0.2$ Hz) regions are proportional to f^{-5} and f^{-4} (where f is the frequency). Several field studies conducted since the JONSWAP (Joint North Sea Wave Project) field campaign reveal an analytical form for wave spectra with the spectral tail proportional to f^{-4} (Toba, 1973; Kawai et al., 1977; Kahma, 1981; Forristall, 1981; Donelan et al., 1985). Usually, there is a predominance of swell fields in large oceanic areas, which is due to remote storms (Chen et al., 2002; Hwang et al., 2011; Semedo et al., 2011). The exponent used in the expression for the frequency tail has different values (see Siadatmousavi et al., 2012 for a brief review). For shallow water, Kitaigordskii et al. (1975) suggested an f^{-3} tail, and Liu et al. (1989) suggested f^{-4} for growing young wind-sea and f^{-3} for fully developed wave spectra. Badulin et al. (2007) suggested f^{-4} for frequencies with dominant non-linear interactions. The study carried out at Lake George by Young and Babanin (2006) revealed that in the frequency range $5f_p < f < 10f_p$, the average value of the exponent 'n' of f^{-n} is close to 4. Other studies in real sea conditions indicate that the high-frequency shape of f^{-4} applies up to a few times the peak frequency (f_p) and then decays faster with frequency. The spectra for coastlines in Currituck Sound with short fetch conditions showed a decay closer to f^{-5} when f is greater than 2 or 3 times the peak frequency (Long and Resio, 2007). Gagnaire-Renou et al. (2010) found that the energy input from wind and the dissipation due to white capping has a significant influence on the high-frequency tail of the spectrum.

The monsoons of the Indian Ocean are an example of strong ocean-atmosphere interactions. In the northern Indian Ocean during monsoon, the large-scale wind field changes its direction between boreal summer and winter, leading to changes in the wave patterns as well. Several studies have been carried out on wave spectral modelling in the northern Indian Ocean dealing with only the single-peaked spectra (Dattatri et al. 1977; Narasimhan and Deo 1979; Kumar and Kumar 2008). But the percentage of double-peaked wave spectra observed in the Northern Indian Ocean is very high compared to the single-peaked, which makes it important to be represented by a parametric spectrum model. The physical processes that influence the wave spectrum include local events like sea breeze/land breeze systems and extreme events like tropical cyclones. In both cases, the wind speed and wind direction change at a very different time scale, providing a growth and decay phase which in turn has a significant effect on the growth and decay of the wave spectrum.

During the non-monsoon period, winds in the coastal regions of India are dominated by the sea breeze. The diurnal sea and the land breeze are caused due to the contrasting thermal responses of land and water surfaces and have their maximum vertical extend in the tropical coastal regions (Abbs and Physick, 1992). A sea-land breeze cycle has mainly two phases; onshore and offshore. During the onshore phase of the sea-land breeze cycle, starting from late morning to early afternoon, the wind speed increases to reach its maximum. At night the wind speed drops, and the wind direction veers offshore in the early hours of the morning. This offshore phase is known as the land breeze. Many studies have shown that the sea breeze can significantly impact coastal processes like alongshore sediment transport (e.g., Masselink 1998, Masselink and Pattiaratchi 1998; Pattiaratchi et al., 1997). Even though the importance of seasonally reversing monsoon winds on ocean waves in the Indian coastal region has been well studied, much attention is not paid to the evolution of wave spectra during the sea-land breeze cycle. In the earlier studies on the spectral characteristics of waves off the east and west coasts of India (Dattatri et al., 1977; Narasimhan and Deo, 1979; Kumar and Kumar, 2008; Aboobacker et al., 2014; Kumar et al., 2014a, 2014b; Sanil Kumar and Anjali, 2015), the evolution of the wave spectrum in response to the changes in the wind has not been discussed. Some studies have discussed the influence of sea breeze on the waves in the coastal waters of India (Neetu et al., 2006; Remya and Kumar, 2013; Glejin et al., 2013; Aboobacker et al., 2014; Amrutha et al., 2016). Vethamony et al. (2011) have studied the super-imposition of wind-seas on pre-existing swells of the eastern Arabian Sea and found that the wave spectra distinctly bring out salient features of deep-water swell and wind-sea generated by the local sea breeze. But the evolution of wave spectra in response to the changes in wind speed and direction during a diurnal sea-land breeze cycle along the Indian coast has not been studied.

A tropical cyclone (TC) with intense and fast-varying winds produces a severe and complex ocean wave-field that can propagate for thousands of kilometres away from the storm centre, resulting in dramatic variation of the wave-field in time and space. In the northern Indian Ocean, there are 5–6 times more tropical disturbances in the Bay of Bengal than in the Arabian Sea (Dube et al., 1997). Studies were carried out in the past to understand wave characteristics during a hurricane (Young, 2006; Kumar and Stone, 2007; Xu et al., 2007; Chu and Cheng, 2008; Soomere et al., 2008; Fan et al., 2009; Babanin et al., 2011; Kumar et al., 2012; Amrutha et al., 2014). The evolution of the wave energy spectrum during the onset of a TC is set by the input of energy from the wind, the transfer of energy between different frequency bands via non-linear wave-wave interactions, and the energy loss due to wave breaking (Phillips, 1980). Since the wave spectral behaviour during extreme wave conditions is an important factor in the structural design as well, the wave spectra during different stages of extreme events like TC and the changes in wave spectral shape during TC should be known.

Figure 1.2 shows the newspaper reports covering the damages caused due to cyclone swells and other high-energy swells. Barge P305 of ONGC (Oil and Natural Gas Corporation Limited, India) has sunk as it was hit hard by high-energy swells of cyclone Tauktae. The figure also shows the heavy wave activity at the Oman coast due to the swells caused by the co-occurrence of 2 cyclonic systems KYARR and MAHA, in the Arabian Sea. The sea wall damage at the Kerala coast caused by the high energy swells from the Southern Ocean, also known as ‘Kalla kadal’can be seen in the figure. The swells hit the coasts of south India, inundating low-lying coastlines for up to 200 metres in some places. The swell showed the impacts of a storm in the Southern Ocean 9,000 km away. An anchored ship drifted towards the shore at Visakhapatnam beach due to high swell activity owing to the deep depression over the Bay of Bengal, is also reported.

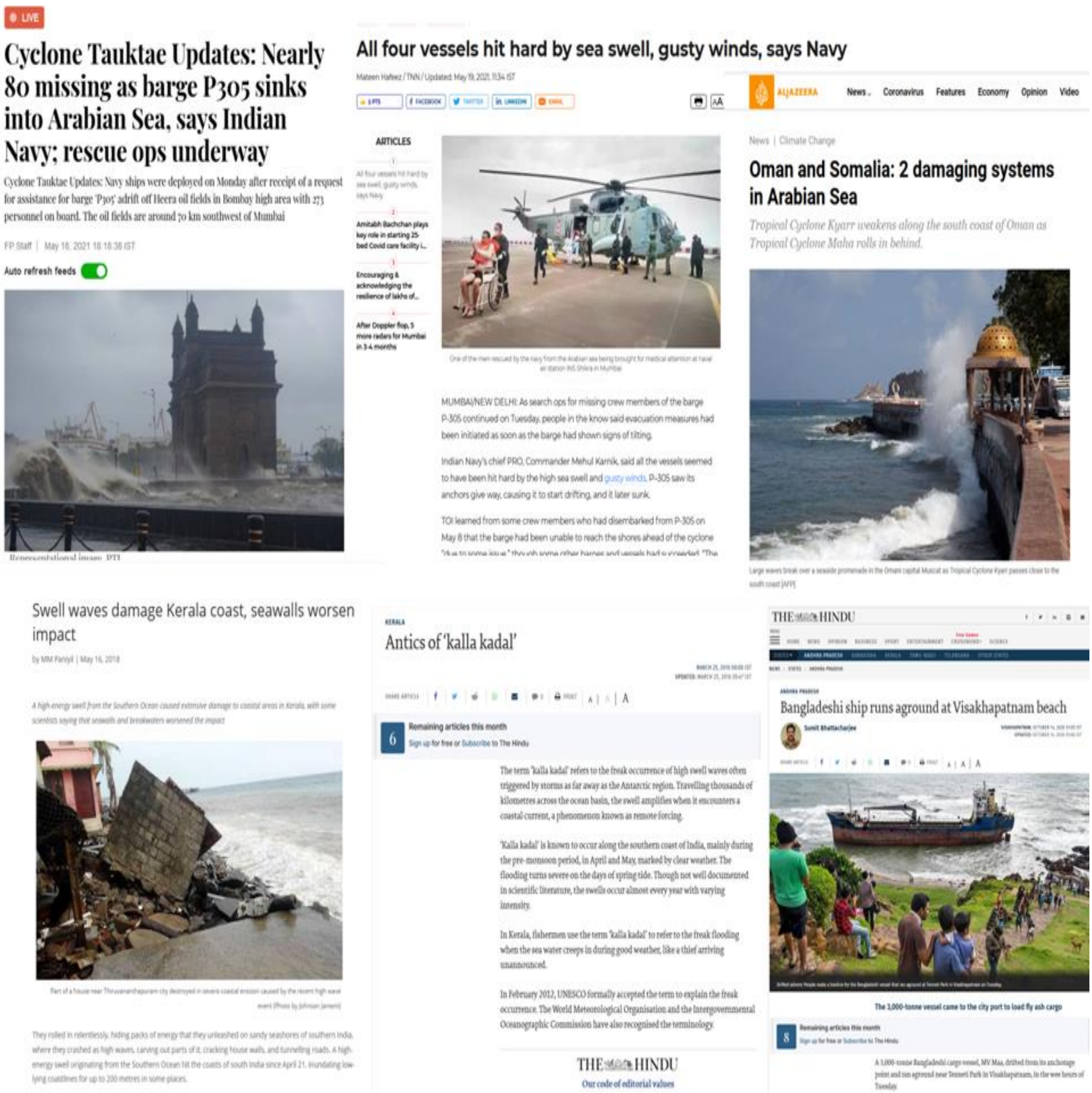
Cyclone Tauktae Updates: Nearly 80 missing as barge P305 sinks into Arabian Sea, says Indian Navy; rescue ops underway

Cyclone Tauktae Updates: Navy ships were deployed on Monday after receipt of a request for assistance for barge 'P305' adrift off Heera oil fields in Bombay high area with 273 personnel on board. The oil fields are around 70 km southwest of Mumbai

All four vessels hit hard by sea swell, gusty winds, says Navy

MUMBAI/NEW DELHI: As search ops for missing crew members of the barge P-305 continued on Tuesday, people in the know said evacuation measures had been initiated as soon as the barge had shown signs of tilting.

Indian Navy's chief PRO, Commander Mehul Karnik, said all the vessels seemed to have been hit hard by the high sea swell and gusty winds. P-305 saw its anchors give way, causing it to start drifting, and it later sunk.

TOI learned from some crew members who had disembarked from P-305 on May 8 that the barge had been unable to reach the shores ahead of the cyclone

Oman and Somalia: 2 damaging systems in Arabian Sea

Tropical Cyclone Kyarr weakens along the south coast of Oman as Tropical Cyclone Maha rolls in behind.

Swell waves damage Kerala coast, seawalls worsen impact

They rolled in relentlessly, hiding packs of energy that they unleashed on sandy seashores of southern India, where they crashed as high waves, carving out parts of it, cracking house walls, and tunnelling roads. A high-energy swell originating from the Southern Ocean hit the coasts of south India since April 21, inundating low-lying coastlines for up to 200 metres in some places.

Antics of 'kalla kadal'

The term 'kalla kadal' refers to the freak occurrence of high swell waves often triggered by storms as far away as the Antarctic region. Travelling thousands of kilometres across the ocean basin, the swell amplifies when it encounters a coastal current, a phenomenon known as remote forcing.

'Kalla kadal' is known to occur along the southern coast of India, mainly during the pre-monsoon period, in April and May, marked by clear weather. The flooding turns severe on the days of spring tide. Though not well documented in scientific literature, the swells occur almost every year with varying intensity.

In Kerala, fishermen use the term 'kalla kadal' to refer to the freak flooding when the sea water creeps in during good weather, like a thief arriving unannounced.

In February 2012, UNESCO formally accepted the term to explain the freak occurrence. The World Meteorological Organisation and the Intergovernmental Oceanographic Commission have also recognised the terminology.

Bangladeshi ship runs aground at Visakhapatnam beach

The 1,000-tonne vessel came to the city port to load fly ash cargo

A 1,000-tonne Bangladeshi cargo vessel, MV Maa, drifted from its anchorage point and ran aground near Tenneti Park in Visakhapatnam, in the wee hours of Tuesday.

Figure 1.5 Newspaper reports covering damages caused to coastal structures and ships due to high energy swells and cyclone waves.

Hence, it is very important to know wave spectral behaviour off the east and west coasts of India by focussing on the spectral shape, wave spectral evolution during sea breeze and tropical cyclones, and the best theoretical wave spectra suitable for the location. Based on these, the objectives of this study are framed as follows.

1.6 Research Objectives

- To study the wave spectral characteristics off the east and west coasts of India (Ratnagiri, Karwar, Honnavar, Gangavaram, and Gopalpur).
- To investigate the change in wave spectral energy in different frequencies during sea breeze and land breeze.
- To study the growth and decay of wave spectra during tropical cyclones.
- To identify the theoretical wave spectra for different wave conditions.

1.7 Study Area

Since the study deals with the wave spectral characteristics, its spatial and temporal variations, variations in different water depths, and evolution in different physical conditions like sea breeze and tropical cyclone, the study area is chosen in such a way that 3 locations are off the west coast of India and two off the west. Figure 1.3 shows the study area with the locations marked. Kumar et al. (2014a) have shown that even though the variations in bulk wave parameters are marginal, there is a significant variation in the wave spectrum within 350 km along the west coast of India. Hence the three locations on the west coast of India are selected as Ratnagiri (in the north), Honnavar (in the south), and Karwar (in between). At the location Honnavar, wave rider buoys are deployed at three different water depths (30 m, 9 m, 5 m) to find out the change in wave spectral characteristics at different water depth and to examine the percentage of deep, shallow and intermediate water waves in different depths. There are considerable differences in the wave climate off the east and west coasts of India. The two locations along the east coast of India selected are Gopalpur and Gangavaram. The coordinates of the wave rider buoy mooring at all the five locations, the water depth, and the period of study are given in Table 1.1.

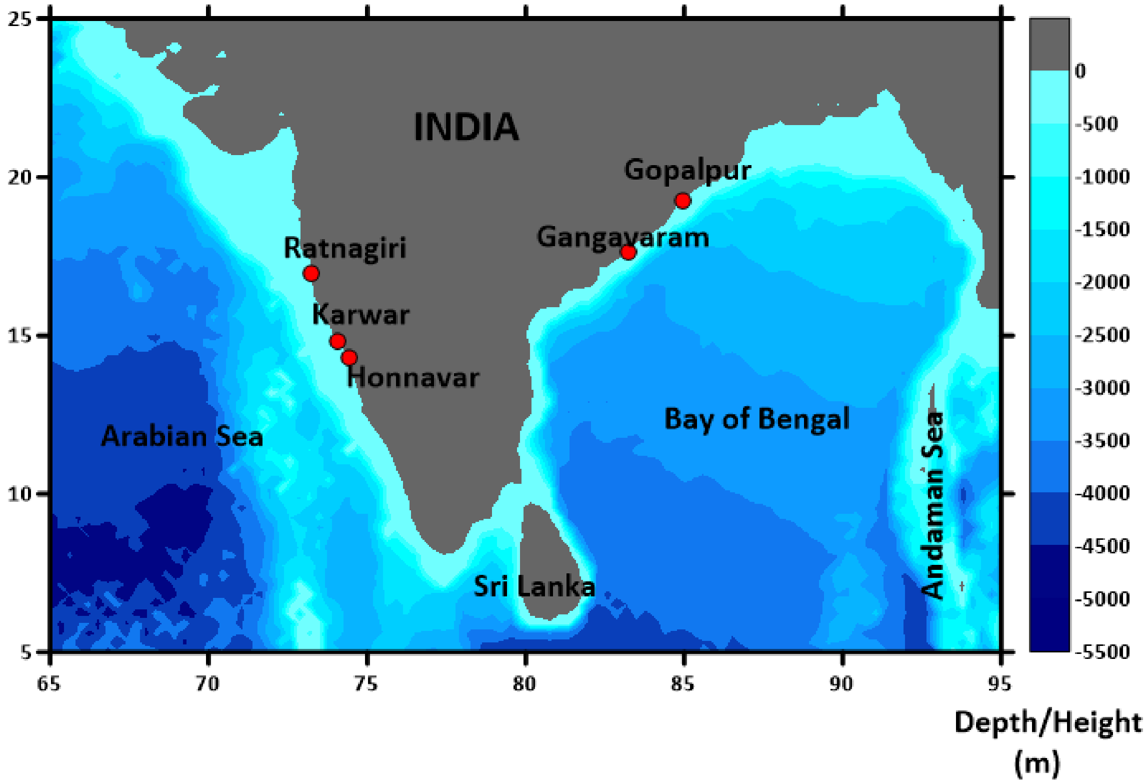

Figure 1.6 Study area showing all the locations

Table 1.1 Specifications of the wave rider buoy data

Location	East/West cast of India	Coordinates	Depth in metres at buoy mooring	Year	Missing data
Gangavaram	East	17.632° N, 83.265° E	15	2011-2015	2013
Gopalpur	East	19.281° N, 84.963° E	15	2013-2015	February (2013) September (2013)
Honnavar	West	14.309° N, 74.254° E	30	2011-2015	
		14.305° N, 74.395° E	9	2011-2015	July (2013) August (2013)
		14.304° N, 74.414° E	5	2011-2015	
Karwar	West	14.822° N, 74.052° E	15	2011-2015	March (2015)
Ratnagiri	West	16.980°N, 73.258°E	13	2011-2015	

Chapter 2: Data and Methodology

2.1 Overview

This chapter deals with the various data sets used in the study. To study the wave spectral characteristics off the east and west coasts of India, measured wave rider buoy data in the near-shore waters are used. To study the wave spectral evolution during sea-land breeze cycle, modelled wave data forced by modelled wind is used. Wind condition during the sea breeze cycle is simulated using the WRF model (Weather Research and Forecast) and waves using the SWAN wave model (Simulating Waves Nearshore). The Bathymetry data used for modelling of waves are derived from NHO (National Hydrographic Office) charts. The growth and decay of wave spectrum during tropical cyclones in the near-shore waters are studied using wave rider buoy data, whereas ECMWF – ERA5 Reanalysis wind and wave data are used in deep-waters. NCEP Reanalysis wind data (National Centre for Environmental Prediction) is also used to study the diurnal variation in wind. The wave spectral characteristics during the cyclones PHAILIN and KYARR are studied here. Joint Typhoon Warning Center (JTWC) is used to get the cyclone track, location and speed. Theoretical spectral fitting and estimation of spectral parameters is done using the measured wave rider buoy data in the near-shore waters.

2.2 Wave measurements

2.2.1 Datawell directional wave rider buoy

The Datawell Directional Waverider buoys DWR-MkIII are used for the wave measurements. The buoys are deployed along the Indian coast as a part of the "Real-time wave data collection program", sponsored by INCOIS (Indian National Centre for Ocean Information Services, Ministry of Earth Sciences, Hyderabad). It is a spherical buoy with a diameter of 90 cm, which measures the height, period, and direction of waves. It consists of three accelerometers (one vertical and two horizontal), pitch and roll sensors, and three axial fluxgate compasses. Wave height is measured using the vertical accelerometer fitted above a gravity stabilized platform. This gravity stabilized platform is a disk suspended in the fluid, filled within a plastic sphere placed in the bottom of the buoy. The wave motion is obtained by double integrating the acceleration signal. Wave direction is measured with the help of two horizontal accelerometers mounted perpendicular to each other in the buoy. These accelerometers measure the horizontal buoy motion in case the buoy is in the upright position. If there is a tilt, the pitch and roll angles are measured by pitch and roll sensors. For this, there are three coils, of which two vertical ones wound around the plastic sphere and one small horizontal coil placed on the platform. The amount of electromagnetic coupling between the fixed coils and the coil on the platform defines the pitch and roll angles. Using the angles of pitch and roll, the horizontal acceleration measured by the accelerometers is converted to real horizontal acceleration. The three axial fluxgate compasses placed inside the buoy measures the Earth's magnetic field in the direction of the x, y, and z axes. Using all these measurements, the acceleration in buoy coordinates is converted to north-west coordinates. The range of heave measured by the buoy lies between -20 and +20 m with a resolution of 1cm and the range of periods lies between 1.6 and 30s. The direction is measured in the range of 0º–360º with a resolution of 1.5º and has an accuracy of 0.5º with reference to the magnetic north. The buoy is moored with the help of a rubber cord and a dead weight. It has a two-meter HF antenna, and it can transmit the data to a shore-based station and/or an Argos satellite. After retrieving the flashcard from the buoy, the data is made to undergo a quality check for removing the error data. Further, the data is processed using w@ves21 software or the FFT technique.

2.3 Wave data analysis

2.3.1 Wave height spectrum

The time-series data of the heave motion of the directional wave rider buoy at every 30 minutes is used to calculate the wave spectrum. The sampling rate of the wave rider buoy is 1.28 Hz (fs), and it collects a total number of N=256 heave samples (hk) every 200 seconds.

$$hk = h(kDt) \qquad \text{k = 0...N-1} \tag{2.1}$$

where Dt=1/fs is the sampling time. The spectrum is calculated by applying a fast Fourier-transform (FFT) in the frequency range 0 to $f_s/2$ = 0.64 Hz, having a resolution of f_s/N = 0.005 Hz.

The Fourier coefficients are calculated as follows:

$$H_l = H(f_l) = \sum_{k=0}^{N-1} w_k h_k \exp\,(2\pi ikl/N) \tag{2.2}$$

$$i = \sqrt{-1} \qquad f_l = l/N\Delta t \qquad l = 0 \ldots N-1$$

Where w_k is the window coefficient, which is a cosine-shaped window applied by Datawell over the first and last 32 samples.

$$w_k = w_{225-k} = \frac{1}{2}\left[1 - cos\left(\frac{k\pi}{32}\right)\right] \qquad \text{k = 0...31} \tag{2.3}$$

$w_k = 1$ otherwise

For normalization, all window coefficients must be divided by

$$w_{norm} = \sqrt{f_s \sum_{k=0}^{N-1} {w_k}^2} \tag{2.4}$$

The power spectral density from Fourier coefficients is calculated as follows

$$PSD(f_0) = |H_0|^2 \tag{2.5}$$

$$PSD(f_l) = |H_l|^2 + |H_{N-l}|^2 \qquad l = 1 \ldots . \mathrm{N}/2 - 1 \tag{2.6}$$

$$PSD\left(f_{N/2}\right) = \left|H_{N/2}\right|^2 \tag{2.7}$$

The frequencies range from 0.0 Hz to 0.64 Hz is in steps of 0.005 Hz. All the coefficients are smoothed according to

$$\overline{PSD_l} = \frac{1}{4}PSD_{l-1} + \frac{1}{2}PSD_l + \frac{1}{2}PSD_{l+1} \tag{2.8}$$

The half-hourly wave spectrum is computed by averaging 8 consecutive spectra covering 1600 s.

The spectral moments are derived using the following equation

$$m_n = \int_0^\infty f^n S(f)df \quad \text{n = 0,2} \tag{2.9}$$

S(f) is the spectral energy density which is a function of frequency

Significant wave height and mean wave period are obtained from spectral moments

Significant wave height, $H_{m0} = 4\sqrt{m_0}$ (2.10)

Mean wave period $T_{m02} = \sqrt{{m_0}/{m_2}}$ (2.11)

The peak wave period is calculated from the peak frequency of the spectrum, which is the frequency at which spectral energy density is maximum. The maximum wave height (max H) is obtained from the zero-crossing analysis of the surface elevation data.

2.3.2 Wave direction spectrum

Wave directional spectrum is obtained by including the time-series of north, west, and vertical (n, w, v) displacements and calculating the Fourier coefficients for them.

The mean wave direction is calculated using the formula

$$\Theta_0 = \arctan\left(\frac{b_1}{a_1}\right) \tag{2.12}$$

Where $a_1 = \frac{Q_{nv}}{\sqrt{(C_{nn}+C_{ww})C_{vv}}}$ (2.13)

$$b_1 = \frac{-Q_{wv}}{\sqrt{(C_{nn}+C_{ww})C_{vv}}} \tag{2.14}$$

Where C represents the co-spectra and Q, the quad spectra formed on the Fourier components of north, west, and vertical displacements.

The directional spread is calculated as follows

$$S = \sqrt{2 - 2m_1} \tag{2.15}$$

Where $m_1 = \sqrt{{a_1}^2 + {b_1}^2}$ (2.16)

2.4 Separation of wind-seas and swells

2.4.1 1D Spectral partitioning

The 1-D separation algorithm suggested by Portilla et al. (2009) is used for wind-sea and swell separation from the measured data. According to this method, the energy at the peak frequency of a swell system should be less than the energy of the PM spectrum (Pierson and Moskowitz, 1963) at the same peak frequency. Here the ratio of the spectral energy density at the peak frequency of the measured spectrum and the PM spectrum is calculated. If this ratio is greater than 1, the wave system is considered as wind-sea and otherwise swell. Thus the wave separation frequency f_c is calculated. Swell and wind-sea parameters are calculated by integrating frequency from 0.025 Hz to f_c, and f_c to 0.58 Hz, respectively.

In the case of cyclone generated waves for differentiating sea of different origins, a parameter equivalent wind-sea frequency (f_u) calculated from the wind speed is used.

$$f_u = \frac{g}{2\pi\beta U} \tag{2.17}$$

U = wind speed, g = 9.81, β = 1.2 (Donelan et al., 1985)

The equivalent wind-sea frequency f_u is the lowest wave frequency, which may receive energy input from the winds with constant wind speed.

2.4.2 2D Spectral partitioning

Spectral partitioning is a technique used to partition the directional wave spectrum into separate subsets of individual wind-sea and swell systems. In this study, a spectral partitioning algorithm introduced by Douglas Cahl and George Voulgaris (2019) based on the work of Hanson and Phillips (2001) and Portilla et al. (2009) is used.

1) The 2D directional wave spectrum is filtered using double convolution.
2) The spectrum is partitioned with the watershed algorithm, and the partition parameters like peak frequency, peak direction, and peak energy for each partition are calculated.
3) The wind partition is defined, and all partitions within the wind region are merged. Here the minimum frequency of wind-sea is taken as 0.12 Hz.
4) Mutual swell peaks are combined

   Here the mutual swell peaks, which are the adjacent swell peaks that belong to the same swell system, are merged. Two neighbouring swell peaks are considered mutual if it satisfies any one of the criteria given below.

   a) Here the spread of each individual peak ($\overline{\delta f^2}$) and the distance between the peaks (Δf^2) are compared. If the spread of either peak satisfies the peak separation criterion $f^2 \leq k\overline{\delta f^2}$, then the two peaks are combined. Here ' k ' is the spread factor, and its value is taken as 0.4.
   b) If the squared distance between the two swell peaks is less than the minimum squared distance ($(6 * df)^2$) and the directional separation between two peaks is less than 90°. Here 'df' is the difference between the frequencies of the two swell peaks.
5) Only the partitions above the noise level and partitions below 0.58 Hz are selected
6) The remaining swell partitions that do not have a valley between them are merged

8) The swell partitions with significant wave height above 0.2 m are only considered
9) The wave parameters for each partition are calculated

2.5 Estimation of high-frequency slope

The wave spectrum, which is defined as the distribution of wave spectral energy over frequency, is in the form

$$S(f) = kf^{-b} \tag{2.18}$$

Here 'S(f)' is the spectral energy density as a function of frequency, ' f ' is the frequency, and k is a constant. The behaviour of the high-frequency part of the spectrum is studied by fitting a curve to the high-frequency part (f > 0.2Hz) of the wave spectrum data. The curve used for fitting is given below.

$$\ln(S) = b \times \ln(f) + k \tag{2.19}$$

The exponent (the value of b) and the coefficient ' k ' are estimated for the best-fit curve based on statistical measures such as the least-squares error and the bias. The slope of the high-frequency part of the wave spectrum is represented by the exponent of the high-frequency tail.

2.6 Computation of inverse wave age

Inverse wave age (ω) is defined as the ratio of wind speed at the sea surface to the phase speed of the waves.

$$\omega = \frac{U_{10}}{C_p} \tag{2.20}$$

Where U_{10} is the wind speed at 10m and C_p is the phase velocity which is given by, $C_p = \frac{gT}{2\pi}$, where T is the time period.

The waves are considered to be wind-sea if $\omega > 1$ and swells if $\omega < 1$.

2.7 Bathymetry data

Bathymetry data is very important in the modelling of near-shore waves. In this study, the digitized bathymetry from National Hydrographic Office (NHO) charts is used for modelling purpose. These charts are produced by the Indian Naval Hydrographic Department (INHD), the nodal agency for Hydrographic surveys and nautical charting in India.

2.8 Wind measurements

2.8.1 WRF modelled wind

The Weather Research and Forecasting (WRF) Model (Skamarock et al., 2008) is a mesoscale numerical weather prediction system developed for operational forecasting applications and for atmospheric research. This model was developed by the collaborative partnership of the National Center for Atmospheric Research (NCAR), the National Oceanic and Atmospheric Administration (represented by the National Centers for Environmental Prediction (NCEP) and the Earth System Research Laboratory), the U.S. Air Force, the Naval Research Laboratory, the University of Oklahoma, and the Federal Aviation Administration (FAA). It can be used for meteorological applications having scales from10 meters to thousands of kilometres. Here the WRF model is used for the simulation of winds in the near-shore region during the sea-land breeze cycle. NCEP FNL wind data is used as the input for the WRF model. From the model output, the 3 hourly wind data (u wind and v wind) with a resolution of 0.027° × 0.027° is extracted for the domain 74.25^{o}E to 74.5^{o}E and 14.2^{o}N to 14.4^{o}N.

2.8.2 ECMWF - ERA5 Reanalysis wind data

ERA5 is the fifth generation of ECMWF atmospheric reanalyses of the global climate, which started in the 1980s (Hersbach and Dee, 2016). It provides the parameters on recent climate by combining models with observation. It is having a spatial resolution of 31 km globally with 137 levels to 0.01 hPa and a temporal resolution of 1 hour. Here ERA5 reanalysis wind data (u wind and v wind) is used to study the wind distribution during the tropical cyclones PHAILIN and KYARR.

2.9 Modelling of Waves – SWAN

SWAN (Simulating Waves Nearshore) is a third-generation wave model used for simulating realistic wave parameters in coastal areas, lakes, and estuaries from given wind, bottom, and current conditions (Booij et al. 1999; Ris et al.1999). It is a discrete spectral model based on the wave action density equation where the wave-current interaction through radiation stresses is taken into consideration. The model equation is given below

$$\frac{\delta N}{\delta t} + \frac{\partial(C_{g,x}N)}{\partial x} + \frac{\partial(C_{g,y}N)}{\partial y} + \frac{\partial(C_{\sigma}N)}{\partial \sigma} + \frac{\partial(C_{\Theta}N)}{\partial \Theta} = \frac{S_{tot}}{\sigma} \tag{2.21}$$

$N(\sigma, \Theta, x, y, t)$ is the Wave action density which is defined as wave energy density divided by intrinsic frequency (E/σ) in frequency, direction, space, and time

$C_{g,x}$ and $C_{g,y}$ are the propagation velocities in x and y space

C_σ and C_θ are the propagation velocities in σ and θ space

Where S is known as the source/sink terms. In shallow water, six processes contribute to the source terms $S_{tot.}$

$$S_{tot} = S_{in} + S_{nl3} + S_{nl4} + S_{ds,w} + S_{ds,b} + S_{ds,br} \quad (2.22)$$

These terms denote wave growth by the energy input from wind, nonlinear transfer of energy through wave-wave interactions, and wave dissipation due to white capping, bottom friction, and depth-induced wave breaking, respectively.

The SWAN wave model was developed for accurate wave simulation in coastal regions by adapting shallow water formulations from deep to shallow waters. Also, the validation of the model for the coastal regions of India was done in several studies (Prasad et al. 2013, Sandhya et al. 2014, Umesh, 2015, Amrutha et al. 2016, Umesh et al.2017, Parvathy et al. 2017). Hence, the SWAN model is used in the study.

2.9.1 SWAN –Model setup

In this study, the SWAN wave model forced by 3 hourly wind from WRF output is used to simulate the wave conditions during the sea breeze event. The domain for SWAN is 74.25°E to 74.5°E and 14.20°N to 14.40°N, in 250×200 grids, with a resolution of 0.001°. The 3-hourly wind data with a resolution of 0.027° × 0.027° from the output of WRF model and the wave parameters like significant wave height (H_{m0}), wave period, and wave direction from the directional wave rider buoy deployed at 30 m water depth off Honnavar, Karnataka were used as the input parameters for the SWAN. Since sea-breeze is a coastal phenomenon, whose strength decreases offshore (Aparna et al. 2005), the offshore boundary for the model should be not too far from the coast. Hence the offshore boundary of the SWAN model was taken at 30 m water depth, which is about 18 km away from the coast. The measured wave rider buoy data at 30 m water depth is given as the offshore boundary condition. The same wave parameters were given for all the three boundaries at north, west, and south, whereas the eastern boundary is a closed boundary (land). The digitized bathymetry from the hydrographic chart is used as the bathymetry for SWAN. The model run was carried out for a period of 4 months, starting from 27 January 2015 to 31 May 2015. Here SWAN is run in third generation mode with a time step of 15 min.

SWAN was run for different white capping schemes and friction coefficients (as mentioned in Table 2.1), and the outputs were compared to find out the best scheme for this location. The model was first run (RUN I) with the default settings for white capping dissipation; the Komen type dissipation using $\delta = 1$ as recommended by Rogers et al. (2003) and JONSWAP bottom friction coefficient, c = 0.067 m^2s^{-3}, which is the value originally recommended by Bouws and Komen (1983). The second model run (RUN II) was done using the same white capping and friction coefficient, but with $\delta = 0$. For the third model run (RUN III), the white capping scheme used is the Komen type dissipation with $\delta = 1$ and a constant JONSWAP bottom friction coefficient, c = 0.038 m^2s^{-3} as recommended by Zijlema et al. (2012). The saturation-based white capping scheme based on the work of Alves and Banner (2003), implemented in SWAN following Van der Westhuysen et al. (2007) with a bottom friction coefficient of c = 0.038 m^2s^{-3}, is used in the fourth model run (RUN IV). Triad interactions are not activated in model simulation. This is because, the triad formulation in SWAN depends on water depth and wave amplitude (Holthuijsen, 2007, Rusu et al. 2008). Hence, it depends on bottom characteristics and it is sensitive to local environments. Since the triad interaction parameterisations were tuned for specific environments and there are no such calibration studies carried out in the Indian Ocean region, usage of the existing parameterisation could be inaccurate. Significant wave height (H_{m02}) and mean wave period (T_{m02}) obtained from all the four model runs were compared with the measured wave parameters using root mean square error (RMSE), correlation coefficient (r), scatter index (SI), and bias.

$$\mathrm{RMSE} = \sqrt{\frac{1}{N}\sum_{i=1}^{N}(A_i - B_i)^2} \quad (2.23)$$

$$r = \frac{N\sum_{i=1}^{N}A_iB_i - \sum_{i=1}^{N}A_i\sum_{i=1}^{N}B_i}{\sqrt{\left[N\sum_{i=1}^{N}A_i^2 - (\sum_{i=1}^{N}A_i)^2\right]\left[N\sum_{i=1}^{N}B_i^2 - (\sum_{i=1}^{N}B_i)^2\right]}} \quad (2.24)$$

$$\mathrm{SI} = \frac{\mathrm{RMSE}}{\overline{B}} \quad (2.25)$$

$$\text{Bias} = \frac{1}{N}\sum_{i=1}^{N}(A_i - B_i) \qquad (2.26)$$

where A_i represents the data obtained from the model runs, B_i represents the data from the buoy measurements, N is the number of data points and the over bar represents the mean value.

Table 2.1 Model specifications

Numerical parameters				
	RUN I	**RUN II**	**RUN III**	**RUN IV**
GRID	Curvilinear	Curvilinear	Curvilinear	Curvilinear
Generation	GEN3	GEN3	GEN3	GEN3
Model domain	74.25°E to 74.5°E 14.2°N to 14.4°N	74.25°E to 74.5°E 14.2°N to 14.4°N	74.25°E to 74.5°E 14.2°N to 14.4°N	74.25°E to 74.5°E 14.2°N to 14.4°N
Spatial resolution (°)	0.001°× 0.001°	0.001°× 0.001°	0.001°× 0.001°	0.001°× 0.001°
Lowest-highest Frequency (Hz)	0.05 - 1	0.05 - 1	0.05 - 1	0.05 - 1
No. of frequencies	25	25	25	25
No. of directions	36	36	36	36
Physical processes activated				
Wind input (Exponential wind growth)	Komen et al. (1984)	Komen et al. (1984)	Komen et al. (1984)	Yan (1987)
White-capping	Komen et al. (1984), delta = 1	Komen et al. (1984), delta = 0	Komen et al. (1984), delta = 1	Alves and Banner (2003)
Friction	JONSWAP c = 0.067	JONSWAP c = 0.067	JONSWAP c = 0.038	JONSWAP c = 0.038
Quadruplets interactions	DIA Hasselmann et al. (1985)	DIA Hasselmann et al. (1985)	DIA Hasselmann et al. (1985)	DIA Hasselmann et al. (1985)
Depth induced	ON	ON	ON	ON

Wave breaking				
Refraction	Not activated	Not activated	Not activated	Not activated

2.10 Fitting the theoretical wave spectrum

The measured wave spectrum is fitted with different theoretical wave spectra mentioned in the literature, such as Pierson-Moskowitz spectrum (Pierson and Moskowitz, 1964), Neumann wave spectrum (Neumann, 1953), Scott spectrum (Scott, 1965), TMA spectrum (Bouws, 1985), JONSWAP spectrum (Hasselmann et al. 1973), and Donelan spectrum (Donelan et al. 1985). It was found out that the JONSWAP spectrum and Donelan spectrum match well with the measured spectrum. JONSWAP spectrum fits well with the measured spectrum at the low-frequency region of the spectrum, whereas the Donelan spectrum fits well at the high-frequency region of the spectrum. Hence those two are used for theoretical spectral fitting, and the spectral parameters for α and Υ for the best fitting curve are estimated.

Chapter 3: Wave spectral characteristics off the east and west coasts of India

3.1 Introduction

The physical processes, including the surface wind-wave field in the northern Indian Ocean, follow a distinct seasonal cycle. To get an insight about the wave conditions at the locations of study, the measured significant wave height (H_{m0}) during the year 2015 at all the five locations are shown in figure 3.1. In the figure, it can be seen that the variations in H_{m0} at the three locations (Figure 3.1 a, b & c) along the west coast are similar with a drastic increase in wave height during monsoon, whereas along the east coast (Figure 3.1 d & e), though H_{m0} increases during the monsoon time, the wave height is comparatively less than the west coast. In the eastern Arabian Sea (AS), the H_{m0} up to 5.5 m is measured during the monsoon period (June to September). But during the rest of the time, H_{m0} measured is usually less than 1.5 m. Whereas in the Bay of Bengal, H_{m0} up to 3.31 m is measured during monsoon. In the Bay of Bengal, the seasonal average value of H_{m0} during the non-monsoon period is 0.8 m, and during monsoon, it increases to 1.3 m. Since the Bay of Bengal is the region of the deadliest tropical cyclones, previous studies show that the H_{m0} during tropical cyclones increased up to ~6 to 8 m. It is known that the wave energy spectra measured in the Indian coastal waters during a year are mostly multi-peaked, containing both swells and wind-seas but are dominated by swells. This chapter deals with the wave spectral characteristics off the east and west coasts of India at five locations by focussing on the spectral parameters, inter-annual variations, directional wave spectrum, diurnal variations in the wave spectrum, and the slope of the high-frequency region of the spectrum.

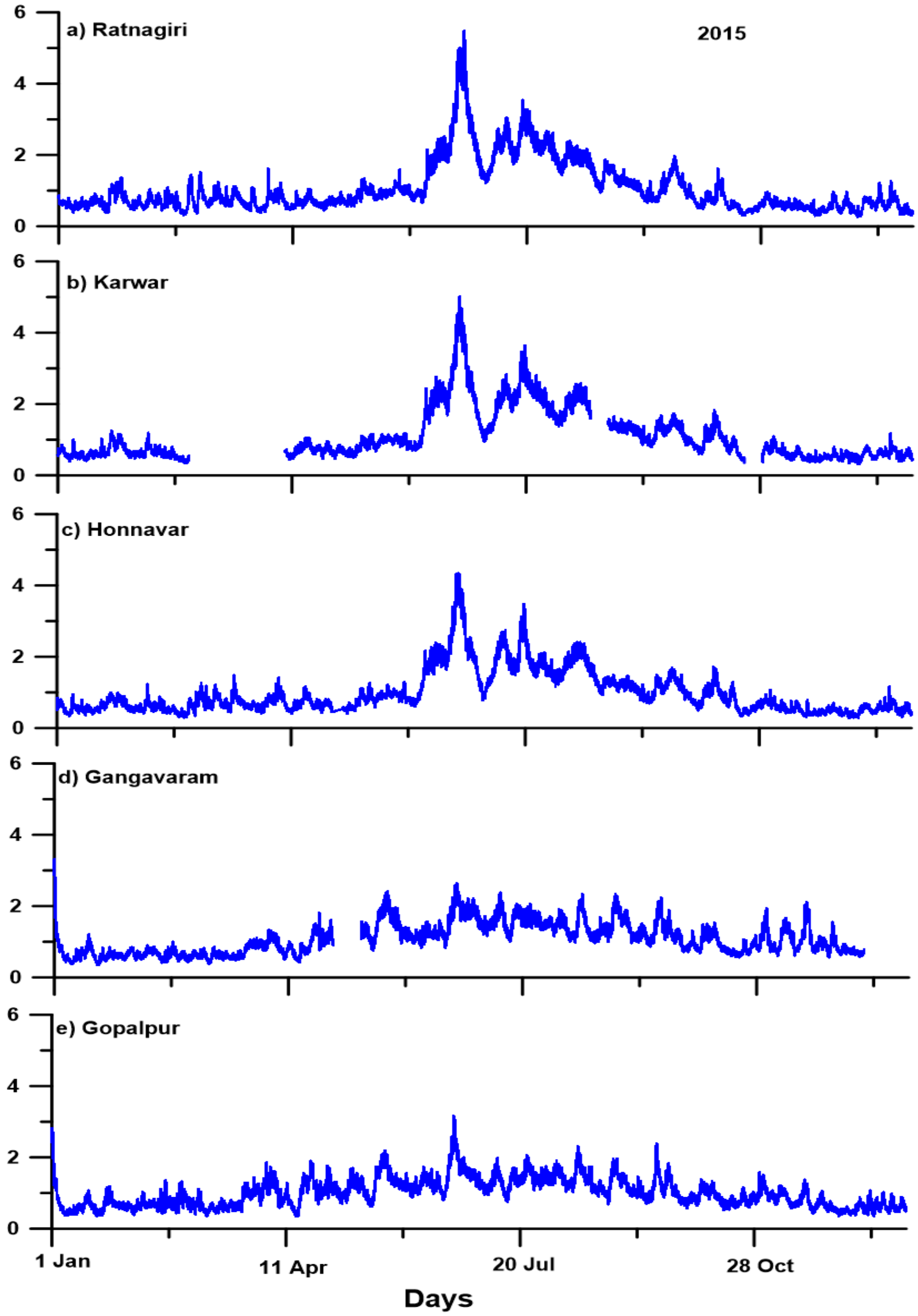

Figure 3.1 Time series of significant wave height for all the five locations during 2015

3.2 Temporal variation in the wave spectrum

3.2.1 Ratnagiri

The time-series of the wave spectral energy estimated from the data measured using wave rider buoy moored at 13 m water depth off Ratnagiri from 23 March 2010 to 6 November 2014 is used in the study.

The contour plots of normalized wave spectral energy density during different months averaged over the years 2010 to 2014 show the monthly variations in wave spectral energy density (Figure 3.2). The normalisation of the wave spectrum is carried out to determine the directional spread of wave energy at different frequencies. Since the range of maximum spectral energy density in a year is large (~ 60 m^2/Hz), each wave spectrum is normalized by dividing the spectral energy density at each frequency with the maximum spectral energy density of the spectrum. In the figure, the energy density can be seen as a narrow band during the monsoon period (June - September) and as a broad band with two peaks during the non-monsoon period. The energy peak during the monsoon period lies around 0.1 Hz, whereas during the non-monsoon period, among the two peaks, one lies at a frequency less than 0.1 Hz and the other at 0.2 Hz. Figure 3.3 shows the monthly averaged directional wave spectra during each month over the years 2010 to 2014. Here, it can be seen that the energy peak observed during the monsoon period is from a direction between SW & W (~ 240^o – 270^o), and the low-frequency peak observed during the non-monsoon is from the SW direction (~ 225^o). The direction of the high-frequency peak during the non-monsoon period is always from the NW direction (270^o - 360^o). The energy peaks at low frequency observed during the monsoon and non-monsoon period are the swells, and the energy peak at high frequency represents the wind-sea generated by the local winds at that location. The swells observed during the monsoon period are generated in the region between 52.5° E to 62.5° E and 5° S to 15° S, whereas the long-period swells observed during the non-monsoon period are generated in the Southern Indian Ocean; the area covered by 40° E to 70° E and 30° S to 50° S (Aboobacker et al. 2011). The predominance of both the swells and the wind-seas are observed from January to May and in November and December (Figure 3.2). In March, long-period swells (T_p ~ 18 to 22 s) arrived in distinct trains, and such episodes occurred four times. These are swells generated in the Southern Ocean (Glejin et al., 2013). From June to August, the spectral energy density is mainly between 0.08 and 0.12 Hz indicating the dominance of swells. Long-period waves (T_p ~ 15 to 22 s) having spectral energy density 1.3 to 2.8 m^2/Hz are observed from 24 August to 26. Except during the monsoon, the two wave systems present in the study area are well separated in frequency and direction (Figure 3.3). The northwest waves dominate the southwest swells from January to March and December. The spectral energy density is low in all other months except during the southwest monsoon season.

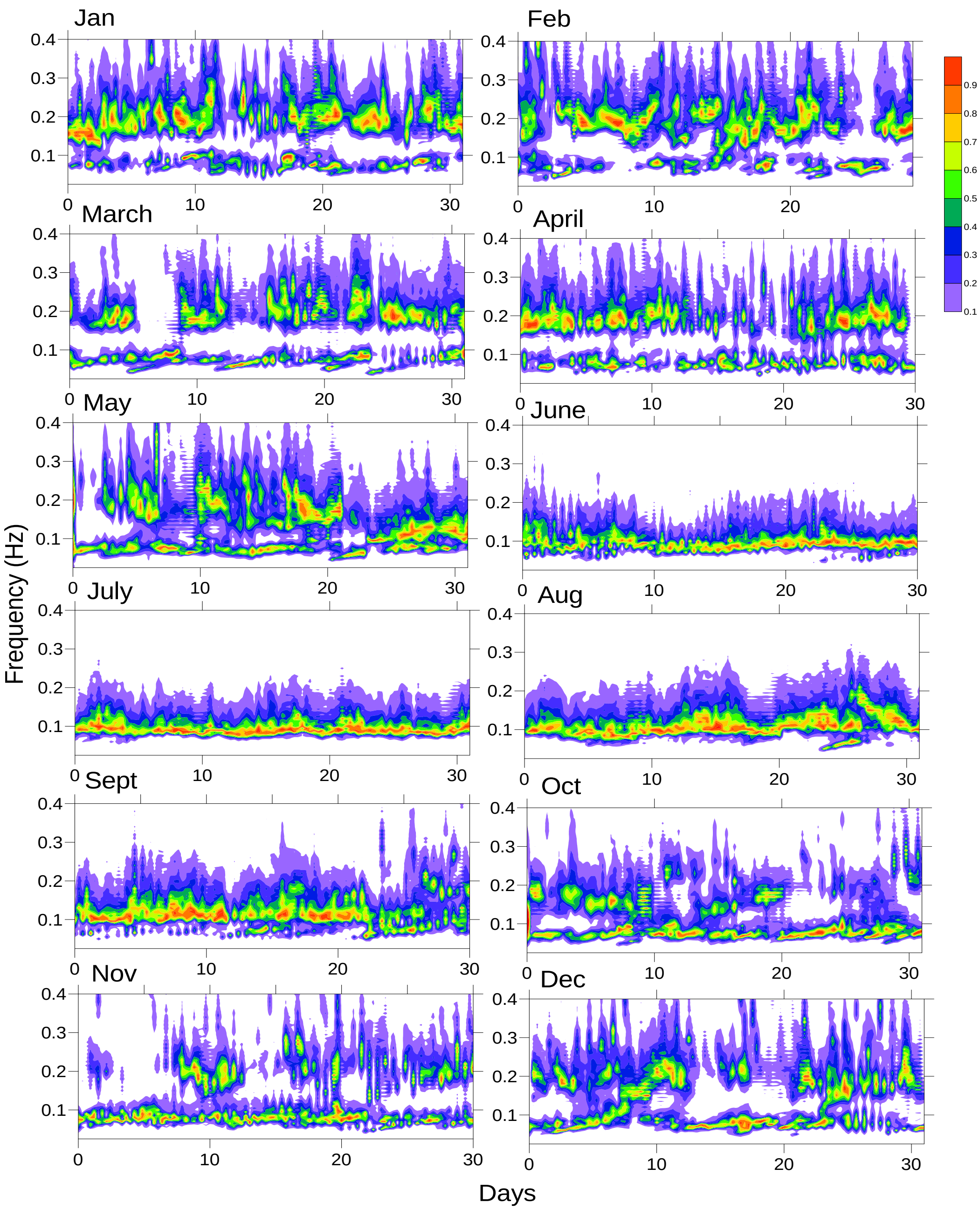

Figure 3.2 Temporal variation of normalized spectral energy density in different months for all the data considered in the study (Ratnagiri).

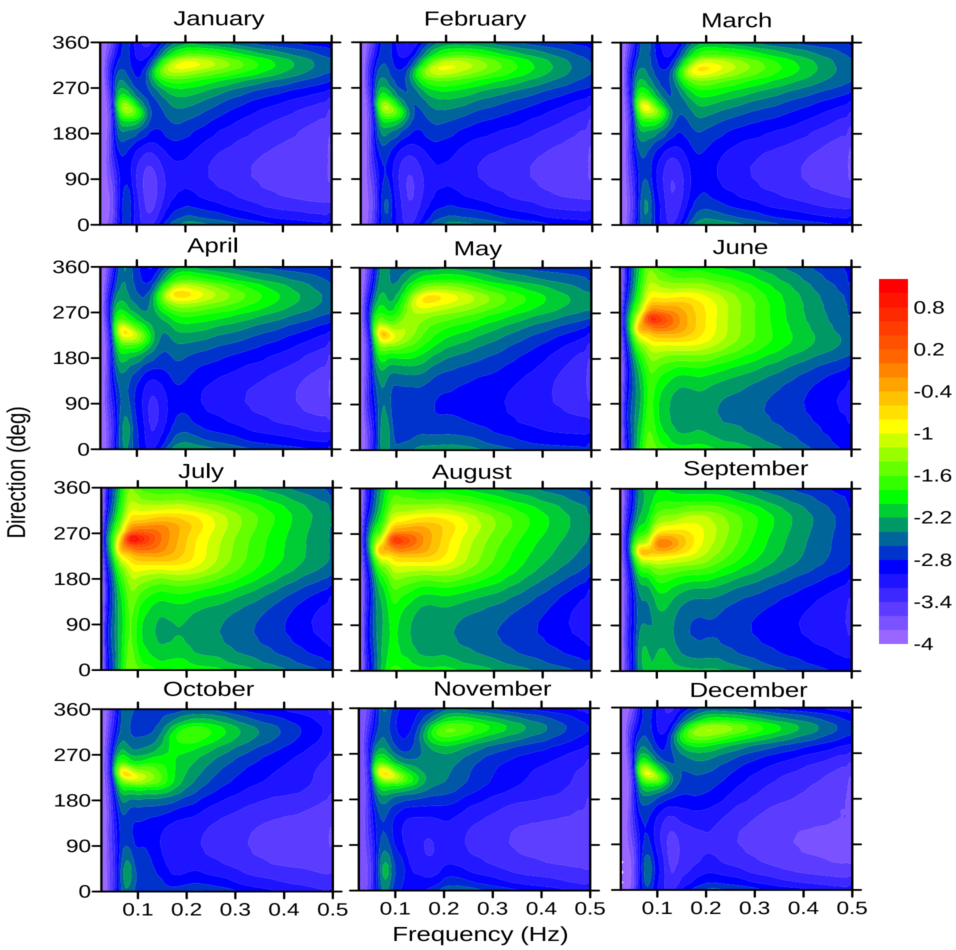

Figure 3.3 Monthly average directional wave spectra considering all the data used in the study (Ratnagiri). The spectral energy density (m^2/Hz/deg) is presented on log scale

3.2.2 Karwar

The coastline at Karwar is 24° inclined to the west from the north, and the 20 m depth contour is inclined 29° to the west. At 10, 30, and 75 km distance from Karwar, the depth contours of 20, 50, and 100 m are present. Hence, large waves in the nearshore will have an incoming direction close to 241° since waves get aligned with the depth contour due to refraction. The waves off Karwar measured using wave rider buoy for a period from 1 January 2011 to 31 December 2015 is used in this study.

The normalized wave spectral energy density contours are presented for different years to know the wind-sea/swell predominance (Figure. 3.4). Here also, like Ratnagiri, the predominance of both wind-sea and swells is observed in the non-monsoon period, whereas in the monsoon, only swells are predominant. The dominance of swells during monsoon is due to the fact that even though the wind at the study region is strong during monsoon, the wind over the entire AS also will be strong, and when these swells are added to the wave system at the buoy location, the energy of the swell increases (Donelan, 1987) and will result in the dominance of swells. The spread of spectral energy to higher frequencies (0.15 to 0.25 Hz) is predominant during January-May (Figure 3.4) due to the effect of sea breeze in the pre-monsoon period. An interesting phenomenon is that the long-period (> 18 s) swells are present for 2.5% of the time during the study period. Due to its exposure to the Southern Oceans and the large fetch available, swells are present all year round in the study area, and the swells are dominant in the non-monsoon (Glejin et al., 2013).

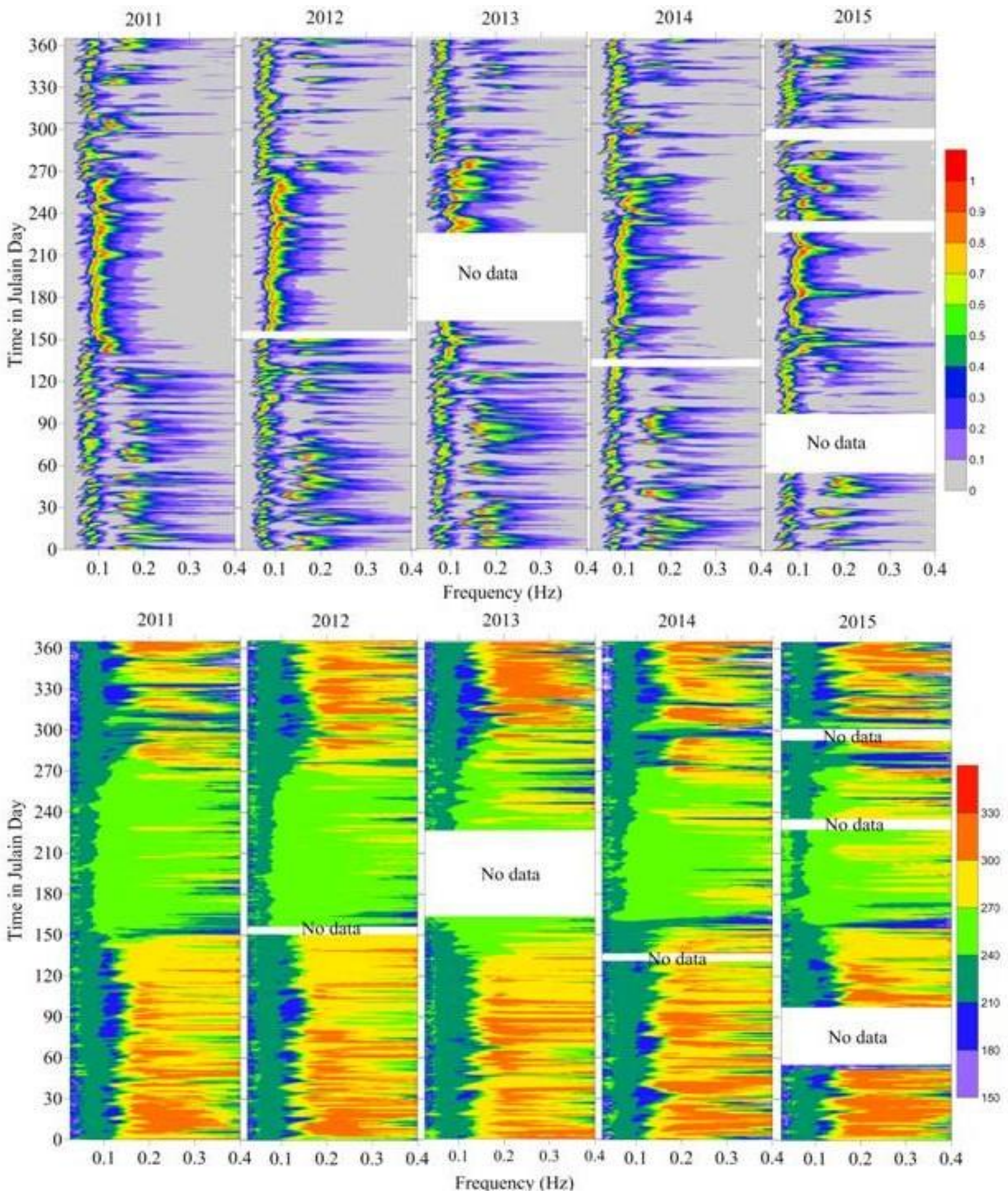

Figure 3.4 Temporal variation of normalized spectral energy density (top panel) and mean wave direction (bottom panel) with frequency in different years (Karwar).

3.2.3 Honnavar

The wave rider buoy data at 9-m water depth off Honnavar (14.3042˚N; 74.3907˚E) for the period from 2009 to 2012 is used for the study. This buoy is located at a distance of 2.5 km away from the central west coast of India. The temporal variations in the normalized spectral energy density for the years 2009 to 2012 are shown in Figure 3.5. In all the years, the wave spectrum is narrow banded during monsoon, with its maximum energy concentration between 0.07 and 0.12 Hz (14 and 8 s) from June to August and between 0.09 and 0.14 Hz (11 and 7 s) during September. During all other times, broad-banded spectra are observed with the presence of both wind-sea and swells. Due to the presence of long-period swells, the energy peak of the spectra lies in the low-frequency side from January to April. During this time, the wind-sea can also be observed. For all the four years studied, the temporal variation in wave spectra shows a similar pattern. The low frequency (< 0.12 Hz) waves observed are from the SW direction (210^o to 240°) from January to May and October to December. The high-frequency waves are from the NW direction during the non-monsoon period. During monsoon, the predominant wave direction is from 240^o to 270°, but the direction of waves with frequency less than 0.08 Hz are from 210^o to 240°. During monsoon, the waves along the 270 km stretch of the eastern Arabian Sea show similar characteristics since the waves at this region are predominantly swells (Anoop et al., 2014). Locally generated waves having low energy and high frequency from the southeast direction can also be seen in the figure.

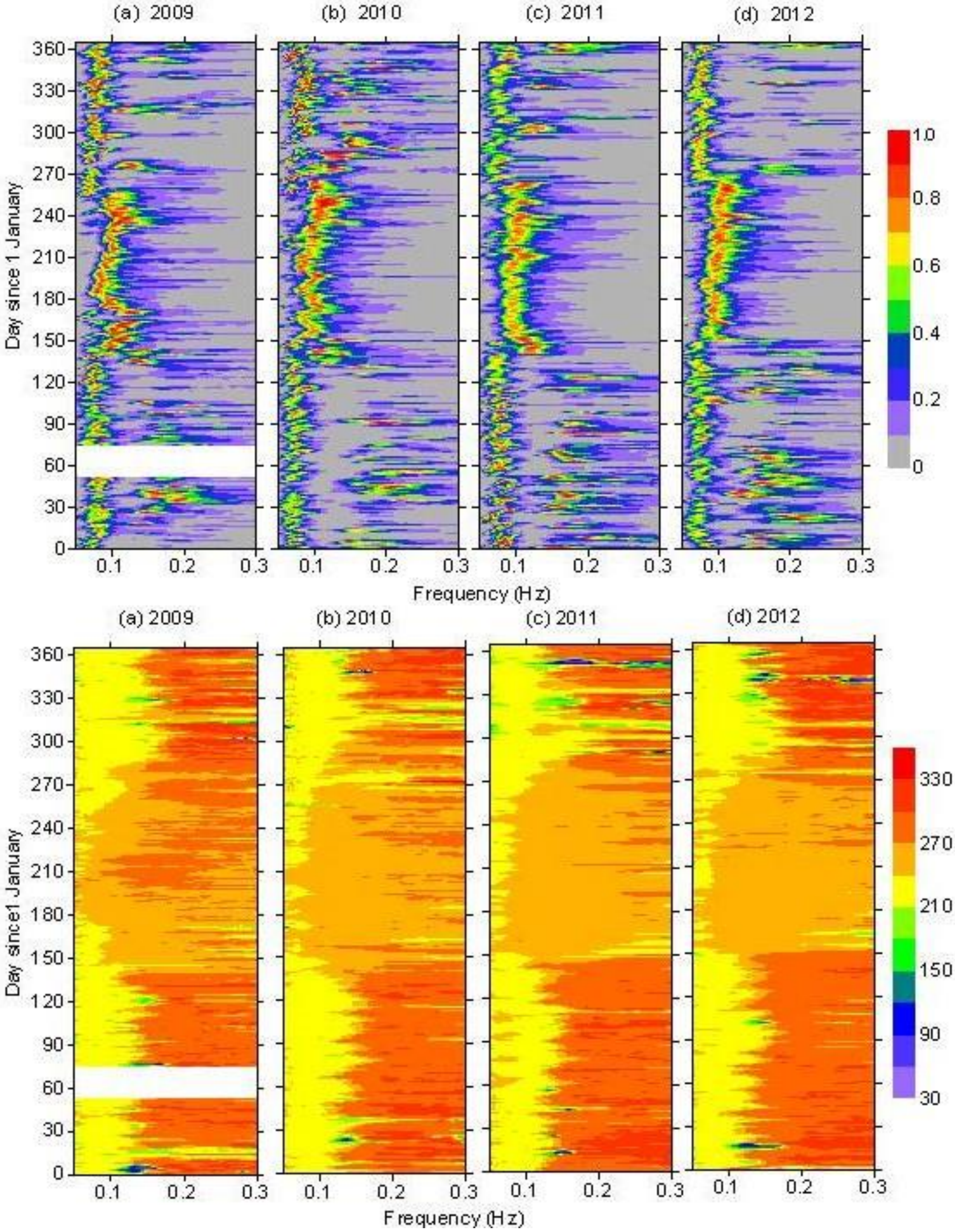

Figure 3.5 Temporal variation in the normalized wave spectral energy density (top) and mean wave direction (bottom) during 2009-2012 (Honnavar). The white patch indicates the gap in the data.

3.2.4 Gangavaram

The waves off Gangaravarm at 15m depth along the east coast, measured using wave rider buoy during the year 2015, are used in this study. The temporal variation in normalized spectral energy density is shown in Figure 3.6. As in the west coast, here also, the spectrum is broad-banded during the non-monsoon period and narrow banded during the monsoon, but with two peaks during most of the time, including monsoon. The low-frequency peaks (0.05 to 0.1 Hz) from SE which is present throughout the year, are the swells from the Southern Indian Ocean. In the monsoon period, one more swell system is observed with a slightly higher frequency (0.1 to 0.15 Hz) from the SE direction, which are the swells generated due to the monsoon winds. The second peak during the months of November and December is in the frequency range of 0.15 to 0.2 Hz, and during the pre-monsoon season, it is in the range of 0.2 to 0.3 Hz, from directions E and SE. The waves with frequencies above 0.2 Hz from the east are the wind-seas and are significant during the pre-monsoon period.

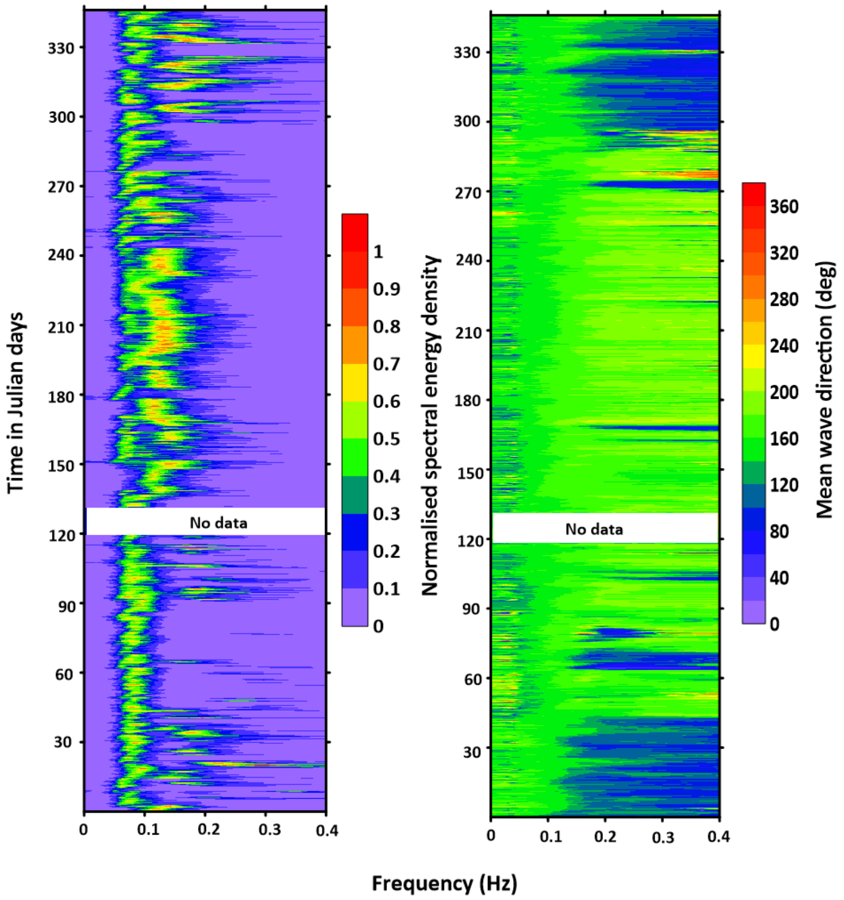

Figure 3.6 Temporal variation in the normalized wave spectral energy density (left) and mean wave direction (right) during 2015 (Gangavaram). The white patch indicates the gap in the data.

3.2.5 Gopalpur

Wave rider buoy data for the location Gopalpur (19.2817˚ N; 84.9640˚ E) located ~1.3 km away from the east coast of India for the period from February 2013 to December 2015 is used in this study. The normalized wave spectral energy density in the frequency-time frame is used to study the energy distribution of waves (Figure. 3.7). The left two panels of figure 3.7 show the time series plot of the normalized spectral energy density with frequency in 2014 and 2015. The contour plots of normalized spectral energy density show a very narrow spectrum within a short frequency range (0.05-0.15 Hz) in the monsoon, whereas during the non-monsoon period, a much broader spectrum with two distinct peaks is observed. On some days, a predominance of wind-sea having high-frequency (0.2-0.3 Hz) is observed from December to May. Over an annual cycle, the majority of the data recorded are multi-peaked spectra (63%), and 80% of the multi-peaked spectra are swell-dominated.

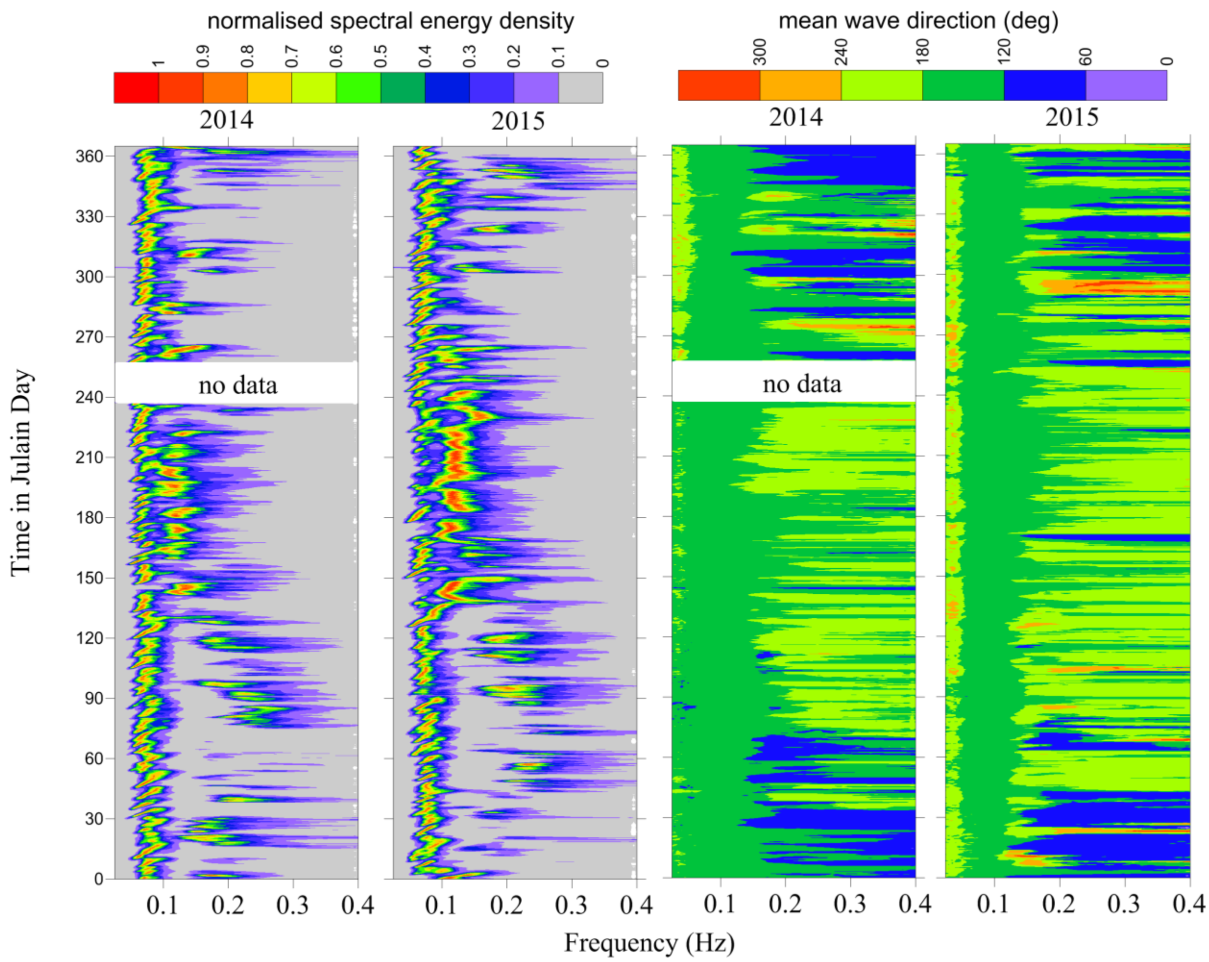

Figure 3.7 Left two panels show the time series plot of the normalized spectral energy density with frequency in 2014 and 2015. Two panels in the right indicate the time series plot of wave direction with frequency.

3.3 Directional wave spectrum

The directional wave spectra at all the five locations off the east and west coasts of India during various seasons are shown in Figure 3.8. For the locations off the west coast, the high energy swells from SW and low energy wind-sea from NW during the pre-monsoon and post-monsoon season can be clearly seen in the figure. Also, the high-energy monsoon swells can be observed from a direction between SW and W. The annual average spectra at the three locations off the west coast show both wind-sea and swells. The pattern obtained is similar for all three locations off the west coast. Off the east coast, long-period swells, with frequency less than 0.1 Hz from SE direction, are observed during all the seasons, and an additional swell peak from S – SE direction with a frequency between 0.1 and 0.15 Hz is observed during monsoon. Wind-sea with comparatively low energy can be observed from the south during the pre-monsoon. The annual average spectrum shows the dominance of swells.

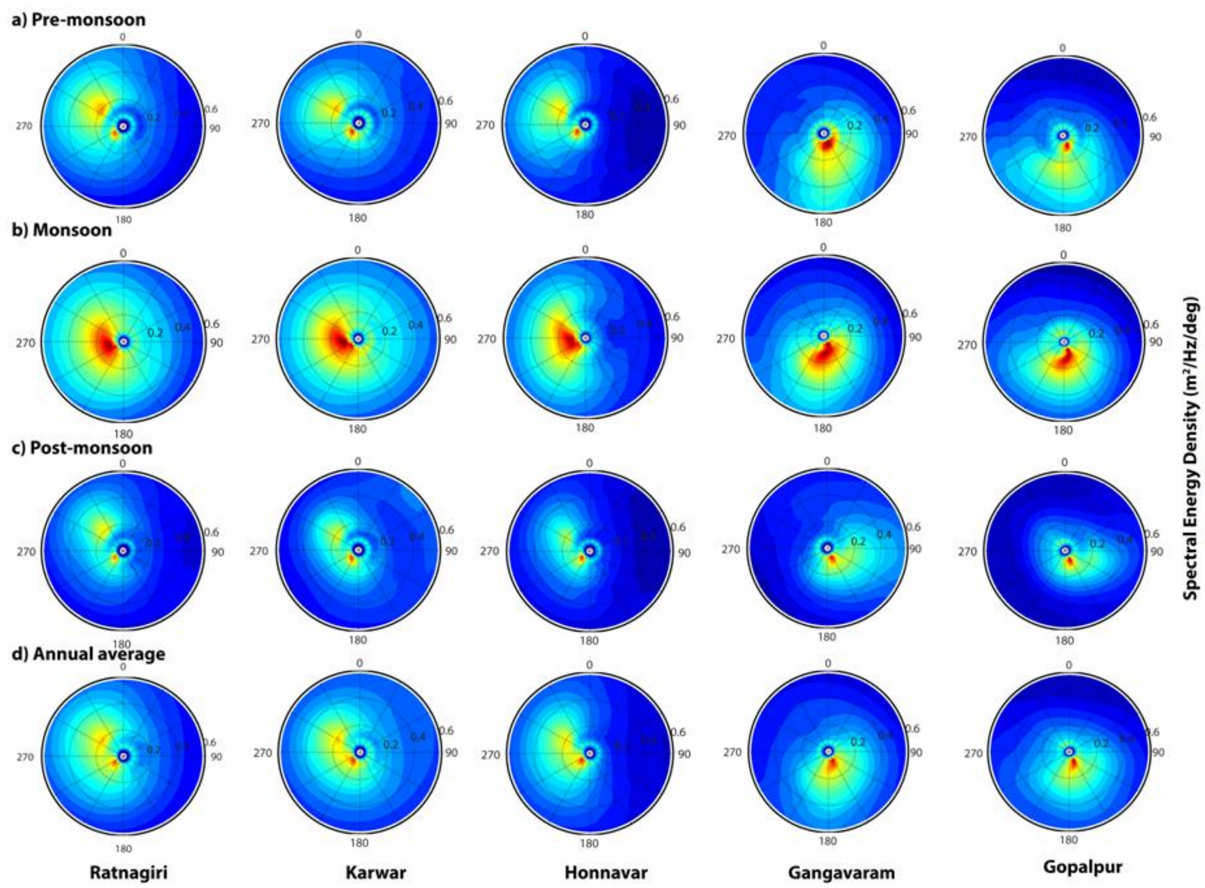

Figure 3.8 Directional wave spectra for all the five locations during 2015

The spectrum averaged during the pre-monsoon, monsoon, post-monsoon seasons and its annual average for all the locations in eastern AS show high-energy swells from SW and low-energy wind-sea from NW during pre-monsoon and post-monsoon seasons. Whereas during monsoon only swells are observed with very high-energy distributed between SW and W. Annual average spectrum shows both wind-sea and swells. The pattern obtained is similar for all three locations on the west coast. Whereas off the east coast, long-period swells, with frequency less than 0.1 Hz from SE direction, are observed during all the seasons and an additional swell peak from S – SE direction with a frequency between 0.1 and 0.15 Hz is observed during monsoon. Wind-sea with comparatively low energy can be observed from the south during pre-monsoon and from east during post-monsoon seasons.

3.4 Percentage of wind-seas and swells

In the statistical analysis of spectra, the spectra are grouped according to the T_p, and the percentage of single or multi-peaked spectra in each wave group is calculated. The percentage of single-peaked and multi-peaked spectra calculated for two locations, Ratnagiri (west coast) and Gopalpur (east coast), are given in Table 3.1 and Table 3.2. For Ratnagiri, the percentage is calculated using the wave spectral data during the period 2010 to 2014, and for Gopalpur, the wave data during the year 2015 is used.

3.4.1 Ratnagiri

The study shows that during June and July, 72 % of the wave spectra are single-peaked swell spectra (Table 3.1). Over an annual cycle, 29 % of the wave spectra are single-peaked spectra, and 72 % are multi-peaked spectra. The high number of multi-peaked spectra observed is due to the co-existence of wind-sea generated by the strong local winds during the non-monsoon period and the swells arriving from the Indian Ocean. For the study area, over an annual cycle, 27 % of the wave spectra are single-peaked swell spectra, and 42 % are multi-peaked swell spectra. During the monsoon, since the wind speed and direction show a significant variability and a new wave system is created whenever the wind direction or intensity changes, swell-dominated spectra are found more often than wind-sea dominated spectra. The monthly averaged spectrum is wind-sea dominated from January to March and swell-dominated during the rest of the period.

Table 3.1 Percentage of single-peaked and multi-peaked wave spectra in different months

Month	Single-peak (%)				Multi-peak (%)			
	Total	Wind-sea (T_p≤6s)	Swell (T_p≥8s)	Mixed (6 <T_p< 8s)	Total	Wind-sea dominated (T_p≤6s)	Swell dominated (T_p≥8s)	Mixed (6 <T_p<8s)
Jan	6	3	2	2	94	51	29	14
Feb	12	3	7	2	88	42	33	14
Mar	13	1	11	1	87	48	34	6
Apr	10	1	9	0	90	39	44	7
May	12	0	11	1	88	13	55	21
Jun	73	0	73	0	27	0	26	1
Jul	70	0	70	0	30	0	30	0
Aug	49	0	49	0	51	0	44	7
Sep	30	0	29	1	70	3	57	10
Oct	24	0	22	2	76	10	53	13
Nov	29	0	28	1	71	16	49	5
Dec	15	1	13	1	85	27	50	8
Annual average	28	1	27	1	72	21	42	9

3.4.2 Gopalpur

The percentage of single-peaked and multi-peaked spectra along with the wind-sea and swell percentage at the location Gopalpur is given in Figure 3.2. Here, during the one-year period, single-peaked spectra are observed for 37.6% of the time, and the remaining are predominantly swell dominated (49.9%) multi-peaked spectra and the wind-sea dominated multi-peaked spectra 6.6% (Table 3.2). Unlike the west coast, during June to August, the multi-peaked spectra are more (79.6 to 91.8%) compared to other months. The occurrence of single-peaked spectra is high (65.7%) during January compared to other months. The percentage of wind-sea dominated spectra is highest in the month of April.

Table 3.2 Percentage of single-peaked and multi-peaked wave spectra in the year 2015

Month	Single-peak (%)				Multi-peak (%)			
	Total	Wind-sea ($T_p \leq 6$)	Swell ($T_p \geq 8$)	Mixed ($6 < T_p < 8$)	Total	Wind-sea dominated ($T_p \leq 6$)	Swell dominated ($T_p \geq 8$)	Mixed ($6 < T_p < 8$)
January	65.7	0.0	65.1	0.6	34.3	0.3	30.7	3.3
February	43.3	0.1	43.2	0.0	56.7	13.6	43.1	0.0
March	49.5	0.1	49.4	0.0	50.5	4.5	45.9	0.1
April	26.5	0.4	26.0	0.1	73.5	29.3	42.6	1.6
May	36.8	0.3	36.1	0.4	63.2	6.6	51.4	5.2
June	20.4	0.1	20.2	0.1	79.6	2.9	71.5	5.3
July	20.2	0.0	19.8	0.4	79.8	0.1	61.8	17.9
August	8.2	0.0	7.2	1.0	91.8	2.0	63.2	26.6
September	35.8	0.1	35.6	0.2	64.2	1.7	56.7	5.7
October	58.7	0.1	58.3	0.2	41.3	0.3	38.2	2.8
November	47.4	0.0	47.4	0.0	52.6	4.7	45.9	2.0
December	38.2	0.7	37.5	0.1	61.8	13.0	47.4	1.3

3.5 Diurnal variation in the wave spectrum

The earlier studies conducted along the Indian coast have indicated that there is diurnal variation in wave parameters due to the influence of sea breeze (Neetu et al., 2006; Vethamony et al., 2011; Glejin et al., 2013; Kumar et al., 2014a). Here the diurnal variation in wave spectra is studied by calculating the monthly average wave spectra for every 3-hour interval in a day for all the months. The diurnal variation in wave spectra is examined for all five locations; Ratnagiri, Karwar, Honnavar, Gangavaram, and Gopalpur. For all the locations, the data used is for the year 2015, except for Karwar, where due to some data unavailability, 2014 data is used.

3.5.1 Ratnagiri

Figure 3.9 shows the diurnal variations in wave spectra during different months. Here, throughout the day, the spectrum observed is double-peaked with swell and wind-sea peaks during the non-monsoon period (November to May) and single-peaked with only swells during the monsoon period. Diurnal variations in wave spectra are mainly observed in the wind-sea region of the spectra, especially during the non-monsoon time. Here the diurnal variation in the wind-sea peak of the spectra is highest during the months of February, March, and April. During February, the wind-sea peak at 0 hrs lies at 0.19 Hz with energy 0.185 m^2/Hz, which slowly increases to reach the maximum energy (0.245 m^2/Hz) at 15 hrs with a peak frequency of 0.20 Hz. After 15 hours, the energy and the peak frequency of the wind-sea peak decreases. Similar pattern can be observed during March and April. During March, at 0 hrs, the wind-sea peak lies at 0.19 Hz with energy 0.15 m^2/Hz, and at 15 hrs, the energy increases to 0.244 m^2/Hz, with a frequency of 0.18 Hz. During April, at 0 hrs, the wind-sea peak energy is 0.112 m^2/Hz at 0.20 Hz, which shifts to 0.24 Hz with an energy of 0.126 m^2/Hz at 12 hrs. The energy further increases to 0.154 m^2/Hz at 15 hrs, and peak frequency decreases to 0.22 Hz. It can be seen that during these three months, the maximum energy observed is at 15 hrs, and it decreases afterward. Also, the peak frequency slightly increases from 9 to 12 hrs and decreases afterward.

There is no much diurnal variation in the mean wave direction (Figure 3.10), where the swell peak is always from the SW direction (200^o – 250^o), and the wind-sea peak is always from the NW direction (280^o -320^o). This diurnal variation in wave spectrum is due to the effect of sea breeze, which is stronger than the synoptic winds in the coastal regions of India during the pre-monsoon period. To know more about the changes in wind pattern, the 6-hourly NCEP wind data is plotted for all the months (Figure 3.11). In the figure, significant diurnal variations can be observed in the wind speed and wind direction during all the months. The hourly variation of wind speed shows that the sea breeze peak values are between 12-14 UTC during January to March and during October-December and is between 10-11 UTC during April-May (Figure. 3.11). The wind direction also shows diurnal variation during the non-monsoon period with the wind direction from NW (270^o-360^o) during sea breeze peak hours. Though the wind speed peak is between 10-14 UTC, the maximum energy density in waves occurs at 15 UTC.

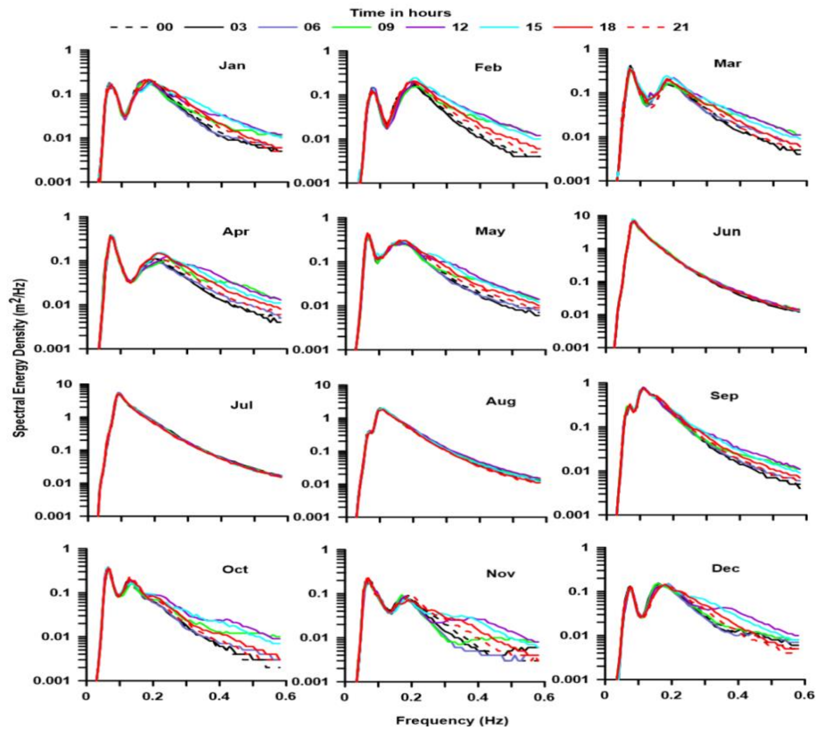

Figure 3.9 Monthly averaged wave spectra at every 3 hours in a day during 2015 at Ratnagiri.

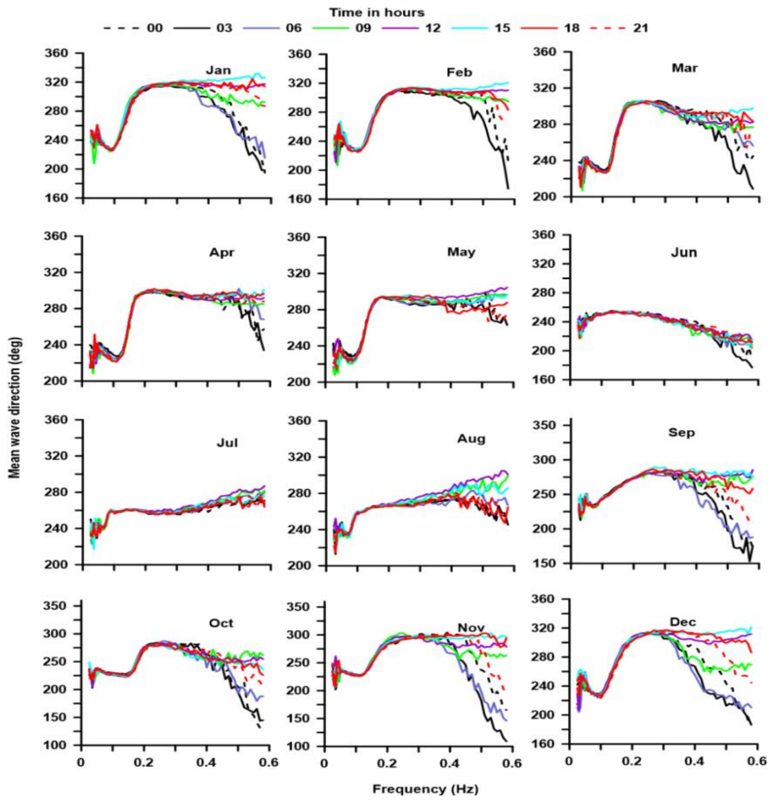

Figure 3.10 Monthly averaged wave directional spectra at every 3 hours in a day during 2015 at Ratnagiri

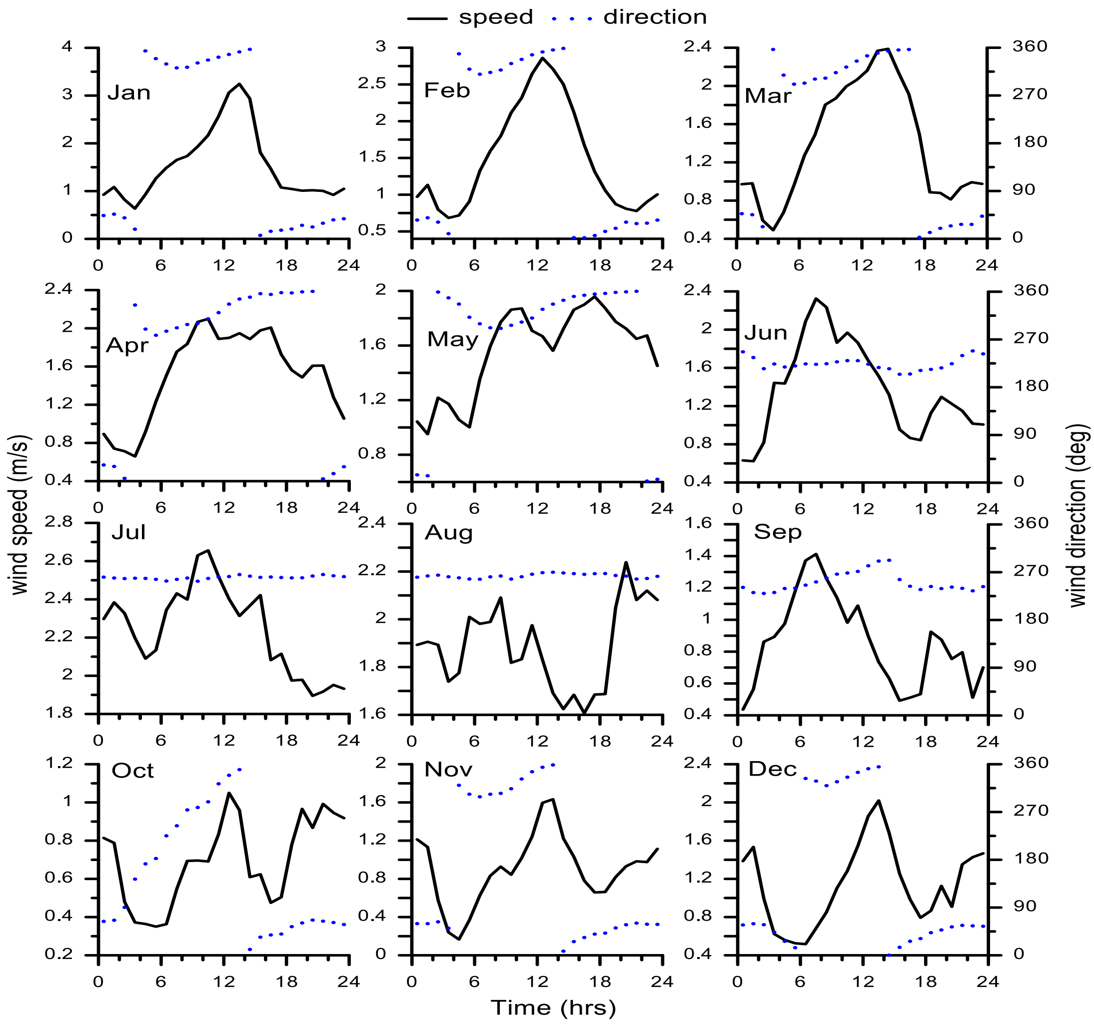

Figure 3.11 Hourly variation of wind speed and direction in different months (Ratnagiri)

Figure 3.12 shows the diurnal variation in wave spectra during April for the years 2010 to 2017 and also the corresponding variation in significant wave height and mean wave period during the same time. From the figure, it can be seen that the significant wave height starts to increase after 6 hrs to reach its maximum value during 15 hrs and then decreases, whereas the mean wave period decreases after 6 hrs and reaches its minimum at 12 hrs and increases afterward. This pattern is similar during all the years. The increase in wave height, along with a decrease in the mean wave period during the sea breeze hours, is due to the super-imposition of wind-sea generated by sea breeze on the pre-existing swells. Since sea breeze is stronger than the synoptic wind existing in that area, the significant wave height increases, and when the short period wind-sea super-impose with the long period swells, the resultant wave period decreases. There is an observed shift in the wind-sea peak towards the high-frequency region at 12 hrs (Figure. 3.9). The diurnal variations in wave spectra for all the years are similar with the maximum energy during 15 -18 hrs, which shows that there is no much inter-annual variation in the diurnal wave spectrum.

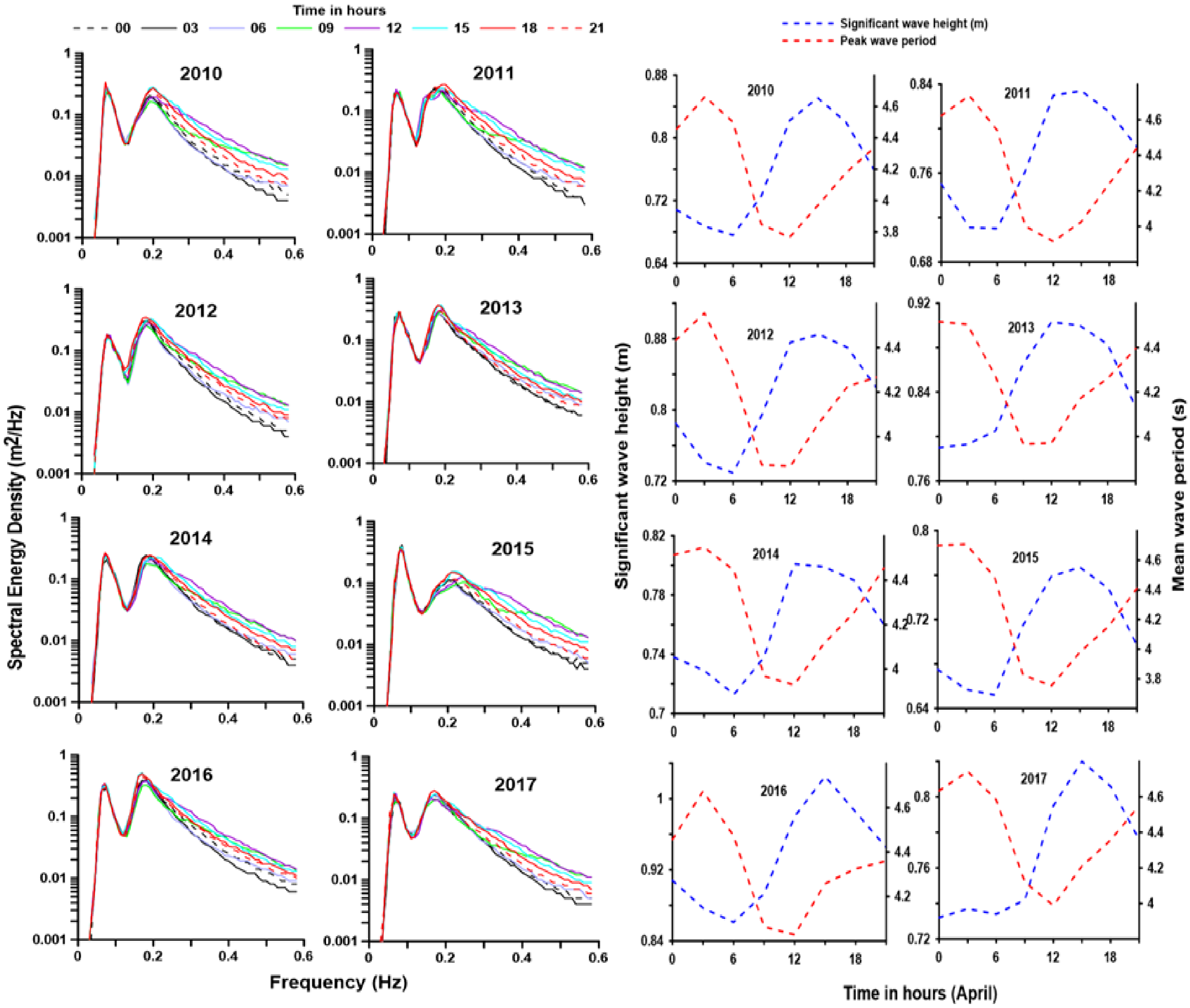

Figure 3.12 (Left Panel) Monthly averaged wave directional spectra at every 3 hours in a day for April (2010-2017). (Right Panel) Hourly variation of significant wave height and mean wave period for April during 2010-2017 (Ratnagiri).

3.5.2 Karwar

The diurnal variation at the location Karwar is shown in Figure 3.13. Here also, diurnal variations are observed in the wind-sea region of the spectra with maximum variation during the pre-monsoon period. During February, the wind-sea peak at 0 hrs lies at 0.19 Hz with an energy of 0.158 m^2/Hz, which initially decreases till 9 hrs (0.116 m^2/Hz) and then increases to reach its peak at 18 hrs (0.185 m^2/Hz) with frequency 0.15 Hz. The case is the same during April, where the energy decreases from 0 hrs (0.154 m^2/Hz) to 9 hrs (0.138 m^2/Hz) and then increases to reach its peak value at 18 hrs (0.172 m^2/Hz). Whereas in March, the wind-sea peak energy increases from 0 hrs (0.192 m^2/Hz) till 15 hrs (0.219 m^2/Hz) without any drop and then decreases after 15 hrs. The maximum energy of wind-sea peak occurs at 18 hrs during February and April, and during March, it is at 15 hrs.

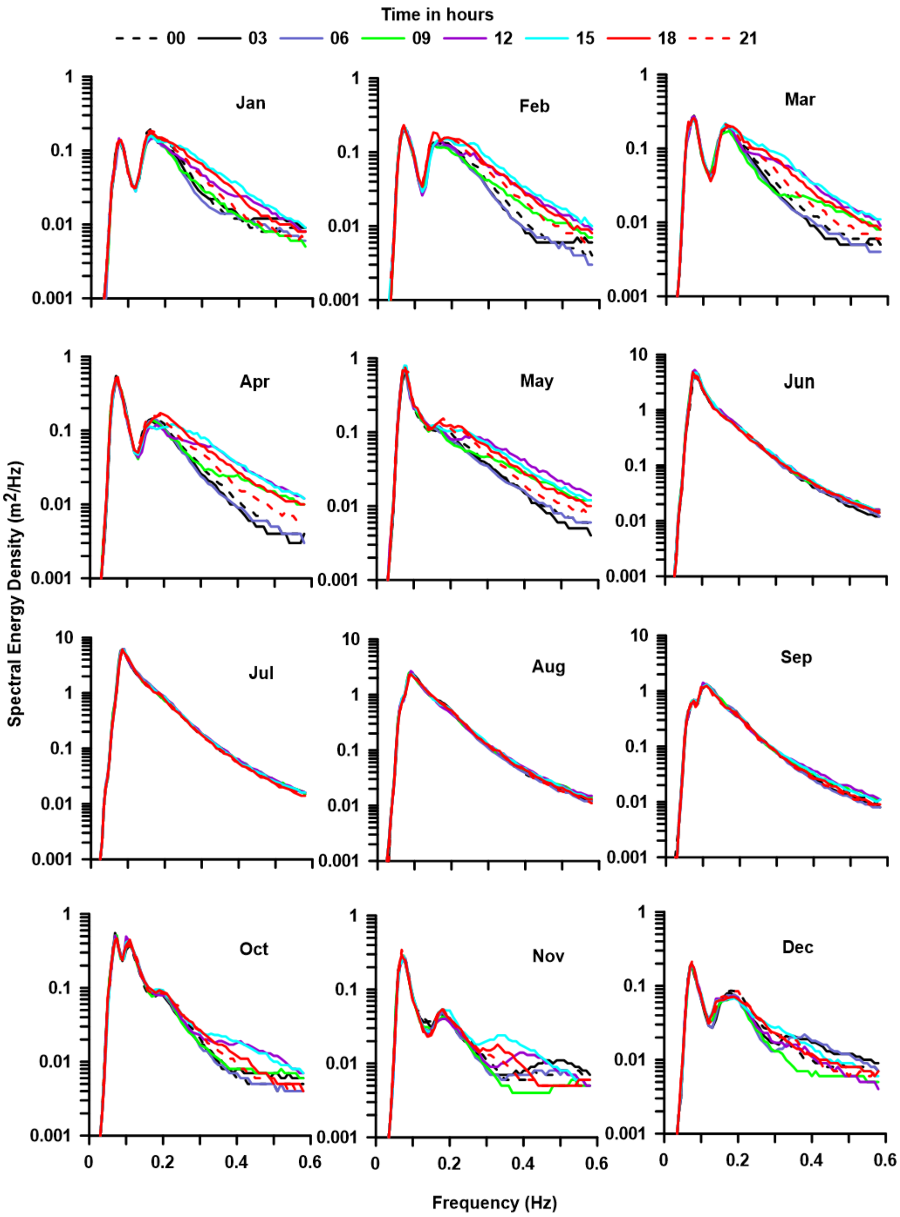

Figure 3.13 Monthly averaged wave spectra at every 3 hours in a day during 2014 at Karwar

3.5.3 Honnavar

The diurnal variation in wave spectra at Honnavar also shows an increase in energy during 15-18 hrs during the pre-monsoon season (Figure 3.14). Here the variation is more during April, where the energy increases from 0 hrs (0.081 m^2/Hz) to its maximum value at 18 hrs (0.172 m^2/Hz) with a total increment of 0.032 m^2/Hz. During March, there is an increase of 0.017 m^2/Hz of energy from 0 hrs (0.1 m^2/Hz) to 18 hrs (0.117 m^2/Hz). In February, though, the spectral energy initially decreases from 0 hrs (0.102 m^2/Hz) to 12 hrs (0.729 m^2/Hz) and then increases to its maximum at 18 hrs (0.105 m^2/Hz), and the total increment in energy from 0 hrs to 18 hrs is less (0.003 m^2/Hz). So here, the effect of the sea breeze is stronger in April.

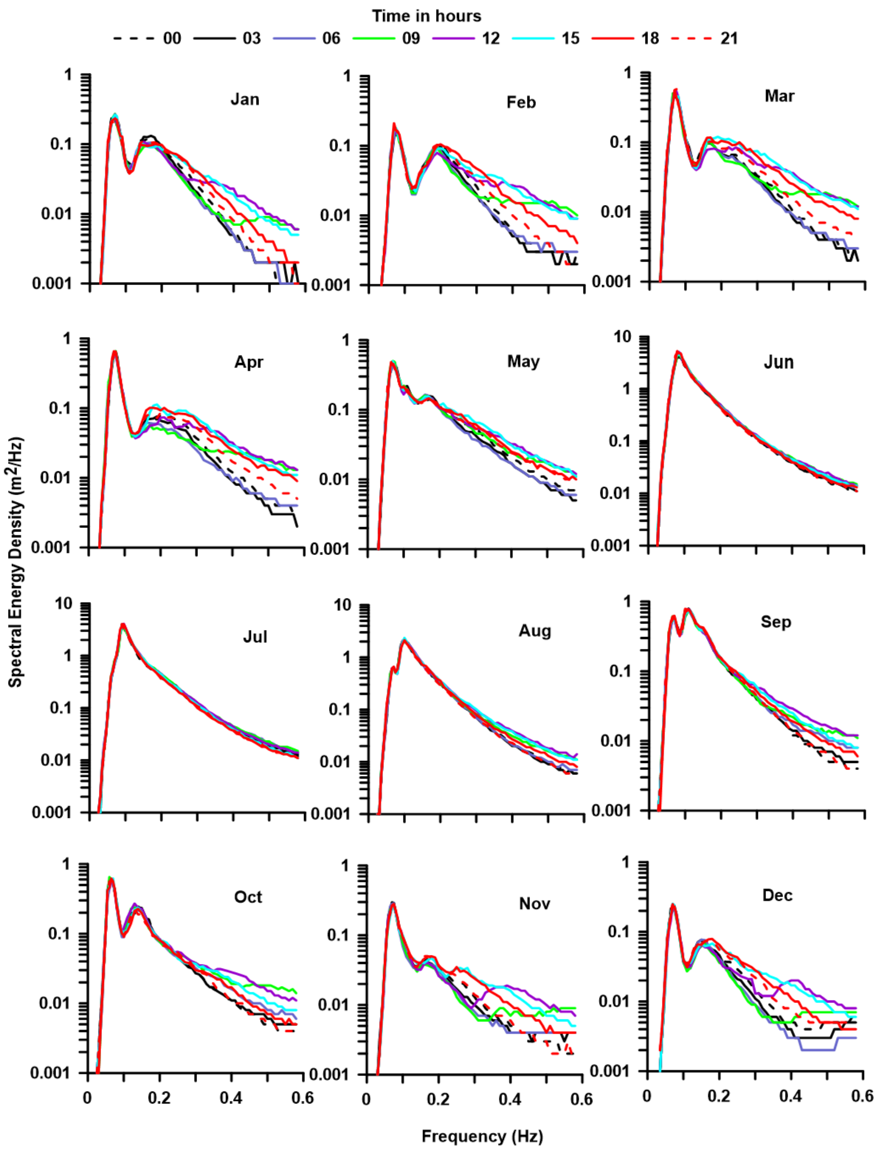

Figure 3.14 Monthly averaged wave spectra at every 3 hours in a day during 2015 at Honnavar

3.5.4 Gangavaram

The monthly average spectra at every 3 hours at the location Gangavaram, off the east coast (Figure 3.15), show that the diurnal variation pattern is not much different from the west coast, with high variations during the pre-monsoon period. Here the variations are high in April with an increment of 0.129 m^2/Hz from 0 hrs to 18 hrs and least during February (0.01 m^2/Hz). The maximum energy observed during March and April is at 18 hrs, whereas during February, the energy density reaches its peak value at 12 hrs (0.078 m^2/Hz).

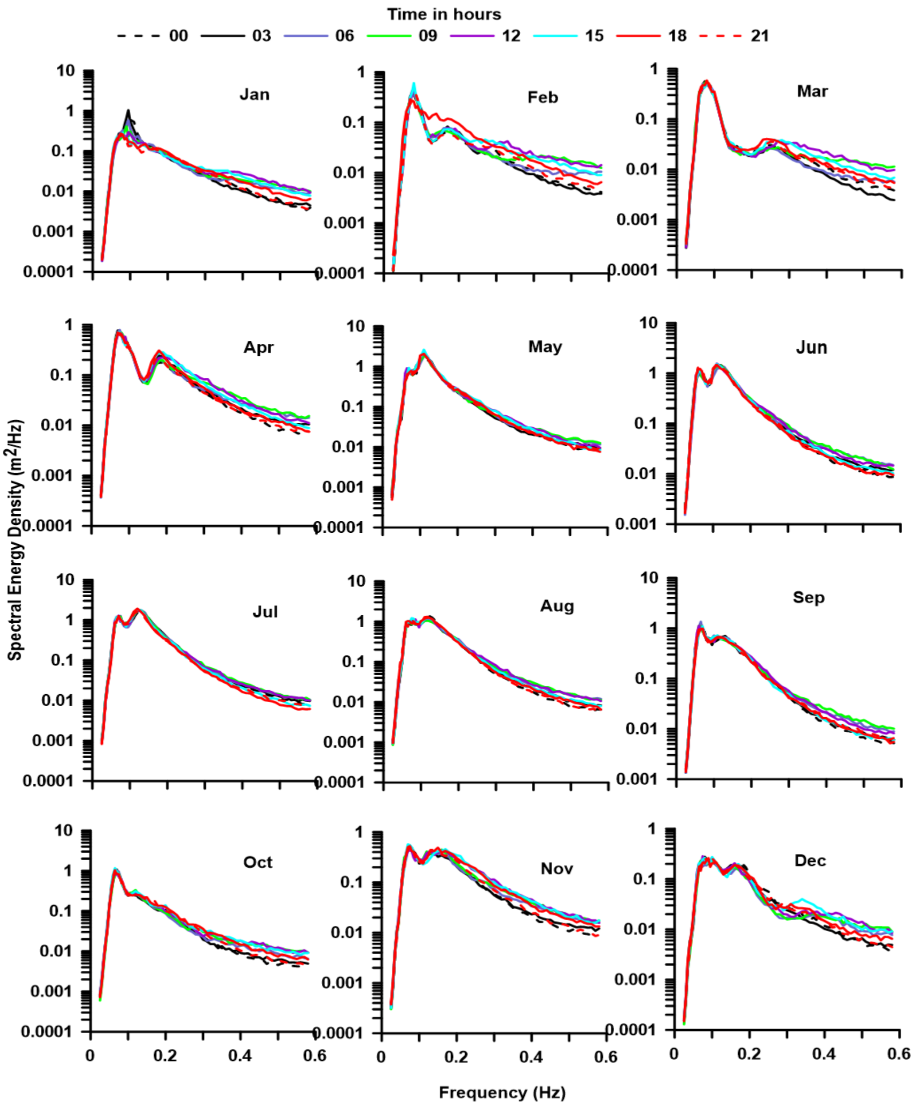

Figure 3.15 Monthly averaged wave spectra at every 3 hours in a day during 2015 at Gangavaram

3.5.5 Gopalpur

The monthly average spectra at the location Gopalpur off the east coast (Figure 3.16) shows high wind-sea energy and large diurnal variation during the pre-monsoon period. It can be seen that the wind-sea energy is very high during April and is almost equal to the swell energy. During February, March, and April, the wind-sea energy increases from 0 hrs to reach its peak at 12 hrs. The maximum diurnal variation occurs during April with an increment of 0.304 m^2/Hz, from 0 to 12 hrs. The wind-sea energy observed during April at 12 hrs is 0.608 m^2/Hz, which is the highest value compared to all other locations. During February, the wind-sea energy increases by 0.128 m^2/Hz from 0 hrs to 12 hrs.

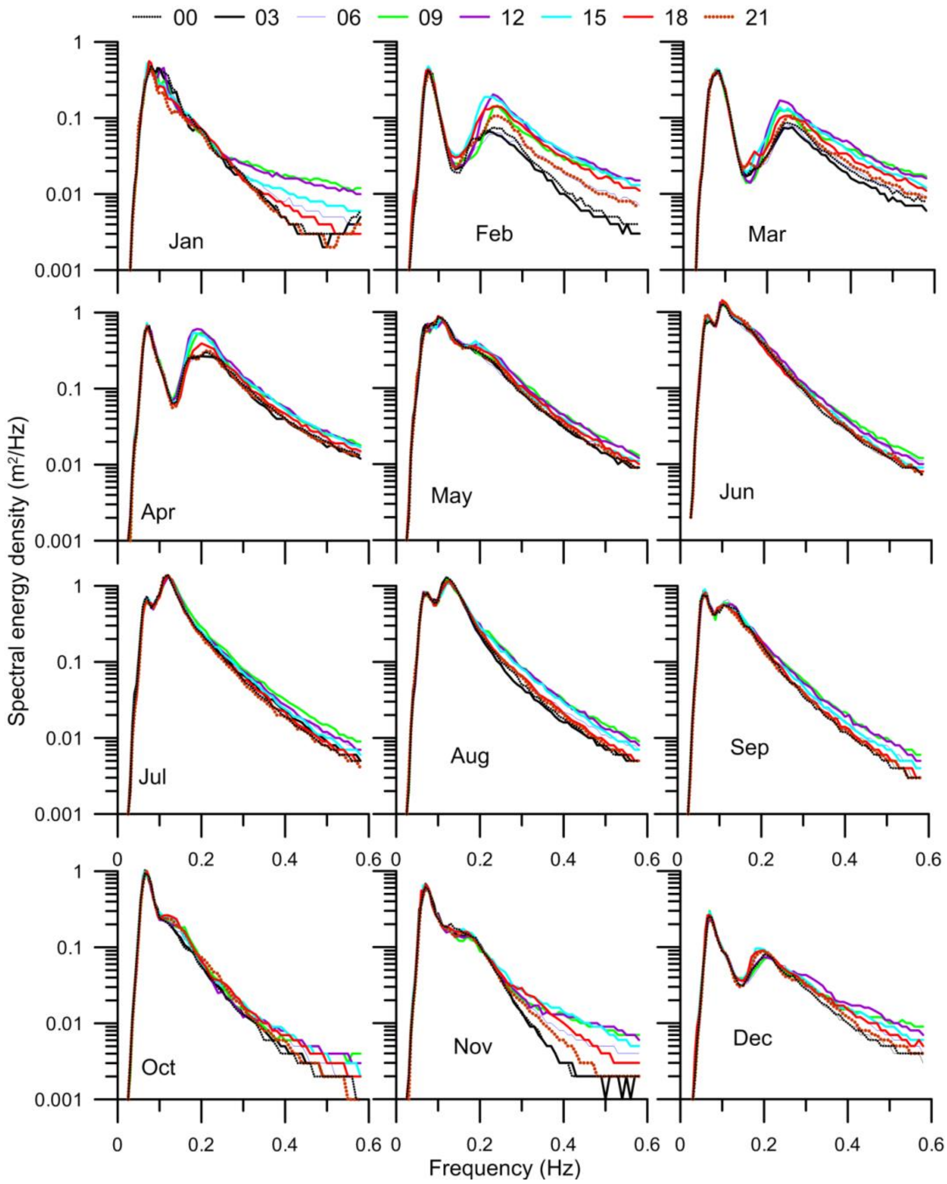

Figure 3.16 Monthly averaged wave spectra at every 3 hours in a day during 2015 at Gopalpur

While comparing all the locations, it can be seen that the diurnal variation, as well as the wind-sea energy, are high off the east coast compared to the west coast, and the maximum diurnal variation is observed during the month of April. Considering the three locations off the west coast, maximum diurnal variation is observed at Ratnagiri during March. The energy maximum occurs between 15 and 18 hrs off the west coast, whereas off the east coast, the maximum energy occurs between 12 and 18 hrs. For the two locations off east coast and for Ratnagiri on the west coast, where the diurnal variation is found to be high, the buoys are moored at a distance less than 2 km from the coast. Since sea breeze is a coastal phenomenon whose strength decreases offshore, the impact of sea breeze on wave spectra could be high at these locations. Also, Ratnagiri and Gopalpur are the northern locations, and hence the energy of swells at this location will be slightly less compared to other locations. This makes the impact of the wind-sea more prominent.

3.6 Inter-annual variation in the wave spectrum

3.6.1 Ratnagiri

To describe the variation in the spectral energy density and mean wave direction over years, the monthly averaged spectra for different years are estimated (Figure 3.17). The monthly averaged wave spectrum indicates that the wave spectra are mainly single-peaked during June to August with peak frequency distributed around 0.08 Hz (T_p ~ 12.5 s) and mainly double-peaked during the remaining period except in September. In September, the swell peak is primarily at 0.1 Hz, and a secondary peak is observed at 0.07 Hz in 2013. From January to May and from October to December, the swell peak is around 0.07 Hz. The wind-sea peak during the non-monsoon period is mainly at 0.2 Hz except during March and April. In November 2011, the wind-sea peak is around 0.13 Hz.

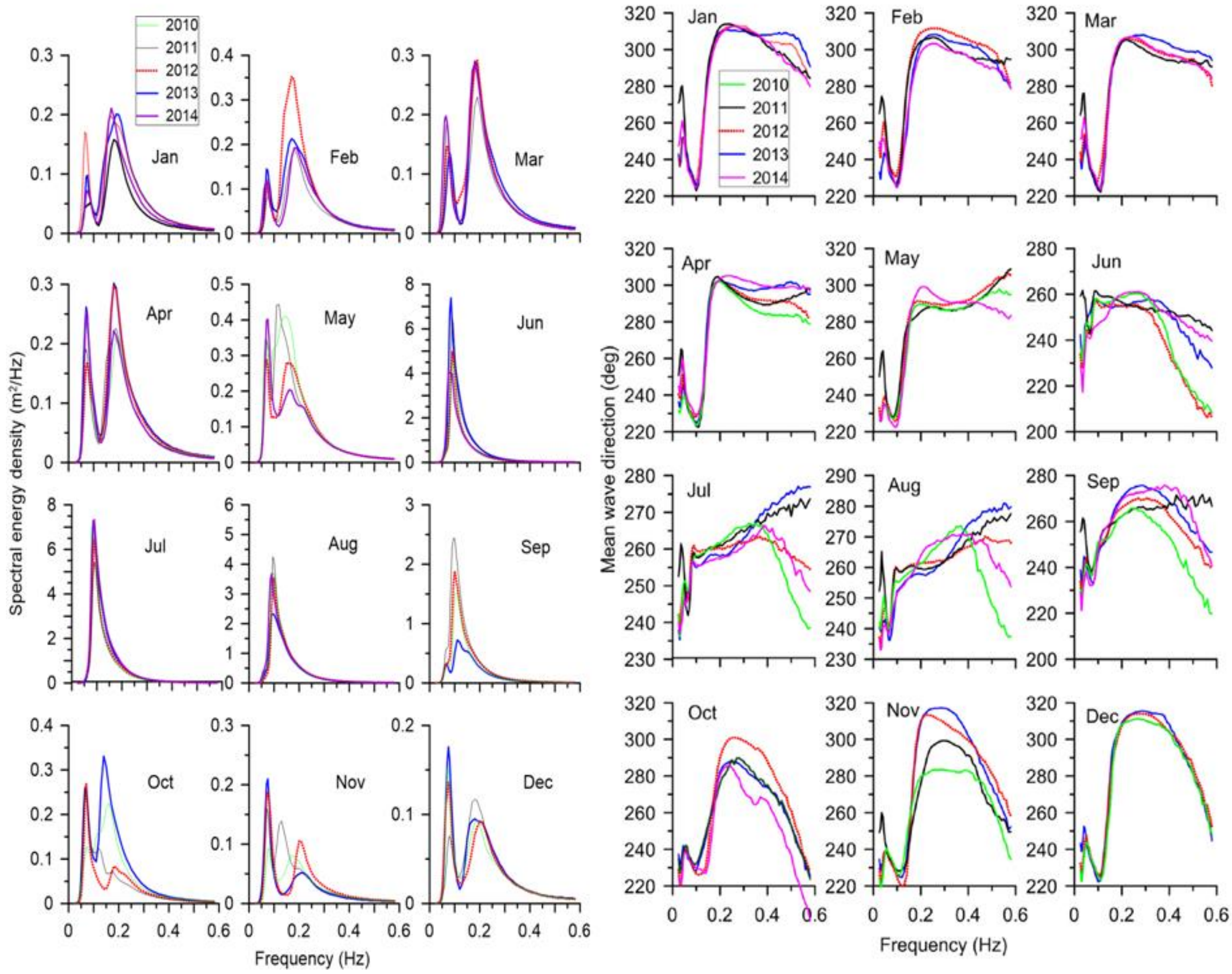

Figure 3.17 Monthly average wave spectra (3 columns in left) and monthly wave direction (3 columns in right) in different years at Ratnagiri

The inter-annual variations in the monthly average wave spectrum are high during February, May, and September to November (Fig. 3.17). Except in September, the variations in the wave spectrum are mainly due to the change in the wind-sea part of the spectrum caused by the inter-annual variations in the local wind. The wave energy level is the highest during June-August due to the monsoon. In June and July, single-peak spectra are with similar characteristics, and the waves are mainly the swells. In June, the swell heights are highest in 2013 compared to other months. The inter-annual variation in wave direction spectra are caused by the local wind conditions. Here the swells are always from the SW direction and wind-sea from NW.

3.6.2 Karwar

The inter-annual changes of wave spectral energy density for different months in the period 2011-2015 are studied by computing the monthly average wave spectra for all the years (Figure 3.18). As in the case of Ratnagiri, here also during the non-monsoon period, the wave spectra observed are double-peaked, indicating the presence of wind-sea and swells, whereas during the monsoon, due to the strong southwest winds, single peaked spectrum is observed, i.e., the swell peak with low-frequency and high spectral energy density. In the study area, from January to May and October to December, the swell peak is between the frequencies 0.07 and 0.08 Hz ($12.5 < Tp < 14.3$s), but in the monsoon period, the swell peak is around 0.10 Hz, in all the years studied. This shows the presence of long-period swells ($Tp > 13$s) in the non-monsoon period and intermediate period swells ($8 < Tp < 13$s) in the monsoon. Large inter-annual variations are observed for the monthly average wave spectrum in all months except in July. This is because July is known to be the roughest month over the entire annual cycle, and the southwest monsoon reaches its peak during July. Hence, the influence of temporally varying wind-sea on the wave spectrum is least during July compared to other months. Due to the early onset (on 1 June) and advancement of monsoon during 2013 compared to other years, the monthly average value of the maximum spectral energy is observed in June 2013 (Figure 3.18). The wave spectra of November 2011 is distinct from that of other years, with another swell peak at frequency 0.13 Hz due to the deep depression ARB04, which occurred south of India near Cape Comorin, during 26 November–1 December, with a sustained wind speed of 55 km/h. During October 2014, the second peak is observed at 0.11 Hz with comparatively high energy showing the influence of cyclonic storm NILOFAR. It is an extremely severe cyclonic storm that occurred during the period 25-31 October 2014, originated from a low-pressure area between the Indian and Arabian Peninsula, with the highest wind speed of 215 km/h, and affected the areas of India, Pakistan, and Oman. Significant inter-annual variation is observed in the wind-sea peak frequency. The inter-annual variation within the spectrum is more for the wind-sea region compared to the swell region. During the study period, the maximum spectral energy observed is during the 2011 monsoon. It is observed that throughout the year, the mean wave direction of the swell peak is southwest (200-250^{o}). In the non-monsoon period, the wind-sea direction is northwest (280-300°). This is due to the wind-sea produced by sea breeze which has the maximum intensity during the pre-monsoon season and *shamal* and *makran* winds.

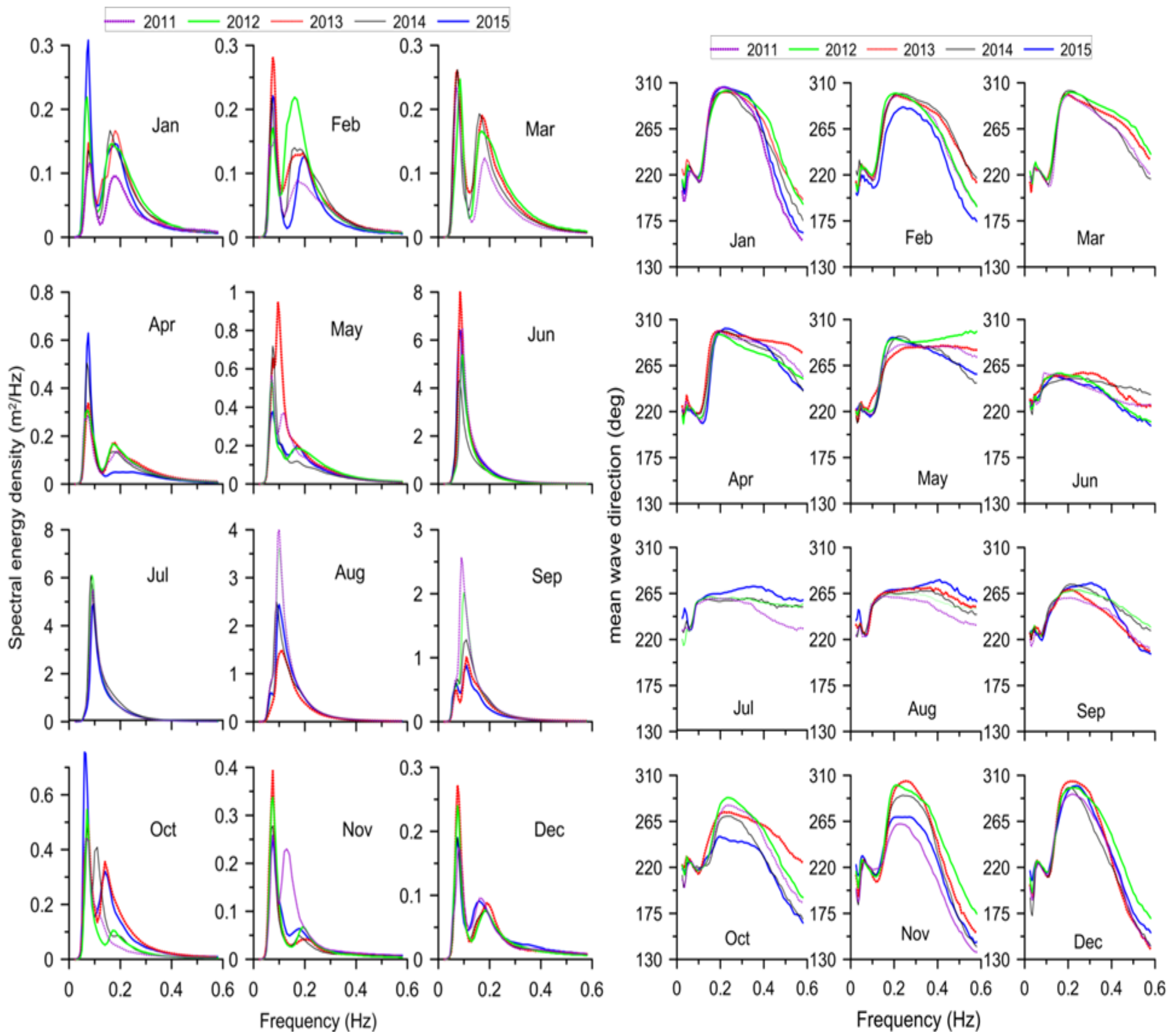

Figure 3.18 Monthly average wave spectra (left) and monthly wave direction (right) in different years at Karwar

3.6.3 Honnavar

The inter-annual variations in the monthly averaged wave spectrum for the location Honnavar from 2009 to 2012 are shown in Figure 3.19. The wind-sea part of the spectrum, which is dominant from January to May, shows inter-annual variation with high energy during 2012 compared to other years. This is due to the presence of relatively stronger winds with a magnitude of 8 m/s to 10 m/s observed during the pre-monsoon period of the year 2012. The high energy peak observed between 0.1 to 0.2 Hz during November 2009 is due to the influence of cyclonic storm 'Phyan.' Inter-annual variation observed in the wave spectrum are high during the months January-February, May, and October-November. The changes in the local wind and the swells from the Southern Ocean and the variation in monsoon intensity are the reasons for the observed inter-annual variations.

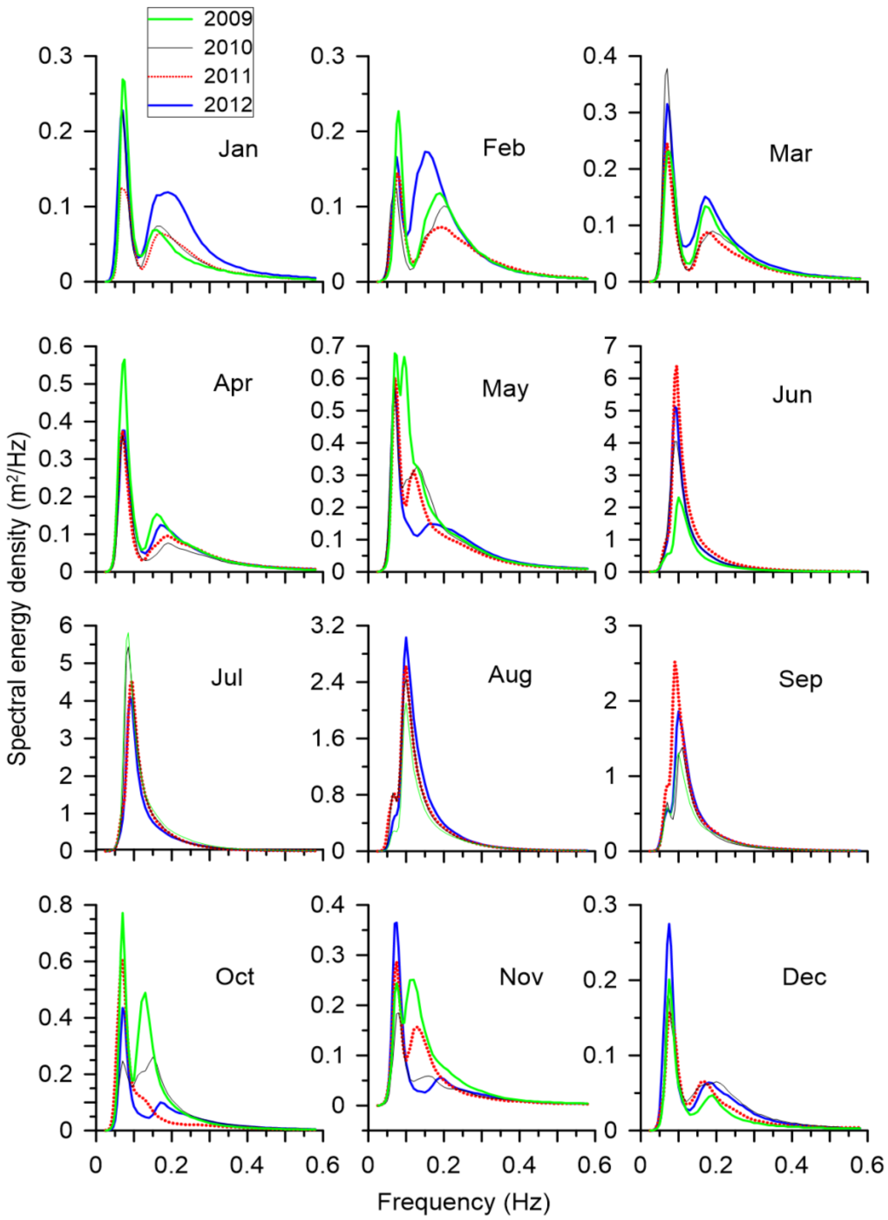

Figure 3.19 Monthly average wave spectra from 2009 to 2012 at Honnavar

3.6.4 Gangavaram

Figure 3.20 shows the inter-annual variations in wave spectra during the years 2012 and 2015. Unlike the west coast of India, here, the spectrum observed is double-peaked during all the months, including the monsoon period. The first peak observed during all the months is with frequency less than 0.1 Hz and from the direction SE (140° - 170°). The second peak observed during the monsoon period is between frequency 0.1 to 0.15 Hz with almost the same direction as the first peak (150° - 160°), whereas from October to February, the second peak observed is between 0.15 to 0.2 Hz from SE. During March and April, the second peak observed is at 0.2 Hz indicating the influence of wind-sea and the wind-sea energy is high during April. The energy density observed is very high during the monsoon period, with the maximum energy observed during June 2012 due to the strong winds of the southwest monsoon. Large inter-annual variation is observed in the energy density during these two years, and it is maximum during May because May is a transition month from fair weather period to monsoon. Large inter-annual variation in the wave direction at the high frequency region of the spectrum (between 0.2 Hz to 0.4 Hz) during the months March, October and December are due to the variation in local winds. Since the 2012 monsoon is a relatively stronger one, the wave energy density during the monsoon period is higher for 2012, except during the month of July. This is due to a hiatus that occurred in monsoon for about 11 days from 22 June – 2 July, and a break-like situation prevailed in the monsoon, from 25th -29th June during the year 2012 (IMD, 2012). Due to the occurrences of cyclonic activities, the spectrum observed during November is irregular.

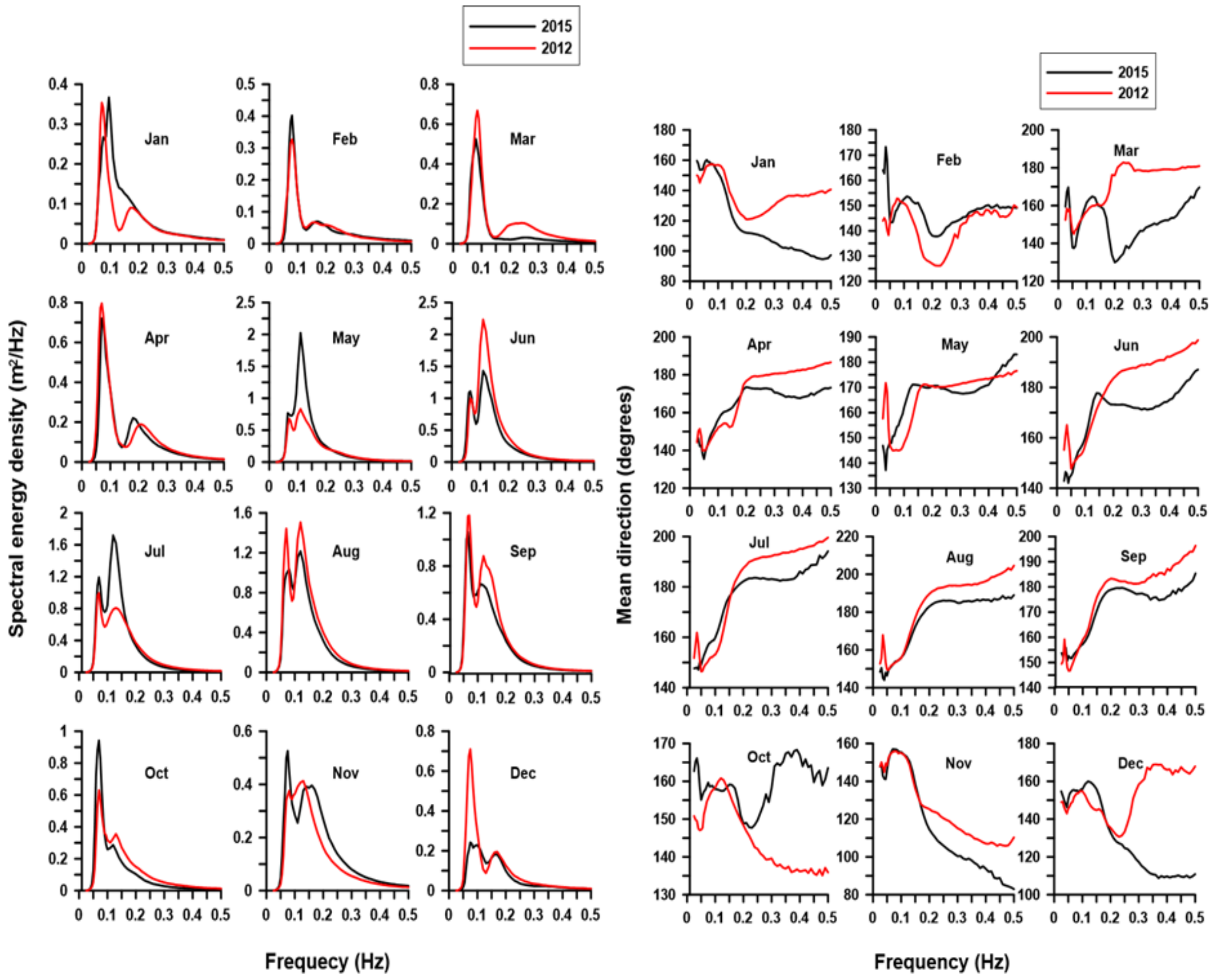

Figure 3.20 Monthly average wave spectra (left) and monthly wave direction (right) during 2012 and 2015, at Gangavaram

3.6.5 Gopalpur

The inter-annual variation in wave spectra at the location Gopalpur is studied using the data for 2013 to 2015 (Figure 3.21). Large inter-annual variations are observed in October due to the occurrence of TCs. The maximum spectral energy density observed is during October 2013 (> 4 m^2/Hz) due to the influence of the cyclonic storm Phailin. Wind-sea peaks are between 0.2 and 0.4 Hz and are significant in February, March, and April. Maximum wind-sea energy for the non-monsoon period is observed during April from south. During the southwest monsoon period, the maximum energy observed is during July 2013, due to the relatively stronger monsoon in 2013.

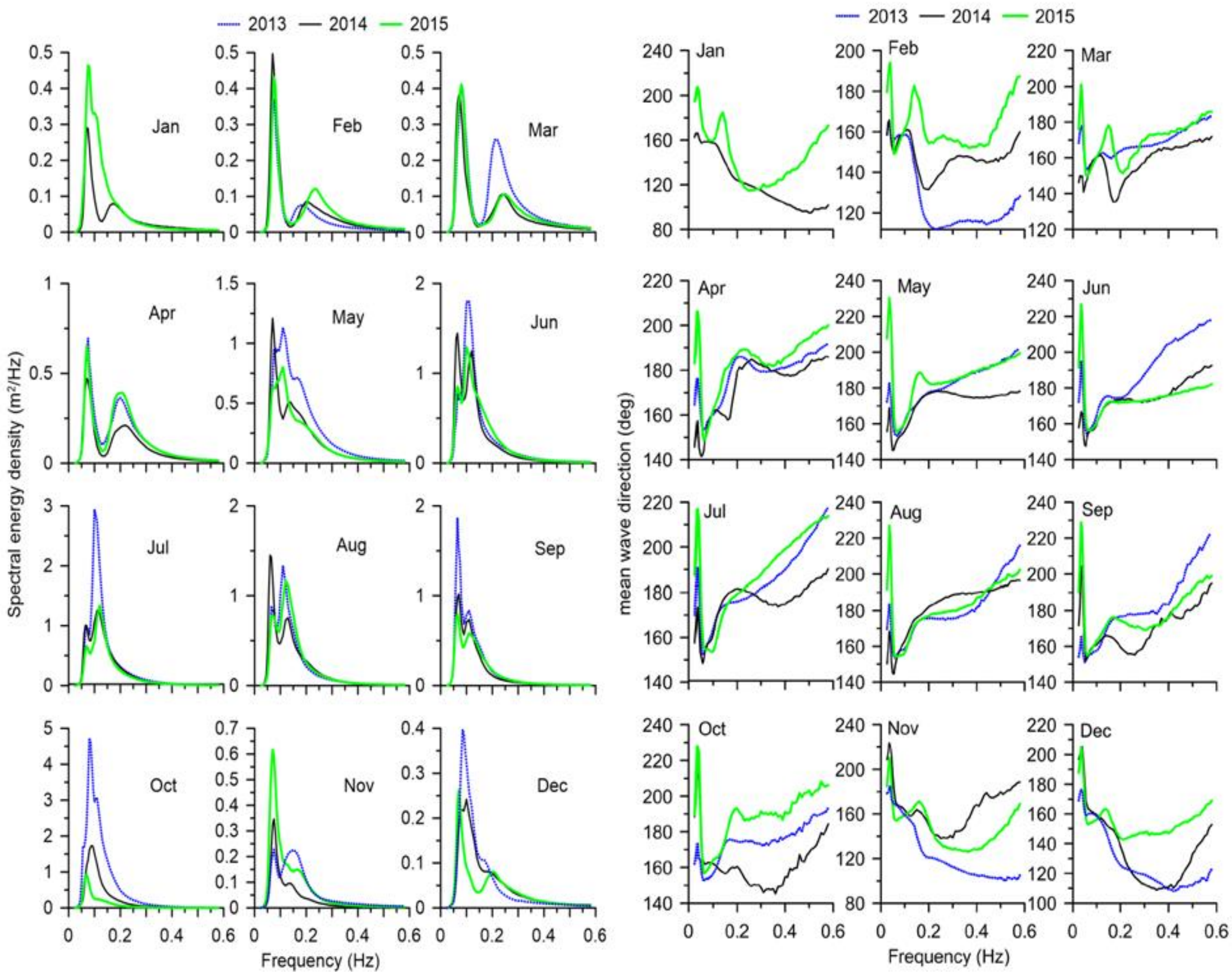

Figure 3.21 Monthly average wave spectra (left) and monthly wave direction (right) in different years at Gopalpur

3.7 Slope of the wave spectrum

The slope of the high-frequency part of the spectrum estimated using the method of the best fitting curve for the monthly averaged spectrum during 2015 for all five locations are given in Table 3.3. Here the slope is estimated for the frequency region above 0.2 Hz. The slope of the spectrum obtained for all the five locations shows that the slope is steep (~ -3) during the monsoon time since wave energy is high. Also, the value of slope in the range -3 is also obtained during some months in the pre-monsoon period. This is because of the high-energy wind-sea generated during that period.

Table 3.3 Slope (exponent) of the high-frequency region estimated for monthly averaged spectra for all the five locations during 2015

Months	**Slope parameter**				
	Ratnagiri	**Karwar**	**Honnavar**	**Gopalpur**	**Gangavaram**
Jan 2015	-3.03	-2.57	-3.46	-2.03	-2.16
Feb 2015	-3.22	-2.93	-2.62	-2.98	-1.86
Mar 2015	-2.94	No data	-2.79	-2.75	-2.09
Apr 2015	-2.92	-2.61	-2.68	-3.29	-2.85
May 2015	-2.86	-2.61	-2.62	-3.46	-3.07
Jun 2015	-3.55	-3.56	-3.51	-3.59	-3.01
Jul 2015	-3.63	-3.65	-3.46	-3.73	-3.30
Aug 2015	-3.41	-3.60	-3.49	-3.60	-3.23
Sep 2015	-3.03	-2.94	-2.95	-3.67	-3.12
Oct 2015	-2.40	-2.51	-2.43	-3.16	-2.33
Nov 2015	-2.19	-1.32	-1.83	-2.76	-2.84
Dec 2015	-2.72	-1.71	-2.04	-2.79	No data

Chapter 4: Evolution of wave spectra during sea breeze and land breeze

4.1 Introduction

The evolution of wave spectrum during sea-land breeze cycle is investigated by examining the relative roles of various source terms involved in the evolution process. This chapter mainly deals with the temporal and spatial variation in source terms during sea breeze and land breeze phase, simulated using SWAN wave model.

4.2 Model validation

The wave parameters (H_{m0} and T_{m02}) obtained from the SWAN wave model, for various friction and white-capping schemes (as mentioned in chapter 2) are compared with measured data at 9m depth of Honnavar. Figures 4.1 a & c shows the comparison of H_{m0} and T_{m02} from all the four model runs (I to IV) with the measured data and the statistical parameters of comparison are tabulated in Table 4.1. From Figures 4.1 a & c, it can be seen that there is no much variation in the H_{m0} obtained from different model runs. The values of RMSE calculated for different model runs are almost the same in the case of H_{m0} but differs significantly in the case of T_{m02}. In the SWAN hindcast described by Rogers et al. (2003), it has been observed that SWAN underestimates structurally the mean or peak wave periods by 10 to 20%. The change of value of δ from 0 to 1 by Rogers et al. (2003) was actually implemented to improve the prediction. From table 4.1, it can be seen that the value of RMSE for mean wave period are less for run I and run III, where the value of δ is 1. Whereas the RMSE value is high for run IV, where a white-capping scheme based on Alves and Banner (2003) is used. This is because the white-capping scheme proposed by Alves and Banner (2003) depends on spectral mean wave number and steepness, which may cause errors in situations of mixed sea and swell, especially in nearshore regions. Since the RMSE between measured and modelled values of H_{m0} and T_{m02}, is the least for Run III, it is used in further analysis.

4.3 Identification of a sea breeze event

The effect of the sea breeze in the coastal regions of India is significant from November to May. Waves generated under the influence of sea breeze will be characterised by high H_{m0} and low T_{m02}. Figures 4.1b shows the variation in H_{m0}, T_{m02} and wind speed during a period of 10 days in March 2015. Wind vector for the same period (22 March 2015 00:00 h to 1 April 2015 00:00 h) is shown in Figure 4.2. One significant sea-land breeze cycle, with high H_{m0} and wind speed accompanied by low T_{m02} is observed on 27 March 2015 (Figure 4.1b). Hence, this sea-land breeze cycle is selected for further study. The diurnal variations in H_{m0}, T_{m02} and wind speed on 27 March 2015 are shown in Figure 4.1d. Here the wind speed is found to increase to reach a maximum (6.47 m/s) at around 12:00 h and then decreases, indicating a sea-land breeze cycle.

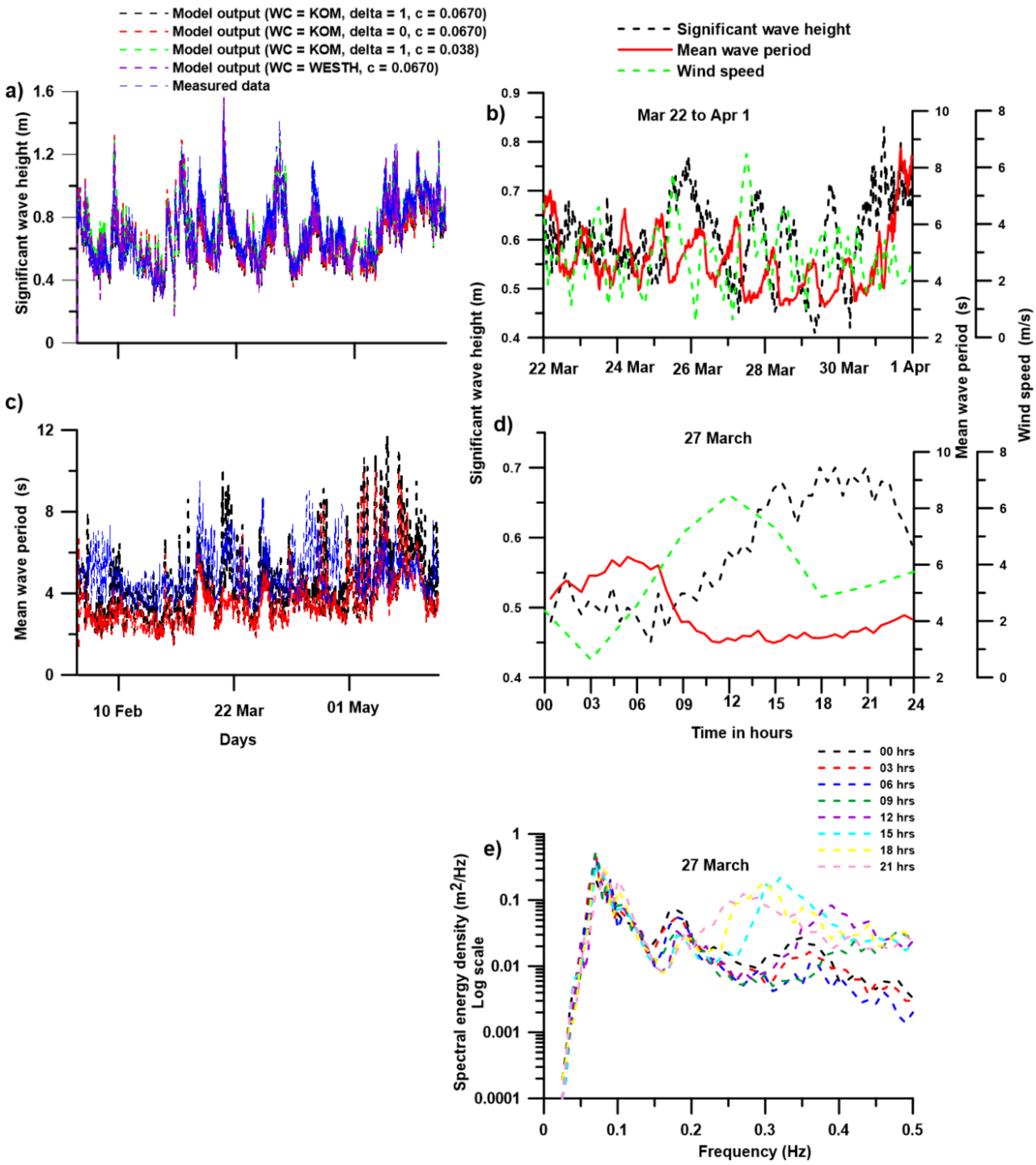

Figure 4.1 Left panel shows the comparison of measured data with model output with different model parameters; a) H_{m0} and c) T_{m02}. Right panel shows the variation in H_{m0}, T_{m02} and wind speed b) from 22 March 2015 00 h to 1 April 2015 00 h, d) on 27 March 2015 and e) spectral energy density at different time on 27 March 2015.

Table 4.1 Statistical parameters for comparison of different model runs with measured data

Statistical parameters		RUN I	RUN II	RUN III	RUN IV
Correlation coefficient	H_{m0}	0.85	0.83	0.86	0.86
	T_{m02}	0.40	0.41	0.43	0.67
Bias	H_{m0} (m)	-0.04	-0.01	0.01	-0.01
	T_{m02} (s)	-0.53	-1.35	-0.23	1.21
RMSE	H_{m0} (m)	0.11	0.11	0.10	0.10
	T_{m02} (s)	1.64	1.85	1.65	2.45
Scatter Index	H_{m0}	0.15	0.15	0.14	0.14
	T_{m02}	0.33	0.37	0.33	0.49

The impact of the sea breeze on the wave spectrum can be seen as the growth and decay of the wave spectrum over time in a day. Figure 4.1e shows the wave spectrum at every 3 h interval on 27 March 2015. Here the wave spectra observed have one major peak at a frequency less than 0.1 Hz (swell peak) and two minor peaks at higher frequencies (wind-sea peak). The wind-sea peaks tend to vary significantly over time. It can be seen that at 12 h, an energy peak develops at around 0.4 Hz and it continues to develop to its maximum energy till 15 h and then decays as the wind speed reduced to 2.8 m/s. The increase in energy from 9 to 15 h followed by a decrease from 15 to 21 h in the wind-sea frequency region of the wave spectrum (Figure. 4.1e) is related to the wind speed intensification due to sea breeze and hence marks the impact of sea breeze on wave spectrum.

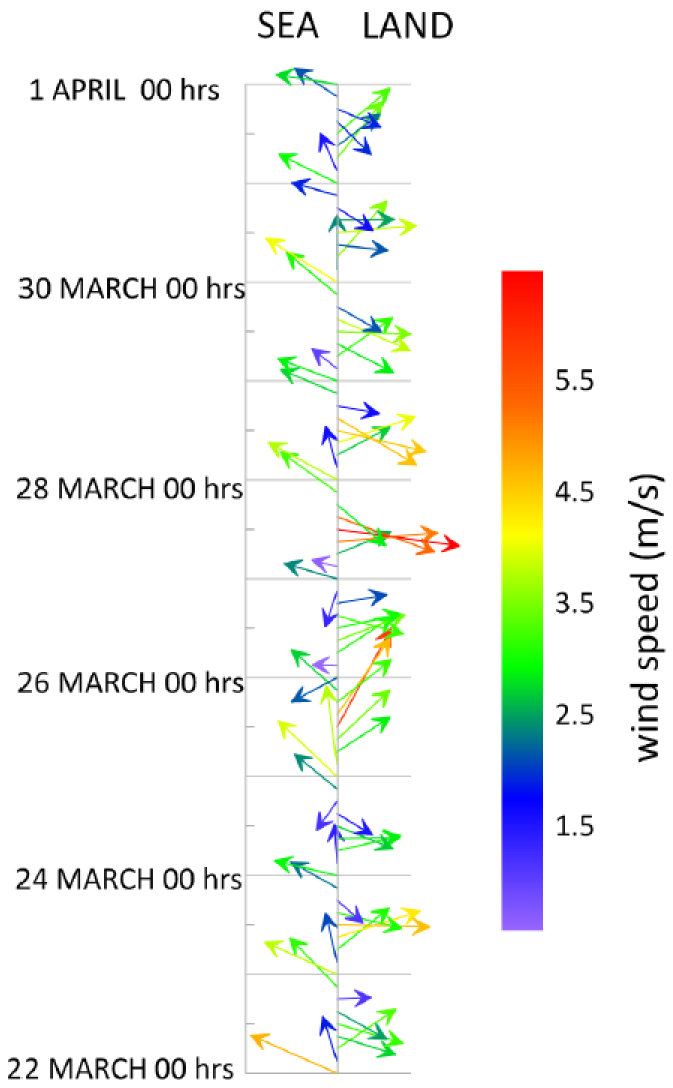

Figure 4.2 Wind vector from 22 March 2015 00:00 hrs to 1 April 2015 00:00 hrs. The colour code indicates the wind speed

4.4 Spectral evolution during sea breeze

The evolution of wave spectra under the influence of wind involves various energy transfer mechanisms like energy input from wind, transfer of energy between different wave components through nonlinear interaction and dissipation due to processes like white-capping, breaking and friction. These processes contribute to the total energy of the wave spectrum and are regarded as the source terms. The various source terms obtained from SWAN at the time of maximum wind speed, during the onshore phase (sea breeze) of the above-mentioned sea-land breeze cycle are shown in Figure 4.3. The figure shows the source terms like variance density, wind input (S_{in}), dissipation through white-capping (S_{ds}), and quadruplet interactions (S_{nl4}) distributed over the frequency and direction domain at 12 h when the wind speed is maximum.

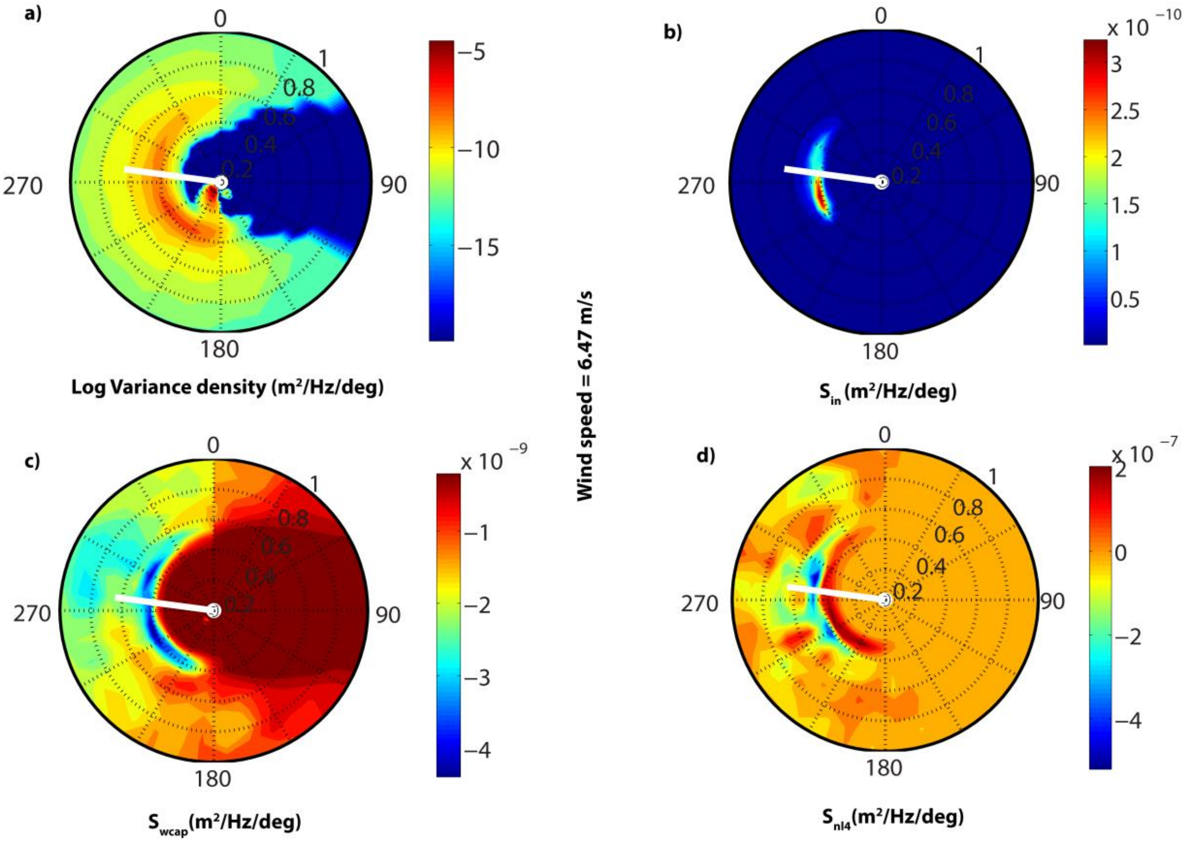

Figure 4.3 Source terms from SWAN model on 27 March 2015 at 12:00 hrs (a) Variance density (log scale), (b) Wind input, (c) Dissipation due to white-capping and (d) Energy transfer due to non-linear interaction (wind direction is shown as white arrows)

At 12 hrs, the wind direction is from the west, indicating that the winds are blowing towards the coast. The wind vector is indicated with white arrow in Figure 4.3. The spectrum for variance density shows two peaks, one at a lower frequency ($f < 0.1$ Hz), representing swells from the southwest direction and the other at higher frequency ($f \sim 0.4$ Hz), representing wind-sea from the west (Figure 4.3a). The wind input term is also from the west, with its maximum energy concentration between west and southwest direction at high frequencies (Figure 4.3b) due to the influence of the sea breeze. It can be seen that the region of high wind input occurs at 0.4 Hz in the direction bin 240° to 300°, with its peak at 240° to 270° (Figure 4.3b). Figure 4.3c shows that it is also in the same frequency and direction bin of 240° – 300°, the magnitude of energy loss due to white-capping and spread through non-linear interactions is high (Figure 4.3d). White-capping is a type of wave dissipation that depends on the steepness of the waves and, thereby, wind input. The generated wind-sea also has significant energy in spectral components travelling in directions away from the peak wind-sea direction (Figure 4.3a).

The evolution of source terms over time during sea breeze is shown in Figure 4.4. The figure shows the variations in variance density, wind input and non-linear interactions over a frequency-direction domain from 9 hrs to 18 hrs. Also, the change in wind pattern is shown using the wind vector. From 9 hrs to 18 hrs, the wind direction is from the northwest and it is towards the coast. The wind speed increases from 9 hrs and reaches a maximum speed (6.47 m/s) at 12 hrs and then decreases, indicating that the sea breeze, which starts in the early morning hours, intensifies at 12 hrs and then weakens. At 18 hrs, the strength of the sea breeze is very low and thereafter, the wind direction changes. The wind input term is very sensitive to the changes in the wind pattern. Energy from wind input is present only when the wind speed is considerably high (12–15 hrs). The wind input energy at 12 hrs is concentrated in the southwest-northwest directional bin, which shifts to the west-northwest directional bin at 15 hrs. Energy from wind input is zero when the wind speed reduces to 2.85 m/s. The energy of the wind-sea peak in the variance density spectrum is also high when the influence of the sea breeze is strong.

The one-dimensional wave spectra of source terms during the sea breeze phase indicate the relative roles of source terms at different frequencies (Figure 4.5). It can be seen that the energy transfer from wind input is always positive, whereas the energy transfer from non-linear interactions has both positive and negative phases. It shows that due to non-linear interactions, energy is lost at certain frequency bins, whereas energy is gained at other bins. Thus non-linear interactions enable the distribution of energy between various frequency bins. The energy from wind input is maximum at 12 hrs (Figure 4.5b) and lies in the frequency bin 0.4 Hz–0.5 Hz. But the wind-sea peak in the variance density spectrum reaches its peak at 15 hrs and with its maximum energy between 0.2 Hz and 0.4 Hz (Figure 4.4a). This is due to the influence of non-linear interactions which become stronger at 15 hrs (Figure 4.5c). At 12 hrs and 15 hrs (Figure 4.5 b & c), the maximum energy loss due to non-linear interactions occurs between 0.4 and 0.5 Hz (region of high wind input) and maximum energy gain between 0.2 and 0.4 Hz. During other times, maximum energy loss due to non-linear interactions occurs at frequencies greater than 0.6 Hz. The energy gain at a higher frequency from wind input is transferred to lower frequencies through non-linear interactions.

The magnitude of energy loss (dissipation) due to white-capping observed here is negligibly small. Maximum wind input is observed during 12 hrs when wind speed is maximum.

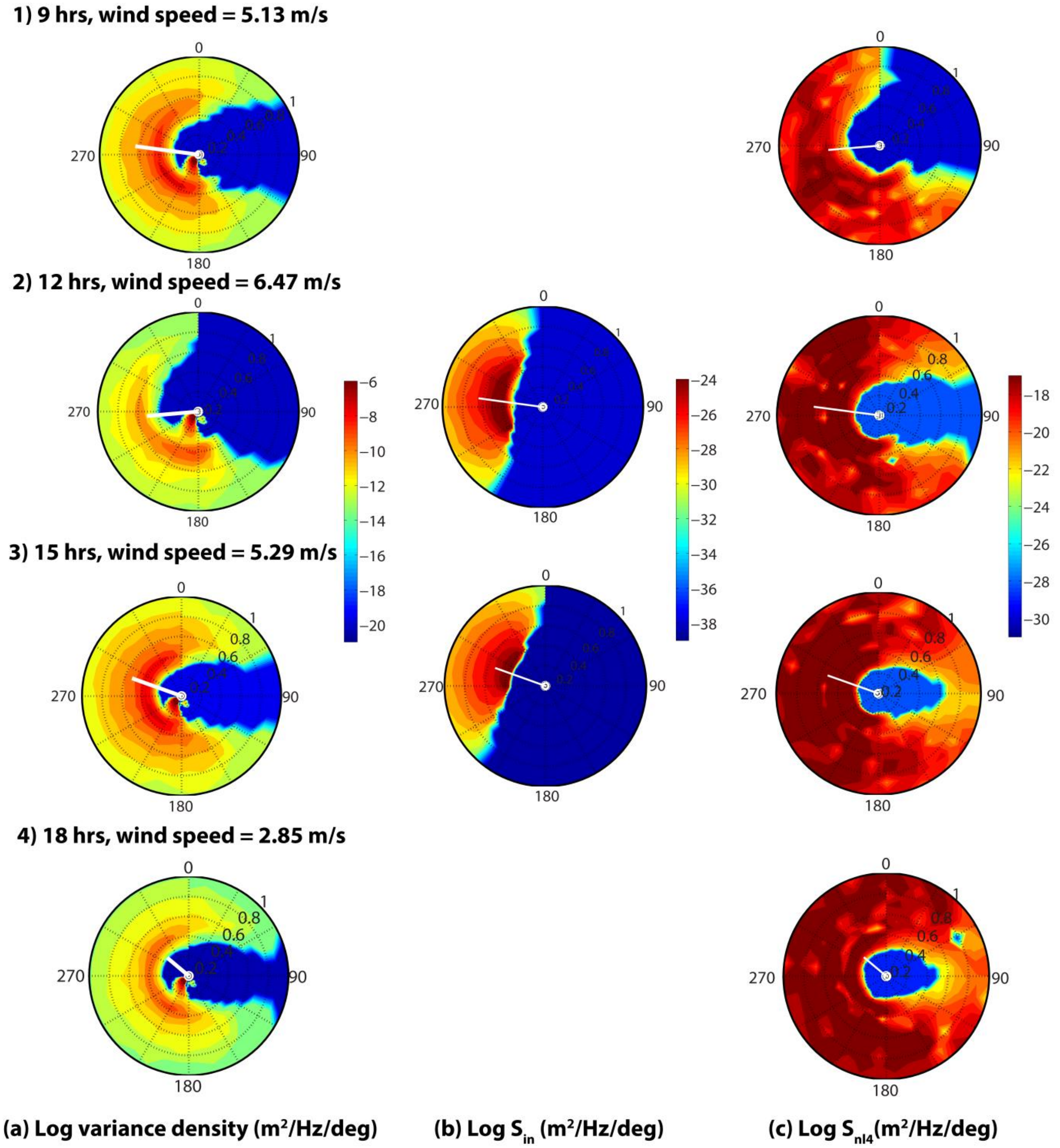

Figure 4.4 Source term variation from 9 hrs to 18 hrs on 27 March 2015. (a) log variance density, (b) wind input and (c) non-linear interactions

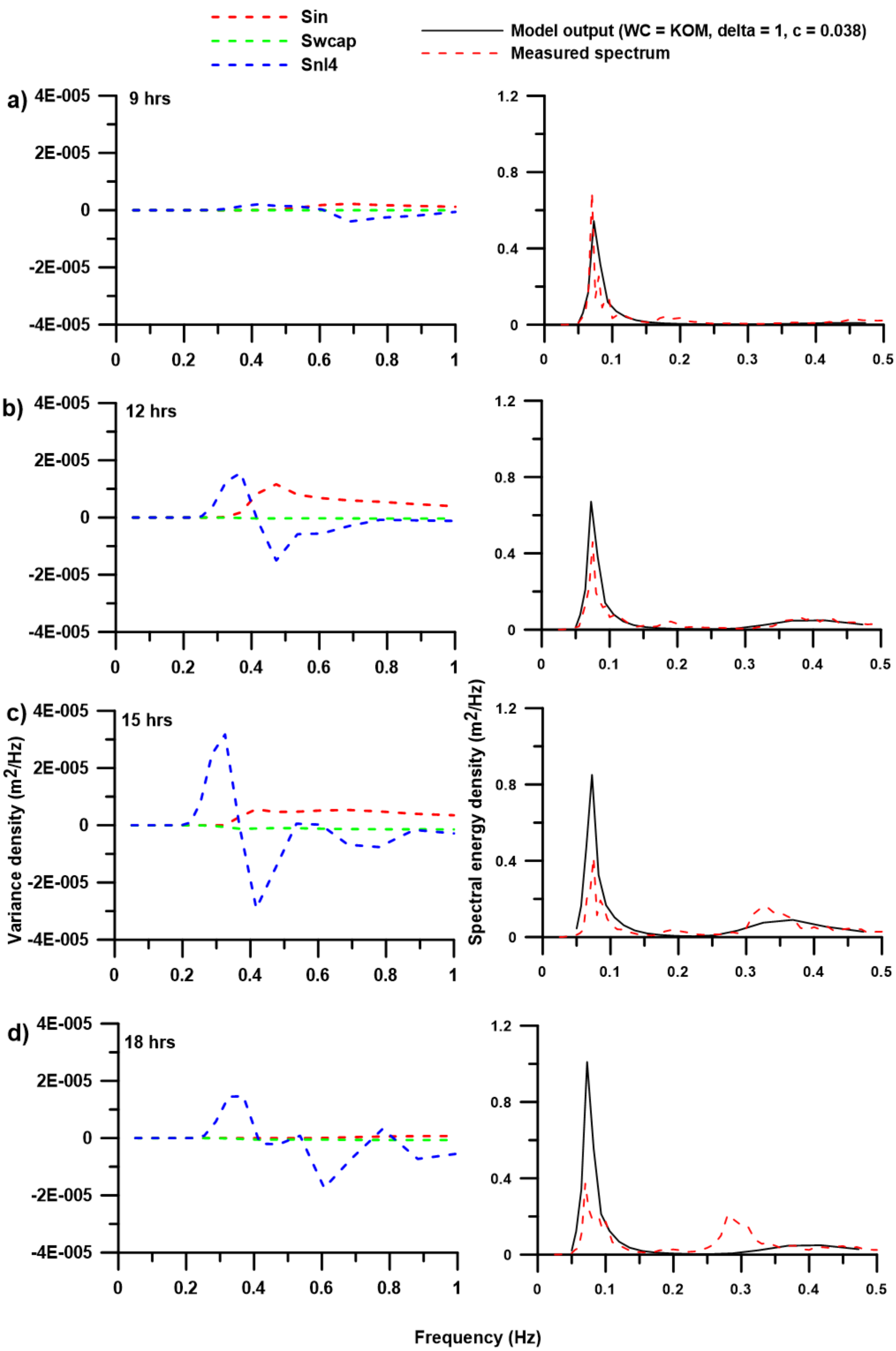

Figure 4.5 Left panel shows the one dimensional spectra of source terms during sea breeze phase on 27 March 2015. Right panel shows the comparison of measured and modelled wave spectra during the corresponding time.

The modelled one-dimensional wave spectrum at 9 m is compared with the measured wave spectrum at different stages of a sea-land breeze cycle (Figure 4.5). Both the modelled and measured wave spectrum are double-peaked. The peak frequency of swells from the model run matches well with the measured swell frequency, whereas wind-sea peak frequency differs. But even in the case of swells, the magnitude of energy density between modelled and measured wave spectra varies. The modelled energy density over-predicts except for 9 hrs when the wind speed is maximum. At 12 hrs, the modelled wind-sea match well with the measured one. The over-prediction of swell peak by model can be due to error in estimation of swell wave dissipation by bottom friction.

4.5 Spectral evolution during land-breeze

Figure 4.6 shows the variation in source terms during the land-breeze phase of the day. Here the wind direction which is marked as a white arrow is between 90^o to 180^o, that is from the SE direction indicating that the wind is blowing from the shore towards the sea. Since the wind speed is very low, there is no significant energy input from wind. The variance density spectrum during 0 hrs and 3 hrs, shows that (Figure 4.6a) the wind-sea peak is from south and not from the direction of wind. Whereas at 21 hrs, though the peak of the wind-sea is from south, wind-sea energy is distributed in the west and north directions. This is due to the transfer of energy generated by sea breeze wind, through non-linear interactions. Figure 4.6c shows that the energy transfer due to non-linear interaction at 21 hrs is high in the above-mentioned directions.

The one-dimensional spectra of source-terms during the land-breeze phase indicates that, the energy from wind input and white capping is zero and it is only the non-linear interactions that is responsible for energy transfer within the spectrum (Figure 4.7). Due to non-linear interactions, energy gain mainly occurs at 0.4 Hz. At 0 hrs and 3 hrs, energy loss due to non-linear interactions is comparatively less, whereas at 21 hrs there is a significant energy loss at 0.6 Hz and gain at frequencies between 0.3 and 0.4 Hz.

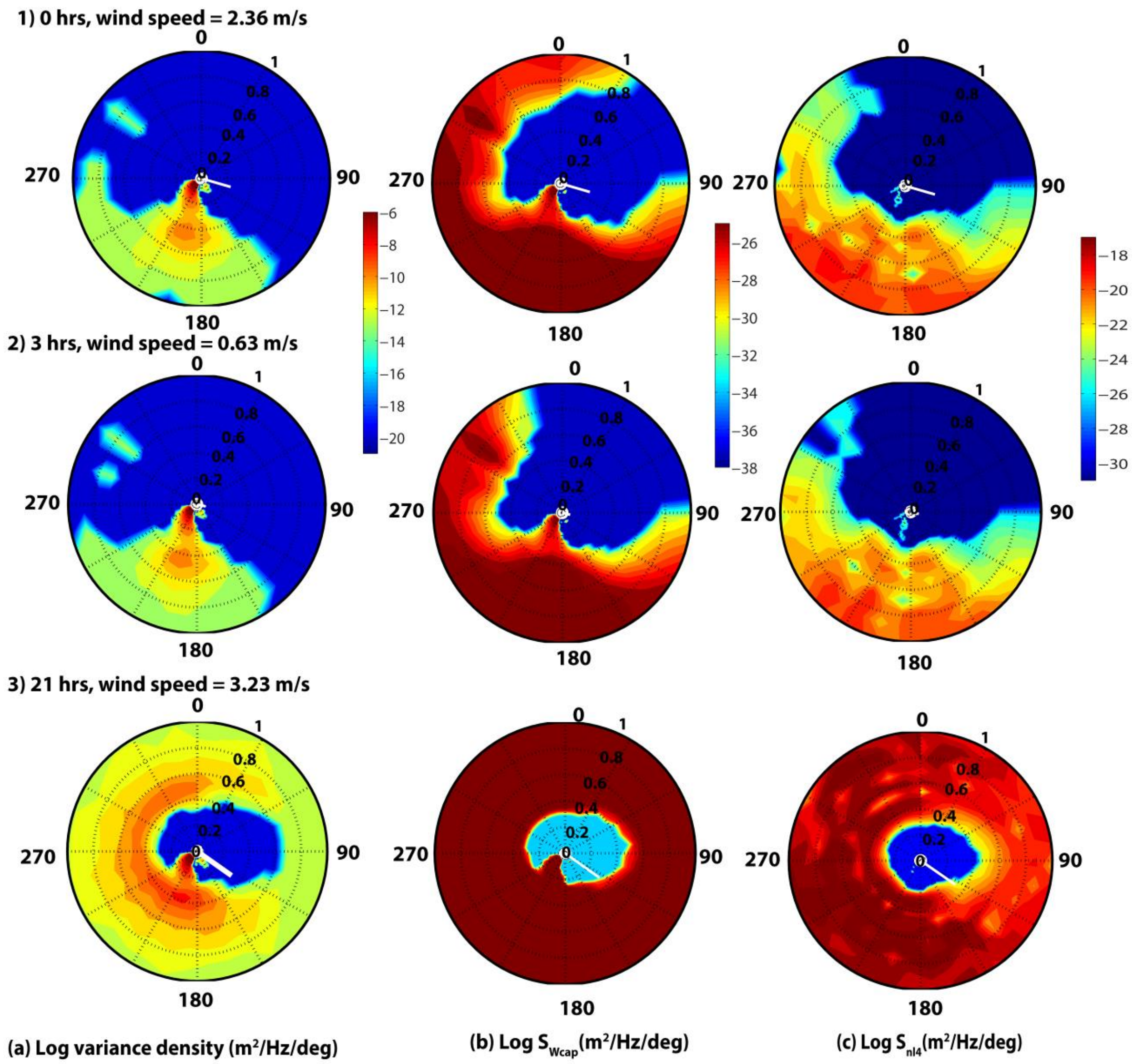

Figure 4.6 Source terms at 0 hrs, 3 hrs and 21 hrs on 27 March 2015. (a) log variance density, (b) dissipation due to white-capping (c) non-linear interactions

.

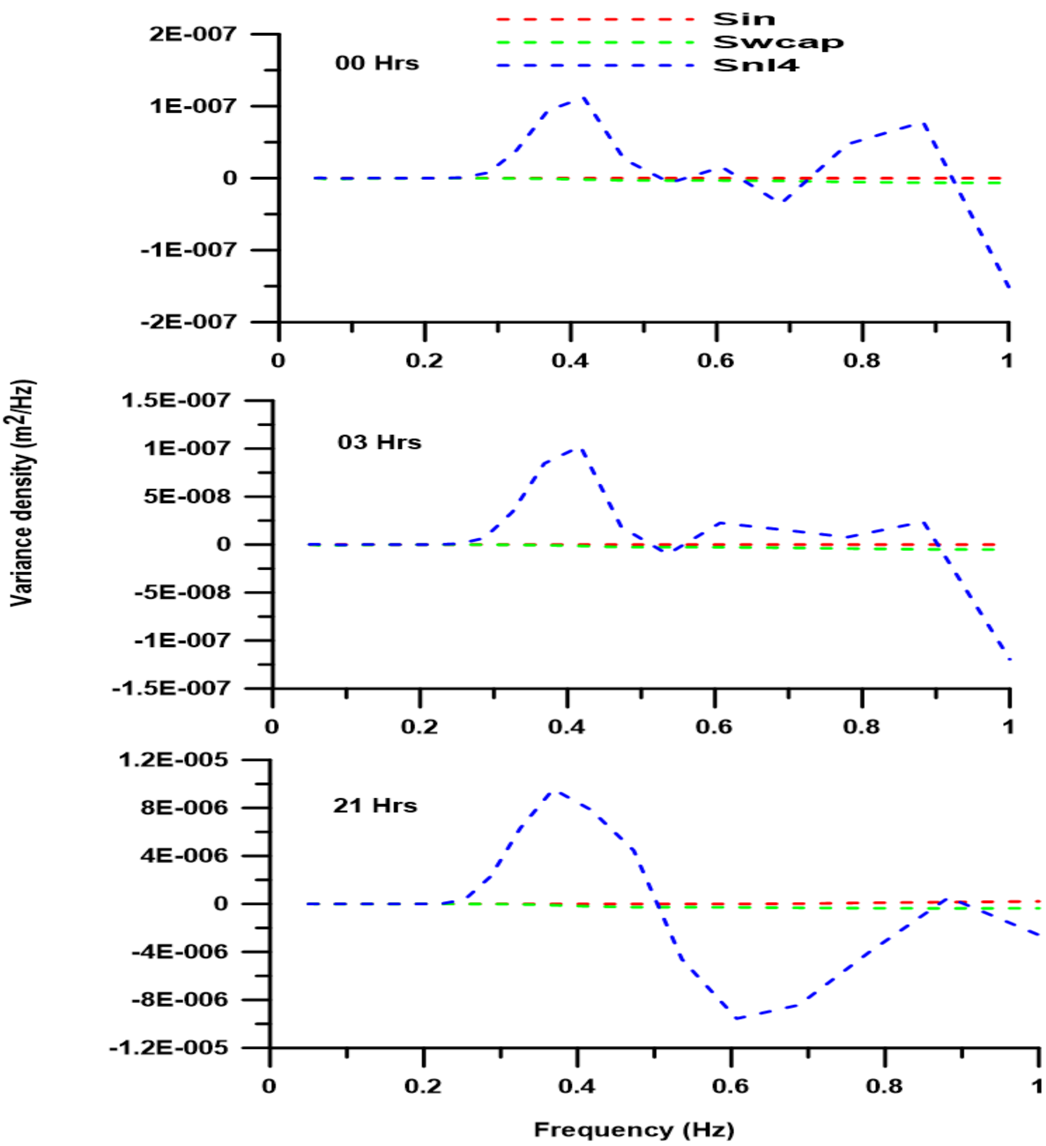

Figure 4.7 One dimensional spectra of source terms during land-breeze phase on 27 March 2015.

4.6 Spatial and Temporal variation in source terms

The spatial and temporal variations in source terms are studied by comparing the source terms at 9 m and 25 m water depth (Figure 4.8). The wind input term reaches its maximum at around 10-15 h. Non-linear interactions and dissipation due to white-capping come into action when the energy from wind input increases. The influence of dissipation due to white-capping is comparatively less at both the depths. The magnitude of source terms is high at 9 m depth compared to 25 m depth. Since sea breeze is a coastal phenomenon whose strength decreases offshore, the decrease in the magnitude of source terms at 25 m depth could be due to the decrease in the strength of sea breeze. Dissipation due to bottom friction and total energy dissipation is high at 9 m depth since the depth is less.

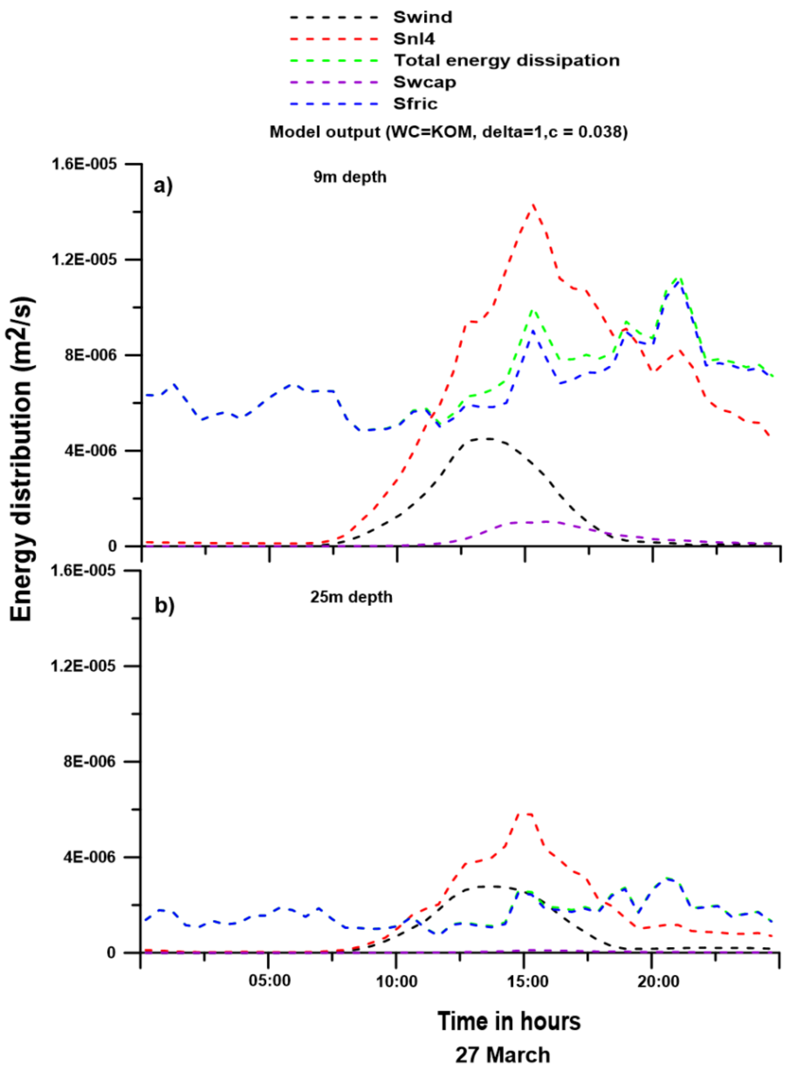

Figure 4.8 Variations in source terms over time a) at 9 m depth and b) at 25 m depth

4.7 Wave spectral partitioning during the sea-land breeze cycle

To get an insight about the wind-sea system generated due to sea breeze, the 2D measured wave spectra during a sea breeze cycle are partitioned using spectral partitioning algorithm. Figure 4.9 shows the wind-sea and major swell system present on 27 March 2015 from 6:30 hrs to 21:30 hrs; where partition no. 1 represents wind-sea and partition no.2 represents the major swell system. The peak of the major swell system with frequency around 0.1 Hz and having high energy is always from southwest direction (180^o -270^o) and the peak of the wind-sea system is always from the northwest (270^o – 360^o). But the intensity and the peak frequency of the wind-sea system varies with respect to time. The energy of the wind-sea system is almost zero at 6:30 hrs (Figure 4.9a) and it starts to increase by 9:30 Hrs. Some small peaks can be observed in the high frequency region (above 0.4 Hz) of the wind-sea system at 9:30 Hrs and the energy of the wind-sea peak increases thereafter. The wind-sea peak at 12:30 hrs and 15:30 hrs lies in the frequency bin between 0.3 to 0.4 Hz, which is where exactly the energy from wind input is maximum. At 18:30 Hrs and 21:30 hrs, wind-sea with sufficient energy can be observed, with its peak at lower frequencies (between 0.2 Hz and 0.3 Hz). There is no wind input due to sea breeze during these hours and hence the wind-sea observed could be due to the non-linear energy transfer from higher to lower frequencies.

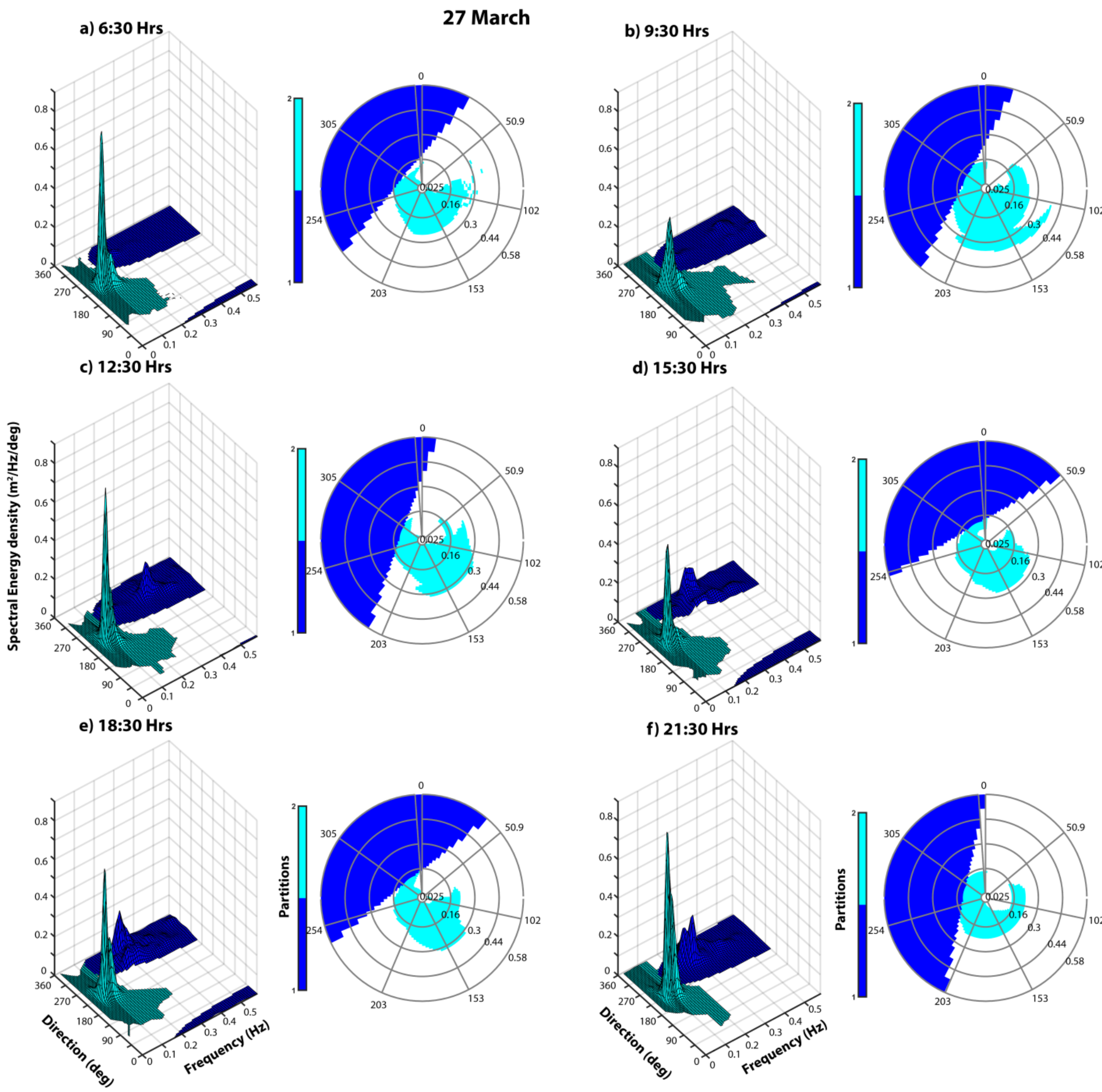

Figure 4.9 Wave spectral partitions (wind-sea and major swell) on 27 March 2015

Chapter 5: Growth and decay of wave spectra during tropical cyclones

5.1 Introduction

This chapter deals with the characteristics of wave spectra during the various stages of cyclone intensification both in the near-shore and deep waters. Here the characteristics of wave spectra off the east and west coasts of India are investigated during two cyclone events; PHAILIN and KYARR, respectively.

5.2 Cyclones PHAILIN & KYARR

The cyclone PHAILIN originated as a depression on 9 October 2013 morning over the southeast Bay of Bengal, which further intensified and developed into a cyclonic storm on the same day evening (IMD, 2013). Moving north-westwards, it further intensified into a severe cyclonic storm (SCS) in the morning and into a Very SCS in the forenoon of 10 October over the east-central Bay of Bengal. The PHAILIN crossed the Odisha coast near Gopalpur around 17:00 hrs on 12 October 2013.

The cyclone KYARR originated as a low-pressure area on 17 October 2019 and later evolved into a depression and a deep depression on 24 October 2019 in the Arabian Sea near Lakshadweep Islands. The deep depression, which initially moved to the northeast, towards the west coast of India, became a Cyclone Storm named KYARR on 25 October and further into a Severe Cyclonic Storm on the same day. On 26 October, KYARR turned to the northwest, away from the Indian coast, and further intensified into a Super Cyclonic Storm on 27 October with a maximum sustained wind speed of 240km/h (IMD 2019). KYARR passed off the Karnataka coast near Karwar around 06:00 hrs on 25 October 2019.

The track of the two cyclones and the wave rider buoy locations are shown in Figure 5.1. The wave rider buoy at Gopalpur drifted from its deployed location on 12 October 2013 at 00:00 hrs due to the impact of the TC, and the buoy remained within 100 km from the TC track on 12 October. The wave rider buoy data collected from 4 to 14 October 2013 (off east coast) and 22 to 27 October 2019 (off west coast) and the ECMWF - ERA5 reanalysis data are used in the study. In the Figure, Buoy X and Buoy Y represent the wave rider buoys off west (Karwar) and east (Gopalpur) coasts, respectively.

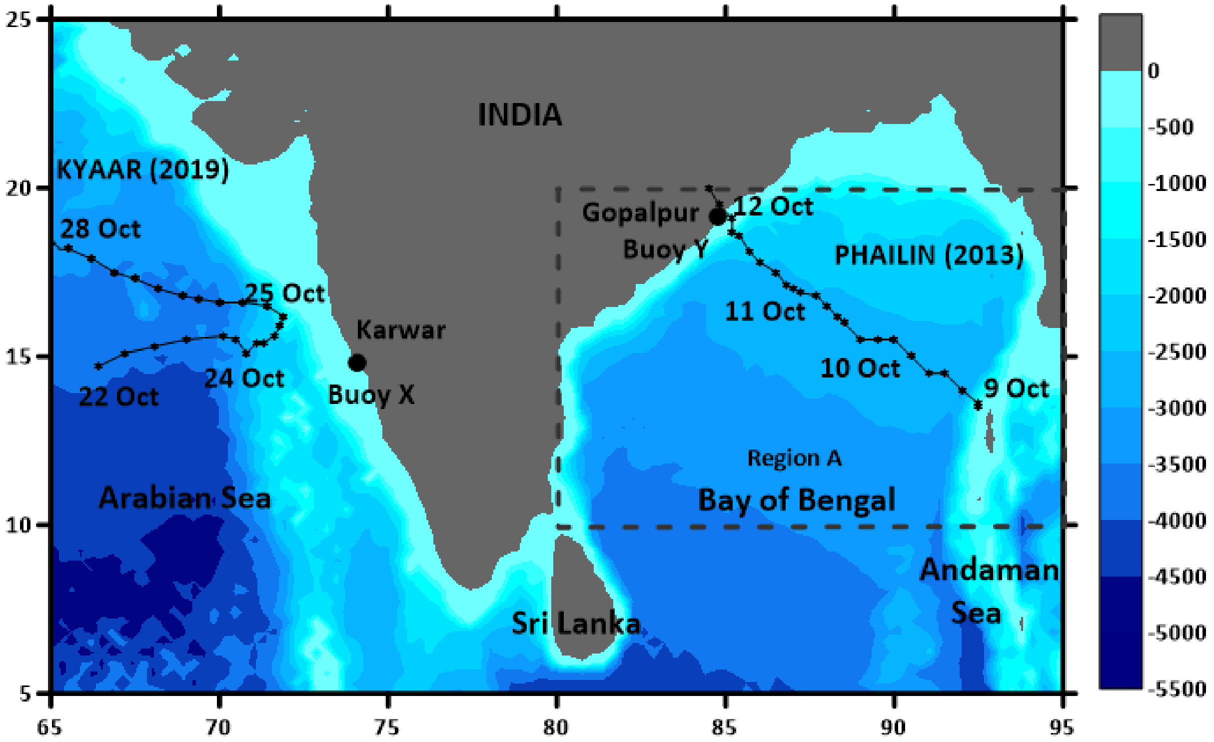

Figure 5.1 Study area showing the track of the cyclone KYARR and PHAILIN along with the wave rider buoy locations

5.3 Growth and decay of wave spectrum during cyclone PHAILIN

5.3.1 Near-shore region

The variation in the averaged wave parameters from wave rider buoy data (Buoy Y) during the TC is shown in the Figures 5.2 a to d. The H_{m0} before the arrival of the cyclone is between 1 and 2 m. In contrast, on 10 October 2013, when the cyclone is 850 km away from the buoy location, H_{m0} starts to increase to reach its peak on 12 October, indicating the influence of the TC. The maximum value of H_{m0} is 7.34 m, which occurs on 12 October, 10:42 hrs. An increase in the T_{m02} is observed during the TC period showing the influence of swells generated by the cyclone, which reached the location before the arrival of the cyclone.

The daily average spectral energy density of buoy wave data from 4 to 14 October is shown in Figure 5.2e. It can be seen that the wave spectrum before the arrival of the cyclone is double-peaked, with low-frequency swells and high-frequency wind-sea, whereas, during the cyclone period, the wave spectrum is single-peaked with very high spectral energy. The wave spectrum on 10 October is narrow, and the spectral peak lies predominantly in the swell region, indicating the presence of high energy swells reaching from the cyclone location. On 12 October, the spectral energy density is maximum, and the low-frequency wind-sea and swells merge to form a high energy single-peaked spectrum.

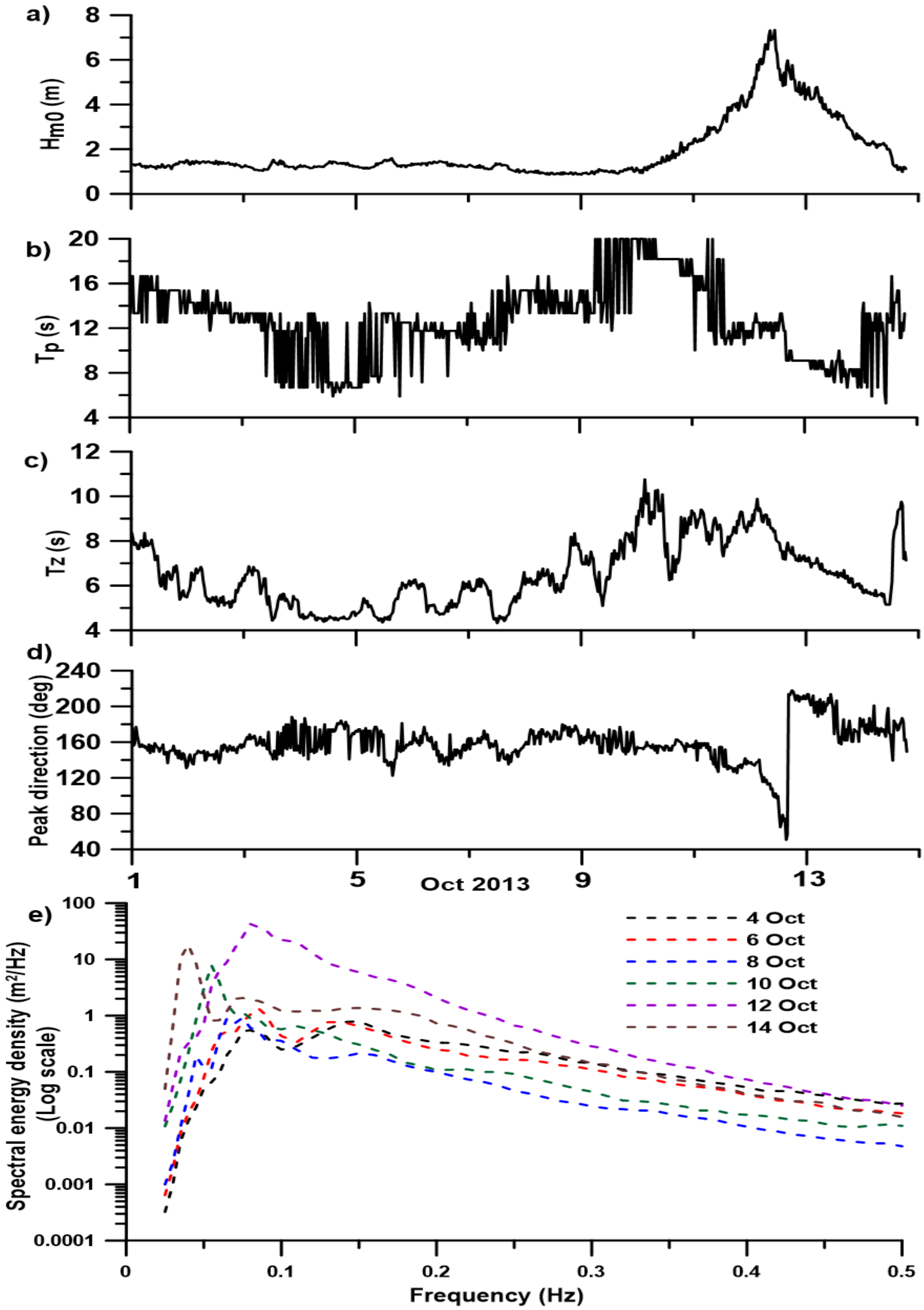

Figure 5.2 Time series plot of a) significant wave height, b) peak wave period, c) mean wave period, d) peak wave direction during 1 to 14 October 2013, and e) Daily average spectral energy density (4 to 14 October 2013)

The slope of the high-frequency part of the spectrum (between $2f_p$ and $4f_p$, f_p - peak frequency) estimated using the method of the best fitting curve for the daily averaged spectrum during the cyclone PHAILIN are shown in Figure 5.3. Here the values of the slope, are found to be increasing as the cyclone intensifies to reach its maximum (-4.74) on 12 Oct, when the cyclone reaches the buoy location. This shows that the wave spectrum becomes steep due to the influence of cyclone.

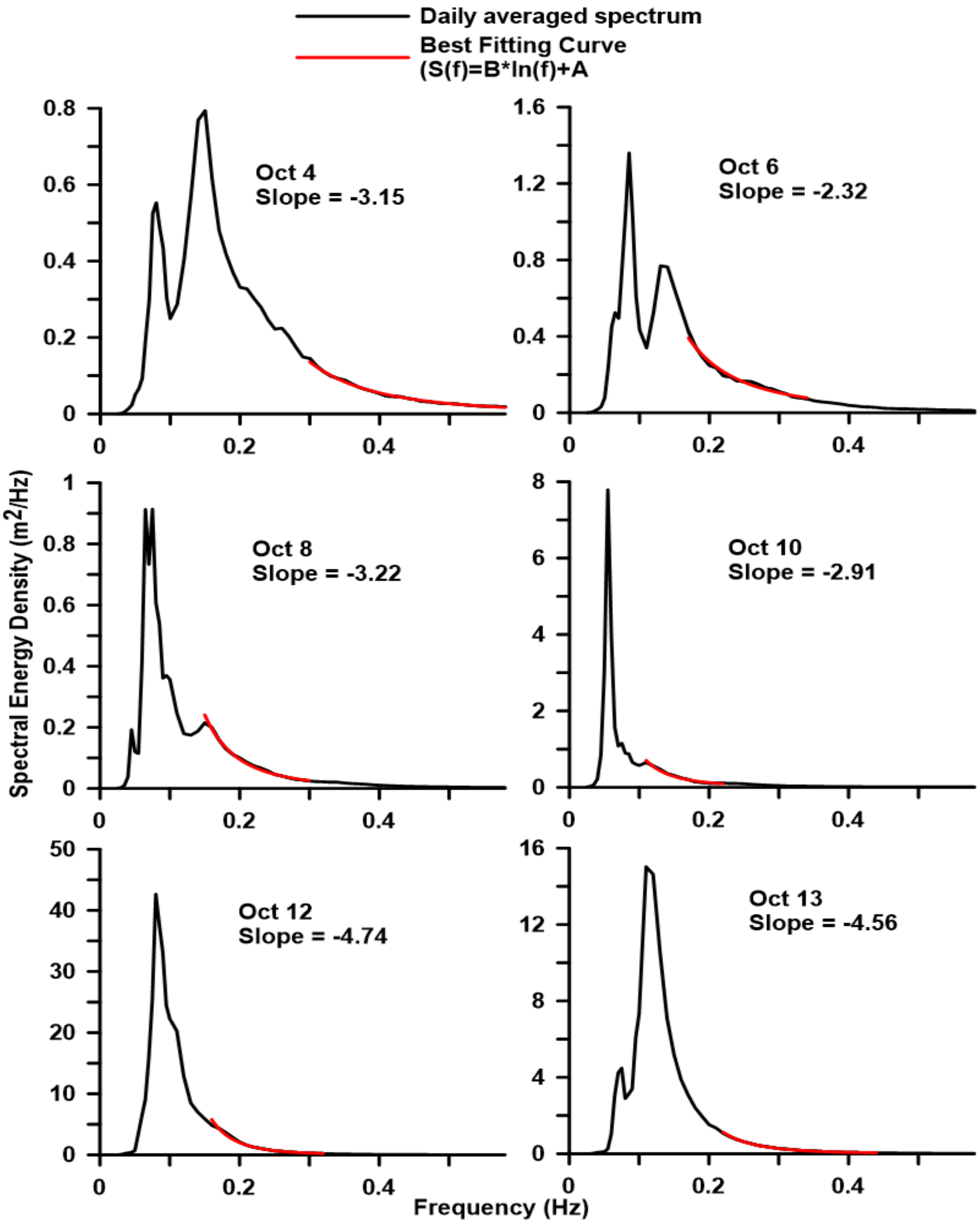

Figure 5.3 Slope of the high-frequency region of the spectrum during cyclone PHAILIN

Wave spectral partitions

The different wave systems generated during the tropical cyclone PHAILIN are obtained by spectral partitioning of the measured 2D spectra at Gopalpur (Figure 5.4). In the Figure, partition 0 represents noise, partition 1 represents the wind-sea system, and 2 represents the major swell system. The following numbers represent other wave systems. Before the arrival of the cyclone, on 8 October, swells from SE with peak frequency less than 0.1 Hz are observed at this location. These are the long-period swells from the South Indian Ocean, which exist at the location throughout the year. When cyclone originates on 10 October, the energy of the swell system increases, and the spectrum becomes narrow. On 11 October, when the intensity of the cyclone is maximum, one more wave system from SE with a peak frequency at around 0.1 Hz is observed at the study location. This wave system is the waves generated by the cyclone winds. Later, on the same day, this wave system can be seen interacting with pre-existing swells at the location. On 12 October, when the cyclone reaches the buoy location, the two wave systems merge to form a single-peaked swell system with high energy.

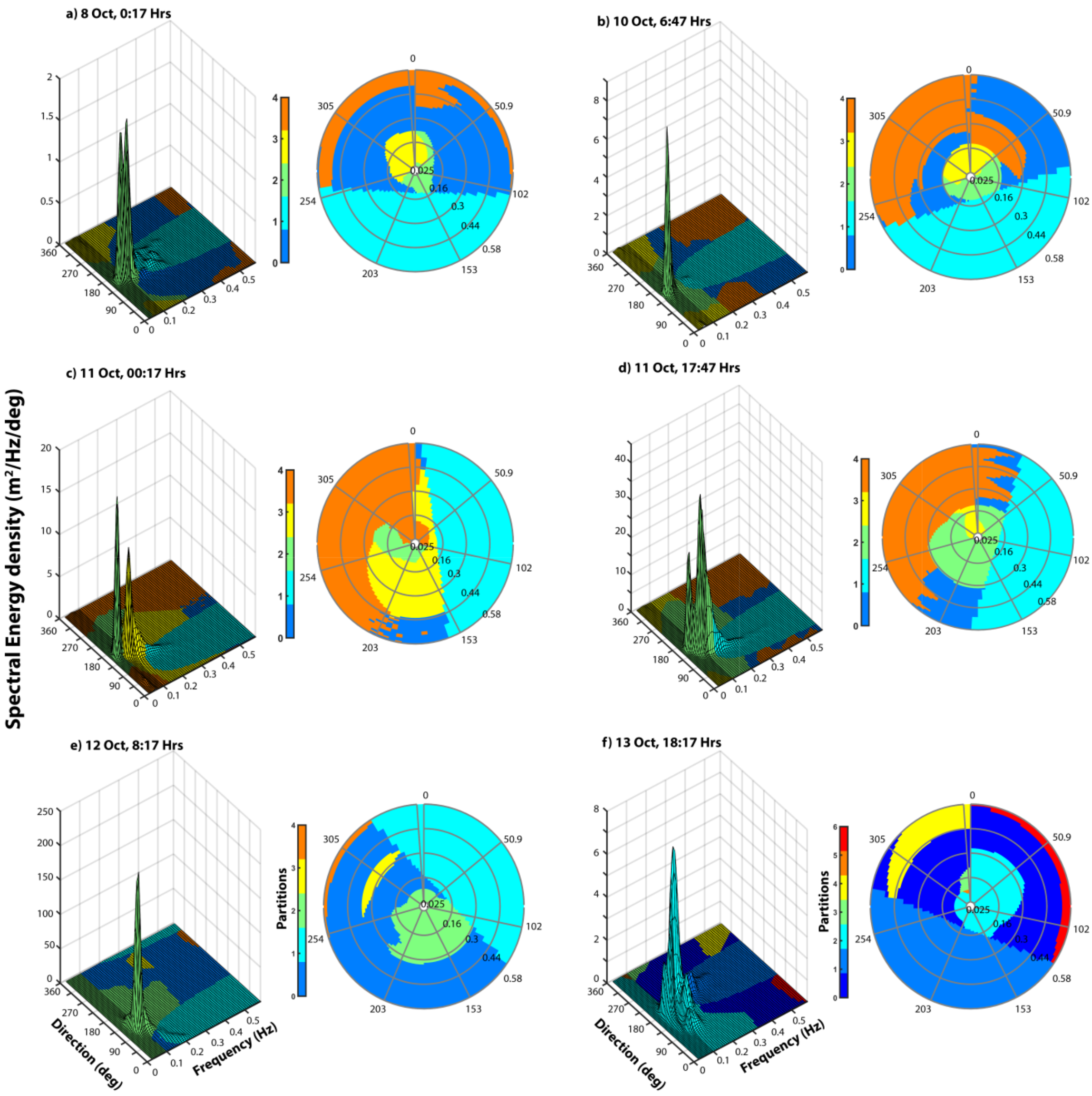

Figure 5.4 Wave spectral partitions during cyclone PHAILIN

5.3.2 Waves in deep waters

The influence of cyclone on waves in deep water can be observed as the changes in H_{m0} and T_p (peak wave period) during the cyclone period. To investigate the impact of the cyclone on wave parameters, the monthly averaged values of H_{m0}, T_p, and wind speed during October for a period of 40 years (1979 to 2018) are taken into consideration. During the 40 years span, there were cyclonic occurrences during the month of October in 20 years. Hence, these years were excluded, and the monthly averaged H_{m0}, T_p, and wind speed for October during the non-cyclonic years were calculated. ECMWF - ERA5 data at a location 88.5°E and 16.75°N (marked as N1 in Figure 5.6) is used in this study. The monthly averaged values in

October of H_{m0}, T_p, and wind speed during the non-cyclonic years are 1.4 m, 12.9 s, and 4.8 m/s, respectively. Whereas during cyclone PHAILIN, the monthly averaged values of H_{m0} and wind speed increases to 1.9m and 5.9m/s, and T_p decreases to 12.1s. The directional wave spectrum for the same location (N1) during 11 October 2015, when there are no cyclones in the Bay of Bengal, is shown in Figure 5.5. From the Figure, it can be seen that when there are no cyclones, the waves in the deep waters are dominated by SW swells, which are the long-period swells generated in the Southern Indian Ocean.

The growth and decay of the wave spectra and the variation in wave parameters during the cyclone in the deep waters are examined by considering the area at and around the cyclone location. The region 'A' mentioned in Figure 5.1 is considered in this study. Figure 5.6 shows the enlarged view of region 'A' along with the spatial distribution of H_{m0} and wind vectors on 11 October (00:00 hrs), when the cyclone reaches its maximum intensity. The Figure also shows the track of the cyclone, the cyclone eye location, and the adjacent locations in the north, west, east, and south of the cyclone eye, for which the characteristics of the wave spectrum are examined.

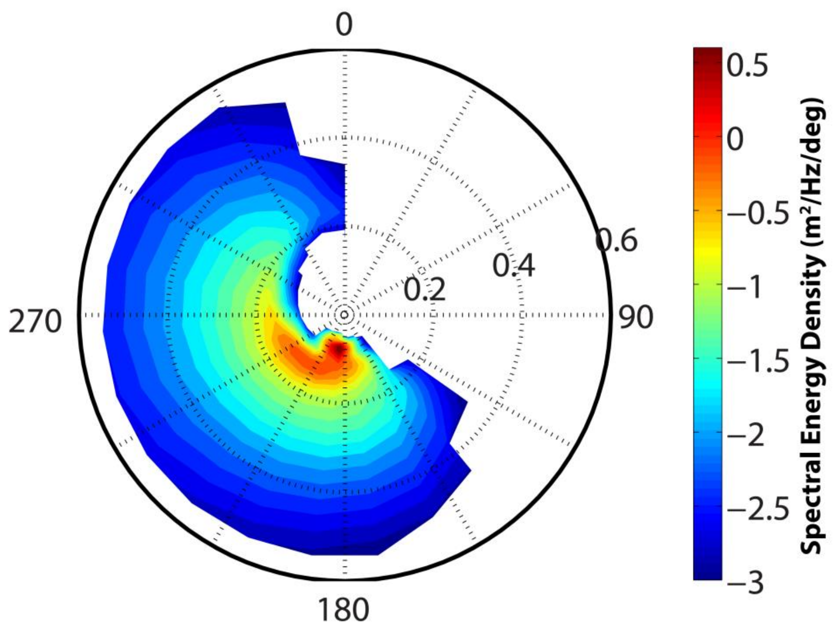

Figure 5.5 Directional wave spectra (ERA 5) at a location 88.5°E and 16.75°N (N1) on 11 October 2015 (00 h)

The wave directional spectra (ERA 5) at the cyclone eye (15.75°N, 88.5°E) and at locations north, west, south, and east of the cyclone (as marked in Figure 5.6) are shown in Figure. 5.7. The equivalent wind-sea frequency (f_u), which is the lowest wave frequency, which may receive energy input from the winds, is also shown. Two spectral peaks, one at a lower frequency (~0.056 Hz) and one at a higher frequency (0.1 – 0.15 Hz), can be identified in the Figure. The lower frequency peak, whose direction is always from the southwest, is a swell peak since the peak frequency is less than f_u. In contrast, the high-frequency peaks, of which the direction varies according to the wind direction, are the wind-sea generated by the cyclonic wind. The wind direction at the location of cyclone and north of cyclone is from the east, and hence the wind-sea peaks are also from the east. Right of the storm, centre, the wind direction approximately aligns with the direction of propagation of the storm, and hence it is expected that the wave propagates forward with the storm. These waves will remain within the intense wind regions of the storm for an extended period and are generally called "fetch-trapped waves" (King and Shemdin, 1978).

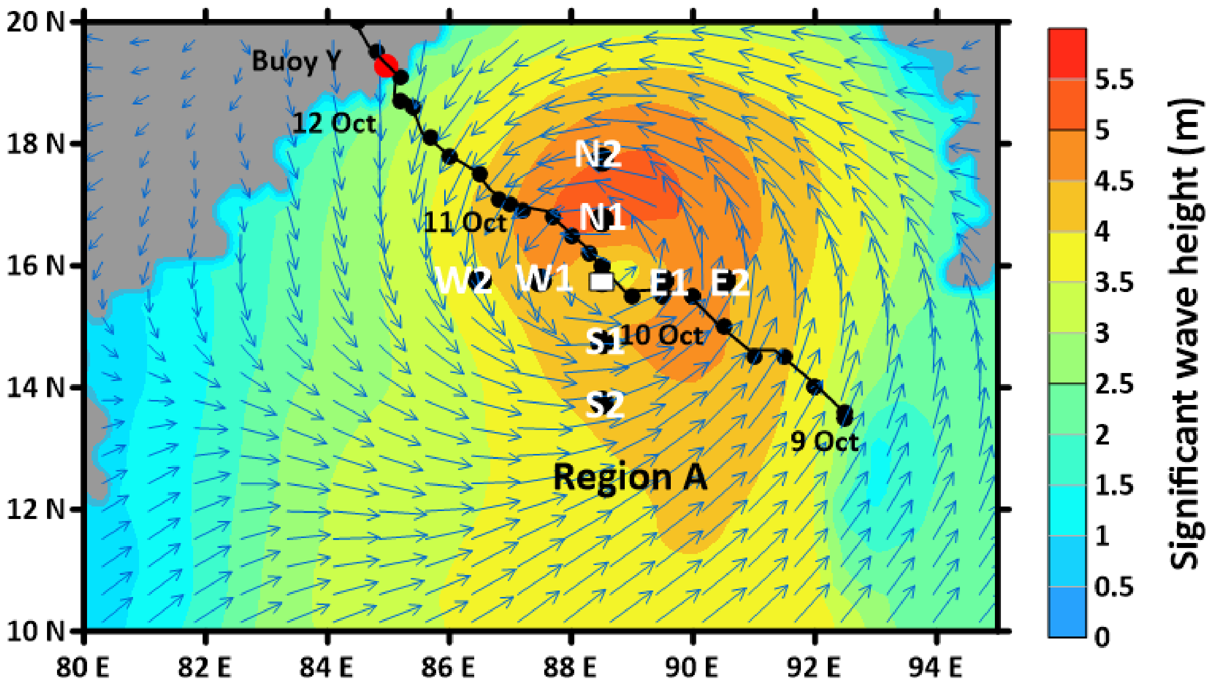

Figure 5.6 Region A showing the buoy Y, H_{m0}, (colour bar), wind vector (blue arrow), track of the cyclone (black line), cyclone eye (white patch), N1, N2, S1, S2, W1, W2, E1, and E2 are the locations around the cyclone eye considered for examining the spatial variation in wave spectra

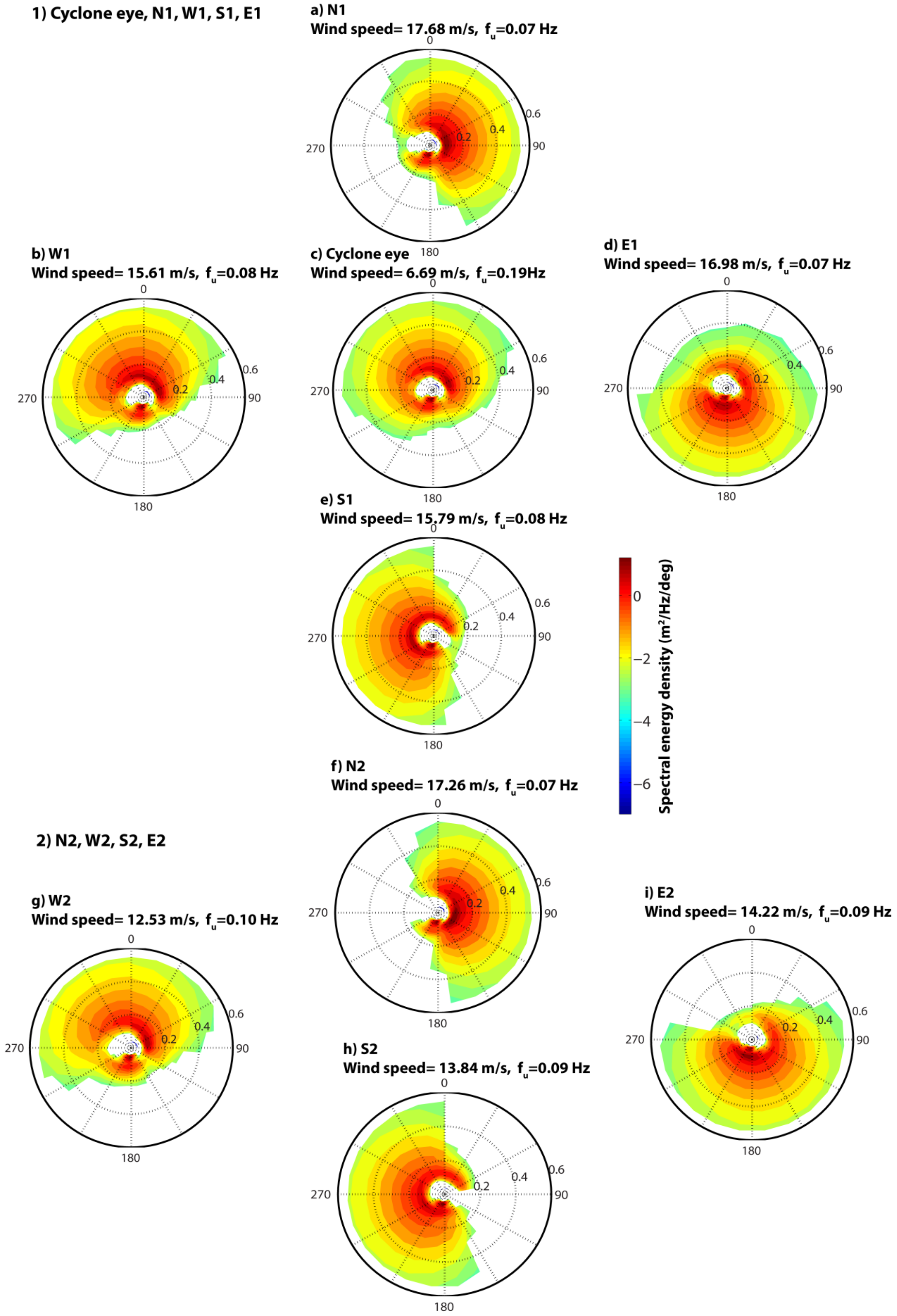

Figure 5.7 Directional wave spectra (ERA 5) at and around cyclone eye on 11 October 2013. Locations N1, N2, S1, S2, W1, W2, E1, and E2 are indicated in Figure 5.4.

Whereas in the left of the storm centre (Figures 5.7 b & g), the wind direction and the direction of propagation of the storm are opposed, and hence waves will remain in the strong wind field for a very short time. This causes asymmetry in the wave direction. It can be observed that in the west of the storm centre, the wind-sea direction is from the northeast. South of the storm centre wind speed is less, hence the wind-sea energy is also less, and it spread in all the directions according to the wind direction.

The growth and decay of wave spectra over time is shown in Figure. 5.8 as directional wave spectra from 6 to 18 October. From the Figure, it can be seen that there is a spectral peak with maximum energy, which always lies at a frequency less than 0.1 Hz, with its direction from southwest representing the swells. Another peak with comparatively lower energy is also observed in the same direction at around 0.1 Hz. But on 12 October, when the cyclone is very near, the energy of the second peak is very high. During all other time except 12 October, the U_{10}/C_p (U_{10} = wind speed, C_p = phase speed) ratio of the second spectral peak is less than 1, indicating that these waves are propagating faster than wind and hence cannot receive energy from wind. The spectral peak observed on 12 October holds $U_{10}/C_p > 1$, showing that it is still under the influence of cyclone winds.

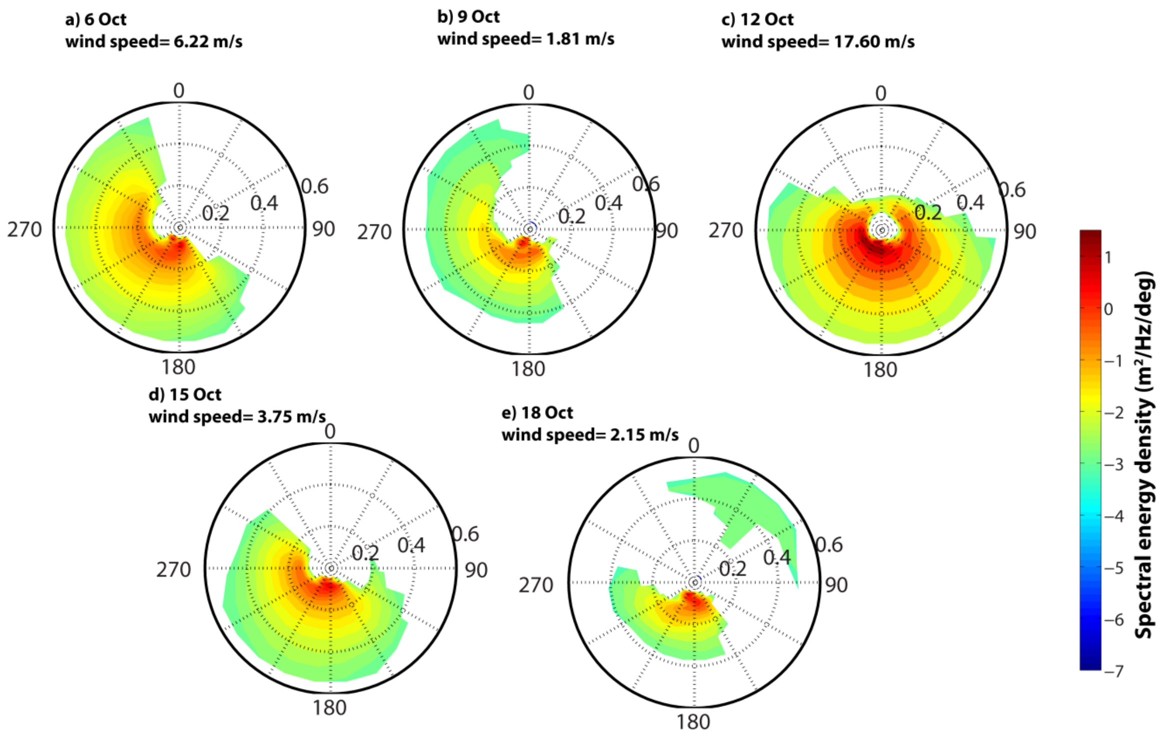

Figure 5.8 Directional wave spectrum (ERA 5) from 6 to 18 October at 16.5°N, 88.5°E

It is known that the wave pattern around a moving tropical cyclone follows an asymmetric pattern. To know more about this pattern, the H_{m0} distribution up to a radius of 220 km from the cyclone eye is analysed. The region is divided into four quadrants RF (right front), LB (left back), LF (left front), and RB (right back) with respect to cyclone heading direction following the definition of Hwang and Walsh (2016). In terms of azimuth angle referenced to the tropical cyclone heading ($\phi = 0$) and positive counter-clockwise, the range of each quadrant is defined as − 45 to 45 (RF), 45 to 135 (LB), 135 to 225 (LF), and 225 to 315 (RB) as shown in Figure 5.9a. Figure 5.9b shows that H_{m0} is asymmetric, with high values in the right quadrant (RF and RB) and low values in the left (LF and LB). To quantitatively analyse the asymmetry in the distribution of H_{m0}, the probability of occurrence of H_{m0} in each quadrant is calculated and shown in Figure 5.9d. H_{m0} observed in this region ranges from 3 to 6 m. Hence, the probability of occurrence of H_{m0} within the range 3–4 m, 4–5 m, and 5–6 m in each quadrant is shown in the Figure. In all the quadrants, the probability of occurrence of waves with the H_{m0} range 4–5 m is the highest. Waves with a high H_{m0} range (5–6 m) are occurring only in the RF and RB quadrant, whereas small waves (3–4 m) are mostly occurring in the LF quadrant. The occurrence of high waves in the right quadrant is due to the high wind speed in that region (Figure. 5.9b). To know more about the waves generated by the moving tropical cyclone, inverse wave age ($\omega_n = U_{10}/C_p$) is estimated for the region (Figure 5.9c). Except in the region near the cyclone eye, the waves in the TC are active wind-sea with ω_n greater than 1. Though inverse wave age (ω_n) is directly proportional to wind speed and wind speed is high in the right quadrants, the youngest wind-sea (high ω_n values) are found in the LF and LB quadrants, whereas, in the RF quadrant, the wind-sea are comparatively older. This is because C_p is directly proportional to H_{m0}, as explained by Zhang and Oey (2019), and H_{m0} is low at LF and LB quadrants resulting in high ω_n. In the RF quadrant slightly older waves with large H_{m0} are found.

The relation between the velocity of forward motion of the cyclone and the distribution of significant wave height is also investigated. Figure 5.10 shows the variation of H_{m0} for different velocities of forward motion of cyclone. Figures 5.10 a and b show the distribution of wind speed and H_{m0} on 10 October, at 12 hrs and 18 hrs, respectively. Even though the maximum value of wind speed (V_{max}) observed here is almost the same, the velocity of forward motion (V_{fm}) of the cyclone differs. Similarly, Figures 5.10 c and d show the wind speed and H_{m0} on 11 October at 00 hrs and 18 hrs, where the values of V_{fm} are 7.20 m/s and 2.27 m/s, respectively. Here it can be seen that the wave-field does not follow exactly the same distribution as the wind field. For higher values of V_{fm} (Figures 5.10 a and c), the contours of H_{m0} tend to sweep back behind the storm centre. This is because when the propagation velocity of the cyclone increases, it exceeds the group velocity of the waves generated by the storm, and these waves cannot keep pace with the storm, whereas for lower values of V_{fm}, larger waves are seen on the right quadrant of the cyclone eye.

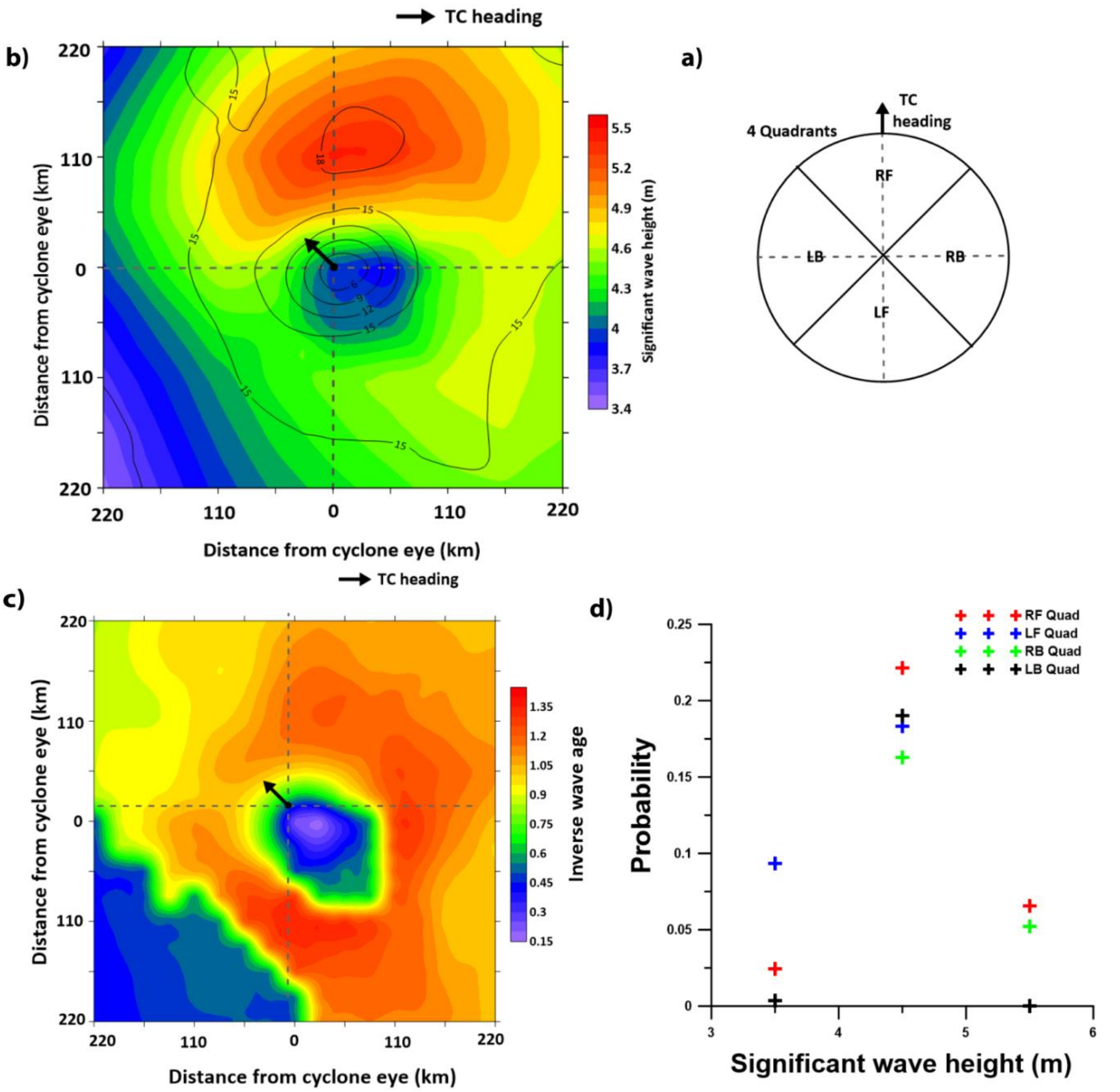

Figure 5.9 The distribution of wave parameters from the cyclone eye on 11 October 00 hrs a) four quadrants discussed in this chapter b) Distribution of significant wave height in each quadrant along with tropical cyclone heading direction and wind speed contour (black contour) c) Inverse wave age in each quadrant d) Occurrence probability of Significant wave height range in each quadrant.

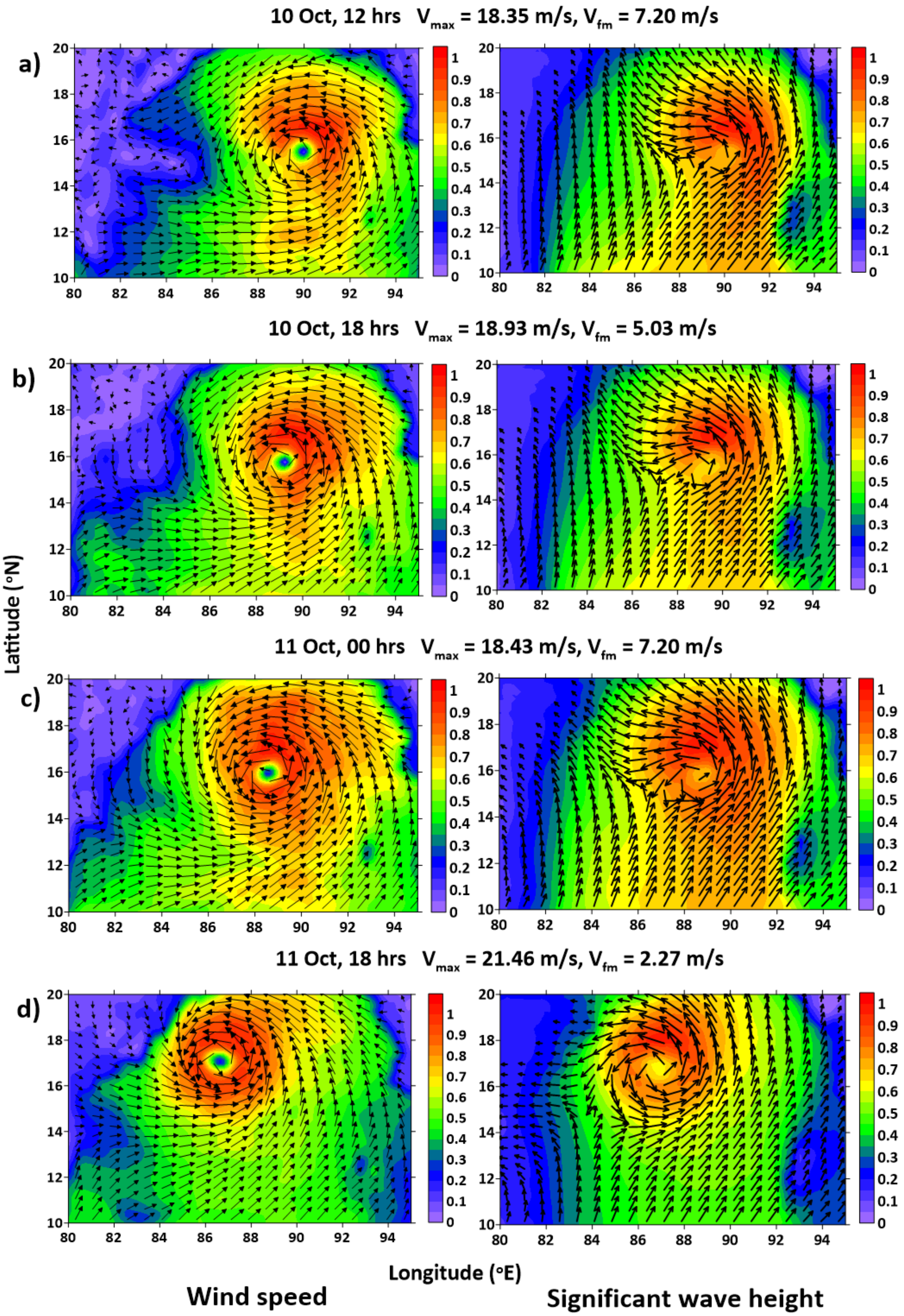

Figure 5.10 The left panel shows the wind speed contours and wind vectors. The right panel is the H_{m0} contours and mean wave direction vectors for different velocities of forward motion of cyclone. Normalised values of wind speed and H_{m0} from ERA5 are presented.

5.4 Growth and decay of wave spectrum during cyclone KYARR

5.4.1 Near-shore region

The different wave systems generated during the tropical cyclone KYARR, obtained by spectral partitioning of the measured 2D spectra at Karwar, are shown in Figure 5.11. Before the arrival of the cyclone, on 23 October, two wave systems can be observed at the location (Figure 5.11a); wind-sea and a major swell system, both from the SW direction (180^o – 270^o). The long-period swells are the swells originating from the southern Indian Ocean, which is present throughout the year. The peak frequency of the swell system is at around 0.15 Hz, whereas the wind-sea peak system lies between 0.2 Hz to 0.3 Hz. On 24 October, when the cyclone originates, only one wave system can be observed. This wave system which is from the same direction as the pre-existing swell (SW) but with high energy, indicates that the wave system originated from the cyclone interacted with the pre-existing swells in that location to form a single-peaked spectrum. As the cyclone intensifies and it moves closer to the study area, the swell energy further increases to reach its peak on 25 October at 07:00 Hrs (Figure 5.11c). Later, on 25 October (Figure 5.11d), as the cyclone starts to move away from the study area, the swell energy decreases, and the study area is dominated by both swells and wind-sea. On 26 and 27 Oct, when the cyclone moves further westward from the study area, though the energy of the wave systems decreases, many wave systems can be observed at the location. On 27 October (Figure 5.11f), the study area has a mixed sea-state with three distinct wave systems: one swell system, one wind-sea system and another wave system with frequencies ranging between 0.1 and 0.2 Hz from NW. Here, one swell system with a peak frequency less than 0.1 Hz from the SW direction is the already existing swell system, whereas the second wave system with a frequency between 0.1 and 0.2 Hz from the NW direction is the wave system generated by the cyclone.

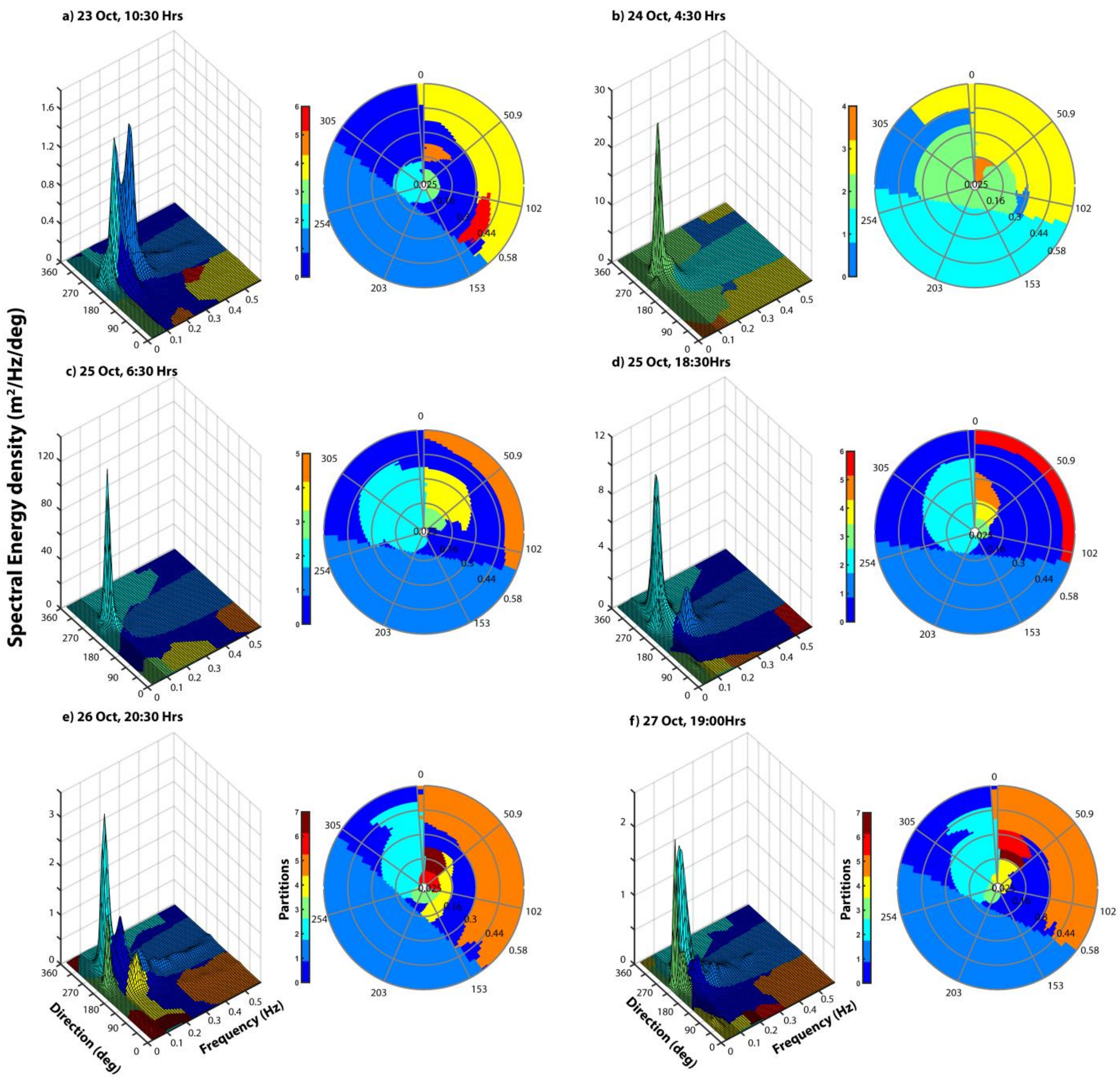

Figure 5.11 Wave spectral partitions during cyclone KYARR

The slope of the high-frequency part of the spectrum during the cyclone KYARR estimated using the method of the best fitting curve for the region of the spectrum between $2f_p$ and $4f_p$, where f_p is the peak frequency of the spectrum, are shown in Figure 5.12. Here the slope becomes steep (-4) when the cyclone intensifies and moves closer to the study location. This shows that the wave spectrum becomes steep due to the influence of cyclone. Similar to the wave spectra during the cyclone PHAILIN, here also the value of the slope increases as the cyclone intensifies to reach its maximum on 25 Oct (-4.01), when the cyclone is close to the buoy location. The slope of the wave spectrum during the maximum cyclone intensity is in the range of -4, during both the cyclones.

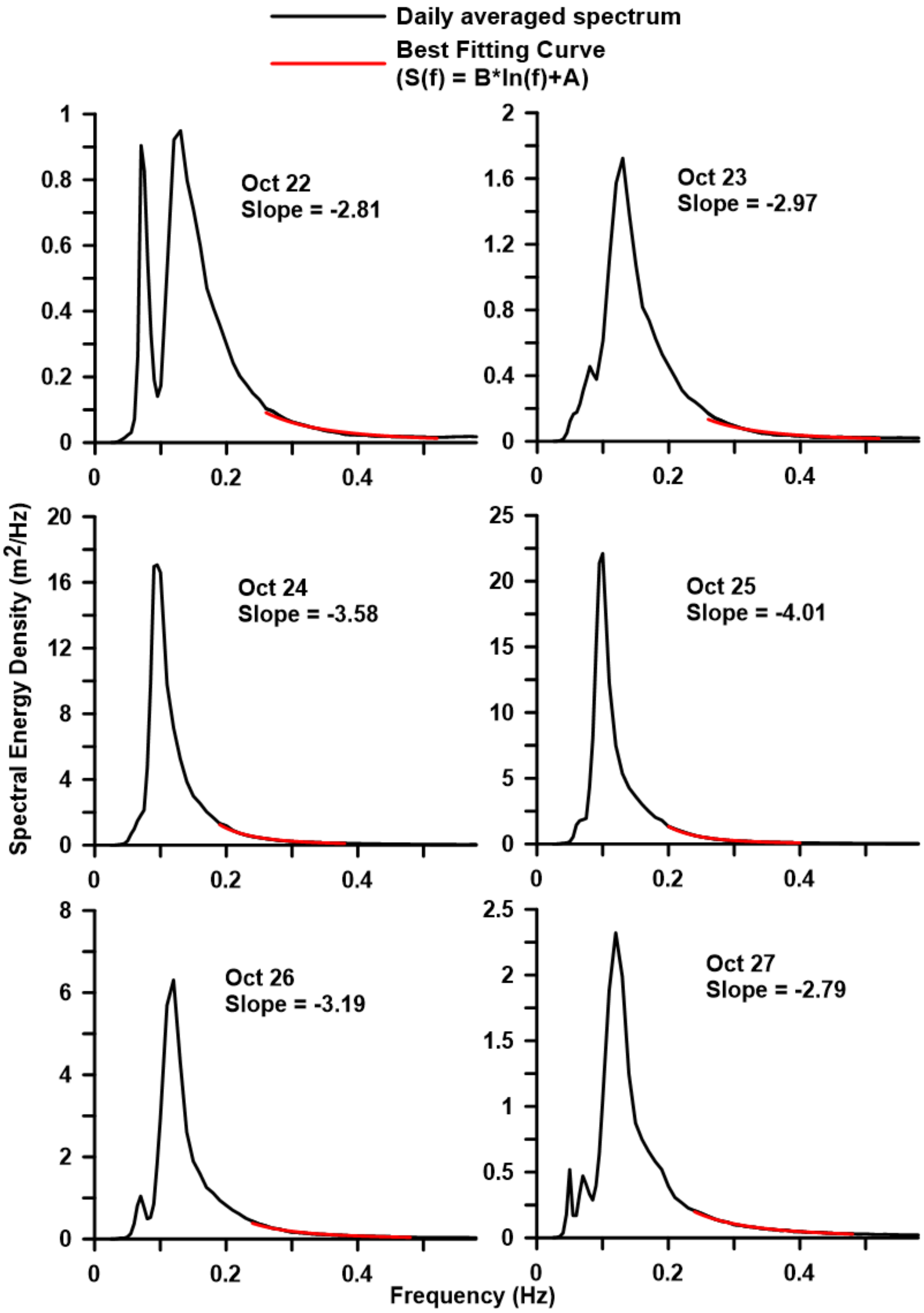

Figure 5.12 Slope (exponent) of the high-frequency region of spectra during cyclone KYARR

5.4.2 Waves in deep waters

The directional wave spectrum for a location 15.5°N and 72.5°E on 11 October 2017, at 7:00 hrs, when there are no cyclones in the Arabian Sea, is shown in Figure 5.13. From the Figure, it can be seen that when there are no cyclones, the waves in the Arabian Sea deep-waters during October are dominated by two swell systems from SSW and SSE and a wind-sea system from NW. The two swell systems with peak frequencies less than 0.1 Hz are the long-period swells generated in the South Indian Ocean.

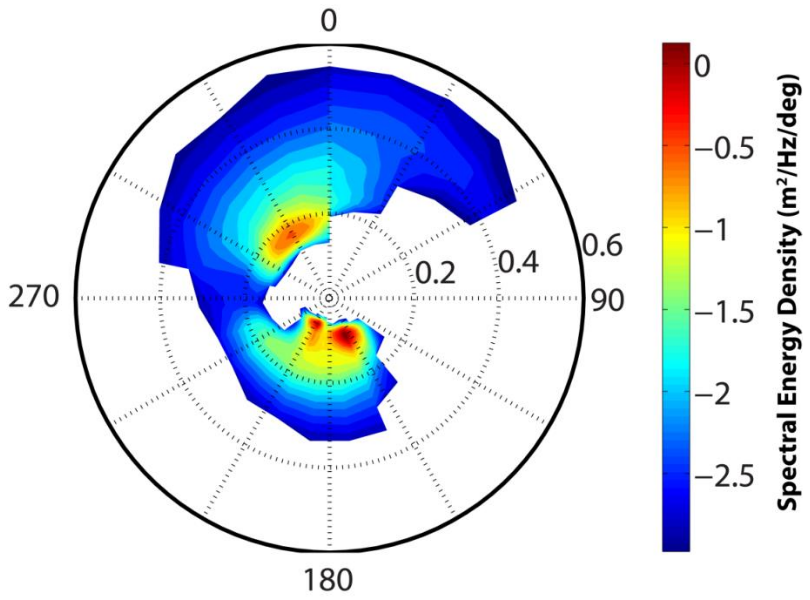

Figure 5.13 Directional wave spectra (ERA5) at a location 72.5°E and 15.5°N on 25 October 2017 (07 hrs)

To have an insight about the wave patterns during the cyclone, the directional wave spectra from ECMWF – ERA5 reanalysis data for the buoy location and its nearby locations are shown in Figure 5.14 The data presented here is for 25 October 07:00 hrs, when the spectral energy density of the measured spectrum is at its peak due to cyclone. Figure 5.14c shows the directional spectra at the buoy location of Karwar and Figure 5.14 a & b, are for the locations west (offshore) of the buoy location. In the figures it can be seen that, at all the three locations, the peak frequency (f_p) of the wave spectrum is slightly greater than the equivalent wind-sea frequency showing that, these waves are the wind-sea generated by the cyclone winds. The study area, which is dominated by swells (SSW & SSE) and NW wind-sea (Figure 5.13), changes to a high energy single-peaked wave spectrum with wind-sea from the WSW direction (Figure 5.14). During this time, the eye of the cyclone is northwest of the buoy location. It can be seen that the wave pattern does not undergo much change as the waves propagate from the cyclone region towards the coast.

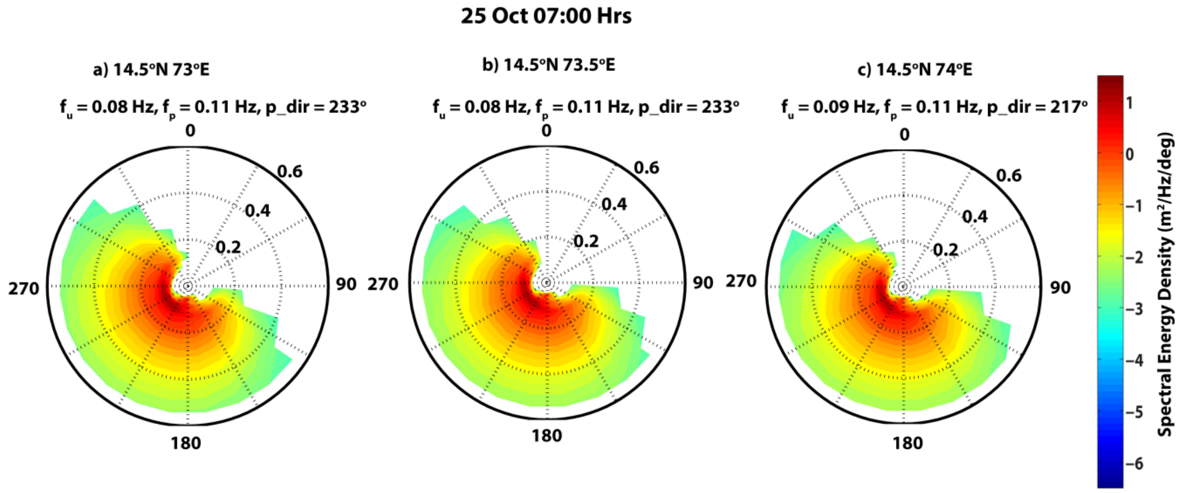

Figure 5.14 Directional wave spectra (ERA5) at the buoy location (c) and two locations offshore of the buoy location (a & b) on 25 October 2019 (07 hrs)

The wave pattern at the cyclone location, north & south of it, during the growth and intensifying phase of the cyclone, is shown in Figure 5.15. Here the middle panel shows the directional spectra (ERA5) for the cyclone location when it is closest to the coast, whereas the top and bottom panel represent the northern and southern locations, respectively. Here except for the northern location on 24 Oct 0 hrs (Figure 5.15a), at all other location the waves generated due to cyclones are wind-seas ($f_p > f_u$). As the cyclone intensifies, the peak energy increases, and the energy peak, which is from the SW direction, spreads to NW in the southern location and NE in the northern location.

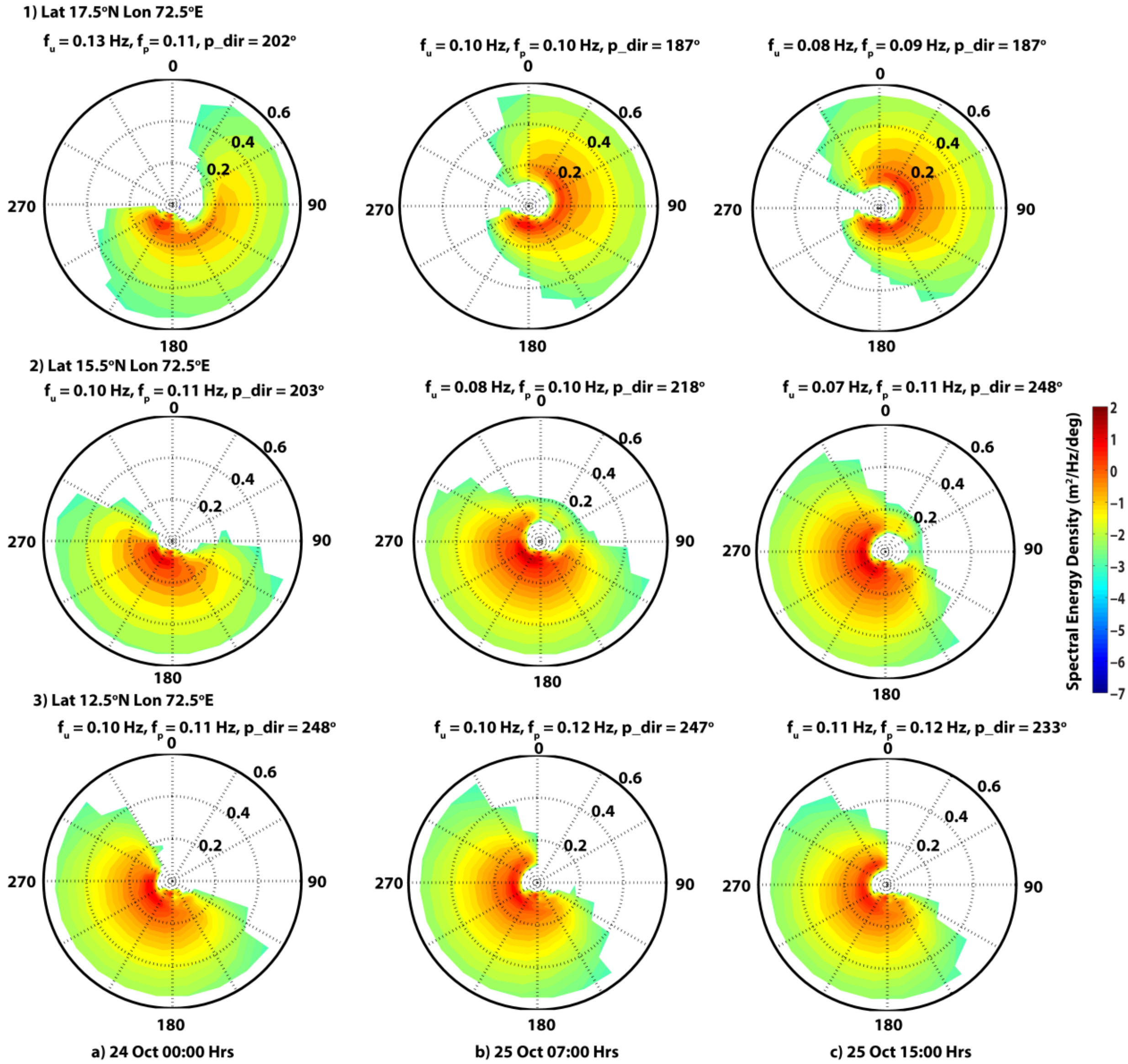

Figure 5.15 Directional wave spectra (ERA5) at different stages of cyclone intensification. The middle panel represents the cyclone location & the top and bottom panel represents locations north and south of the cyclone.

Chapter 6: Fitting theoretical wave spectrum for different wave conditions

6.1 Introduction

This chapter deals with fitting the theoretical wave spectrum to the measured wave spectrum for different wave conditions and estimation of spectral parameters. Here the theoretical wave spectral fitting is done to the monthly averaged spectra of all the five locations, to the measured wave spectrum during cyclones, and to the measured wave spectra at different water depths.

6.2 Fitting different theoretical wave spectra to the measured wave spectrum

Figure 6.1 shows the fitting of various theoretical wave spectra mentioned in the literature to the monthly averaged measured spectrum during June from 2010 to 2015 at the location Karwar. It was found that among the theoretical wave spectra, JONSWAP and Donelan spectra describes the wave conditions at the study location, and hence those two are used for spectral fitting. In the case of the single-peaked spectrum, the JONSWAP spectrum is used to fit the region below peak frequency and the Donelan spectrum at the region above peak frequency. In the case of the double-peaked spectrum, the first peak is fitted using the JONSWAP spectrum and the second peak using the Donelan spectrum. Here the values for α and ϒ were varied from 2×10^{-6} to 0.1 and 1.1 to 3.3, respectively, to find the values for which the theoretical spectrum best fits the measured spectrum. JONSWAP spectrum was proposed for the fetch-limited growing waves for which the shape is defined by five parameters. The peak frequency 'f_p' and the Phillips constant 'α' (Phillips, 1958) are called the scale parameters, where α is determined by total wave energy. The other three parameters ϒ, σ_a, and σ_b define the shape of the spectrum. The peak enhancement parameter ϒ is the ratio of the maximum spectral energy to the maximum of the corresponding Pierson-Moskowitz (Pierson-Moskowitz, 1964) spectrum given α is the same. The magnitude of the peak wave energy is determined by ϒ. Thus, both α and ϒ may be connected with H_{m0}, T_p, and hence on wind speed. According to Young (2003), σ_a and σ_b, which define the left and right-side widths respectively of the spectral peak region, have a weak influence on the general wave spectral shape. The generally recommended value of α is 0.0081. Hasselmann et al. (1973) couldn't find a trend for the value of ϒ and is expected to vary from 1 to 10 with a value of 3.3 commonly chosen. Previous studies have described α and ϒ using some equations connecting non-dimensional fetch, wind speed, H_{m0}, T_p, C_p, and T_{m02} for different sea areas

(Hasselmann et al., 1973; Ochi and Hubble, 1976; Donelan et al., 1985; Ochi, 1993; Young and Verhagen, 1996; Young, 1998; Chakrabarti, 2005; Kumar et al., 2008; Feng et al., 2012). Liu et al. (2017), in the study conducted in the South China Sea, found out that except the equation provided by Kumar et al. (2008), all the equations provided by the above-mentioned studies gives a reasonable estimate of α from the non-dimensional peak period during the typhoon conditions.

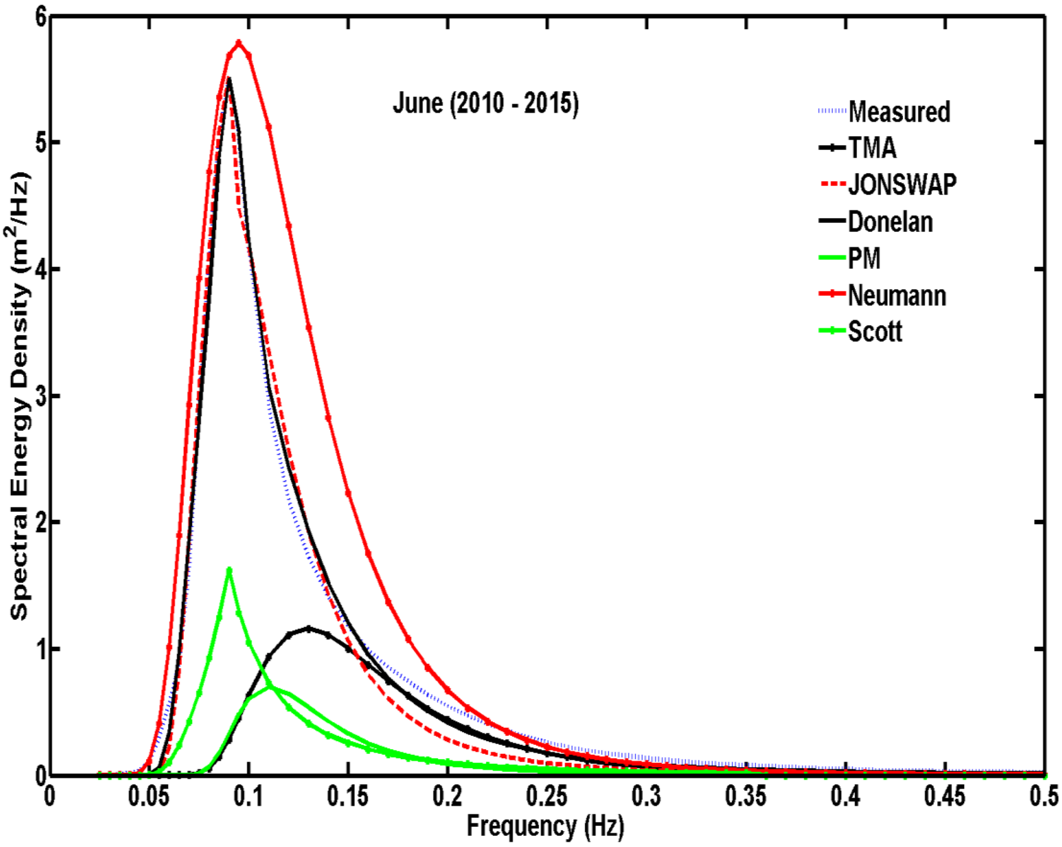

Figure 6.1 Different theoretical wave spectrum fitted to the monthly averaged measured spectrum during June from 2010 to 2015 at Karwar

6.3 Fitting theoretical wave spectra for monthly averaged spectrum

6.3.1 Ratnagiri

Theoretical wave spectrum fitted against the monthly averaged measured wave spectrum off Ratnagiri for the year 2015 shows that theoretical wave spectrum defines the measured wave spectrum well during all the months except May (Figure 6.2). JONSWAP spectrum fits well to the swell region of the spectrum, and discrepancies can be seen at the wind-sea part of the spectrum while fitting the Donelan spectrum. The spectral parameters estimated show that for JONSWAP spectrum α values vary in the range 1×10^{-5} to 6.2×10^{-4} and ϒ in the range 1.1 to 2.8, with both of its maxima during the month of July. The α values of the Donelan spectrum varies within the range 1.4×10^{-3} to 8.8×10^{-3} with its maximum in July and ϒ values between 1.3 and 2.2 with its maximum during May.

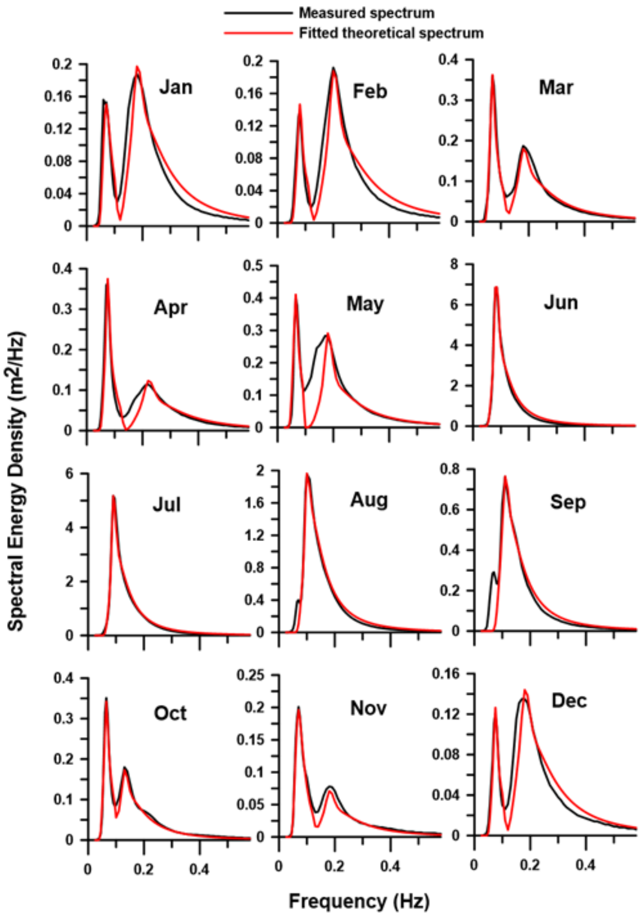

Months	JONSWAP		Donelan	
	α	ϒ	α	ϒ
Jan	1.3×10^{-5}	1.1	6.1×10^{-3}	1.5
Feb	1.7×10^{-5}	1.6	7.4×10^{-3}	1.8
Mar	2.3×10^{-5}	1.5	5.2×10^{-3}	1.6
Apr	2.8×10^{-5}	1.8	7.5×10^{-3}	1.7
May	1.7×10^{-5}	1.5	6.1×10^{-3}	2.2
Jun	4.9×10^{-4}	2.6	8.3×10^{-3}	1.9
Jul	6.2×10^{-4}	2.8	8.8×10^{-3}	1.7
Aug	5×10^{-4}	2.2	6.7×10^{-3}	1.3
Sep	4.3×10^{-4}	1.6	3.6×10^{-3}	1.4
Oct	1.5×10^{-5}	1.5	1.4×10^{-3}	1.6
Nov	1.7×10^{-5}	1.1	1.9×10^{-3}	1.7
Dec	1×10^{-5}	1.7	4.4×10^{-3}	1.5

Figure 6.2 Fitted theoretical wave spectrum to the monthly averaged measured spectrum during 2015 at Ratnagiri along with the estimated spectral parameters.

6.3.2 Karwar

Theoretical wave spectrum fitted against the monthly averaged measured wave spectrum off Karwar for the year 2014 shows that theoretical wave spectrum defines the measured wave spectrum well during all the months (Figure 6.3). Both JONSWAP and Donelan spectrum fits well to the swell and wind-sea region of the spectrum, respectively. The spectral parameters estimated show that for JONSWAP spectrum α values vary in the range 1.7×10^{-5} to 9.9×10^{-4} with its maximum values during June. The ϒ values for the JONSWAP spectrum vary between 1.1 and 2.3, with its maximum during the month of July. The α values of Donelan spectrum varies within the range 1.1×10^{-3} to 8.3×10^{-3} with its maximum in July and ϒ values between 1.1 and 2.5 with its maximum during May.

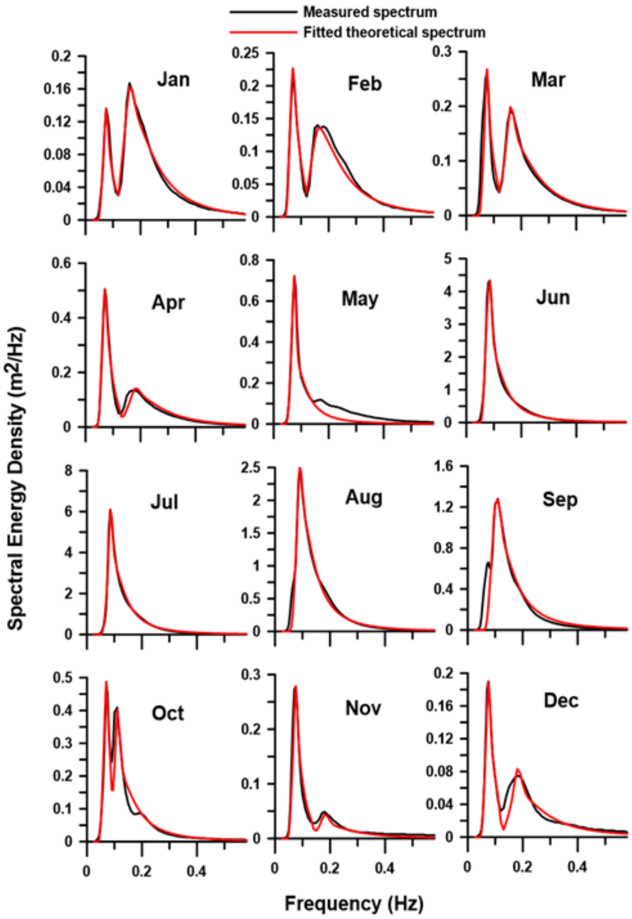

Months	JONSWAP		Donelan	
	α	ϒ	α	ϒ
Jan	6.3×10^{-5}	1.4	3.6×10^{-3}	1.3
Feb	1.8×10^{-5}	1.2	3.5×10^{-3}	1.1
Mar	2.4×10^{-5}	1.5	3.8×10^{-3}	1.5
Apr	3.7×10^{-5}	1.3	5×10^{-3}	1.3
May	6.5×10^{-5}	1.5	4×10^{-3}	2.5
Jun	9.9×10^{-4}	1.1	5×10^{-3}	2
Jul	6.6×10^{-4}	2.3	8.3×10^{-3}	1.7
Aug	5.6×10^{-4}	1.5	5.2×10^{-3}	1.4
Sep	4.6×10^{-4}	1.5	5.5×10^{-3}	1.5
Oct	3.1×10^{-5}	1.5	1.3×10^{-3}	2
Nov	2.5×10^{-5}	1.5	1.1×10^{-3}	1.9
Dec	1.7×10^{-5}	1.5	2.3×10^{-3}	1.7

Figure 6.3 Fitted theoretical wave spectrum to the monthly averaged measured spectrum during 2014 at Karwar along with the estimated spectral parameters.

6.3.3 Honnavar

For the location, Honnavar, the α values of the JONSWAP spectrum estimated varies from 1.4×10^{-5} to 9.8×10^{-4} with its maximum values during July, and the ϒ values vary from 1.2 to 1.9 with its maximum during the month of April (Figure 6.4). Whereas the α values of the Donelan spectrum varies from 1.3×10^{-3} to 5.9×10^{-3} with its maximum values during June and July and the ϒ values vary from 1.1 to 3.3 with its maximum during the month of July.

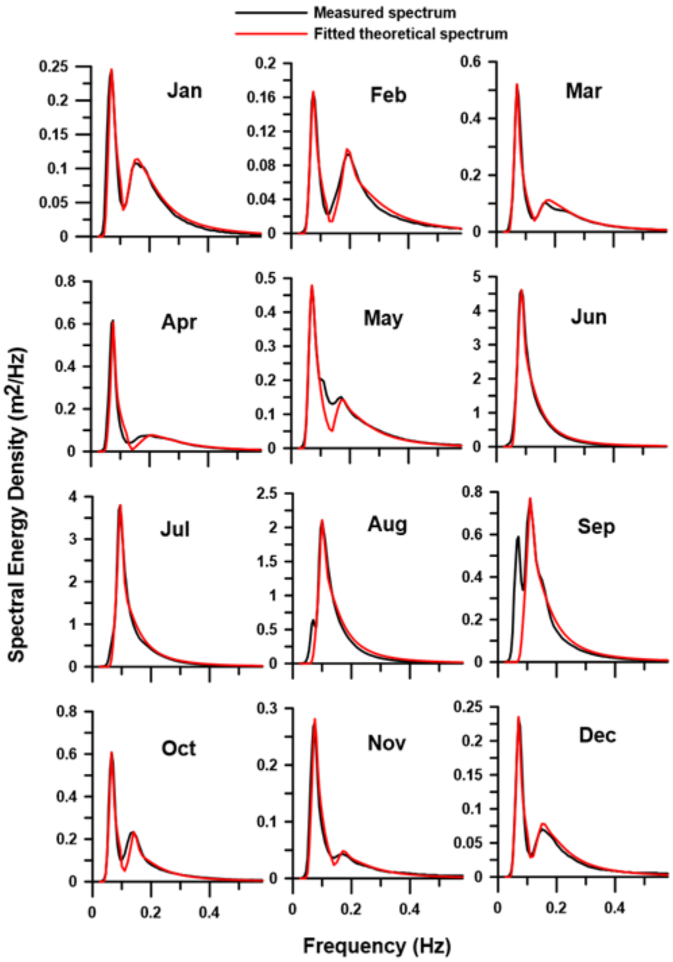

Months	JONSWAP		Donelan	
	α	ϒ	α	ϒ
Jan	1.8×10^{-5}	1.3	2.3×10^{-3}	1.1
Feb	1.6×10^{-5}	1.4	3.6×10^{-3}	1.6
Mar	3.1×10^{-5}	1.6	3.7×10^{-3}	1.1
Apr	4.3×10^{-5}	1.9	4.9×10^{-3}	1.1
May	3.8×10^{-5}	1.2	4.1×10^{-3}	1.3
Jun	9.6×10^{-4}	1.2	5.9×10^{-3}	1.8
Jul	9.8×10^{-4}	1.7	5.9×10^{-3}	2.3
Aug	6.6×10^{-4}	1.8	5.5×10^{-3}	1.7
Sep	4.4×10^{-4}	1.6	2.9×10^{-3}	1.7
Oct	2.5×10^{-5}	1.6	2.1×10^{-3}	1.9
Nov	2.7×10^{-5}	1.4	1.3×10^{-3}	1.4
Dec	1.4×10^{-5}	1.6	1.5×10^{-3}	1.2

Figure 6.4 Fitted theoretical wave spectrum to the monthly averaged measured spectrum during 2014 at Honnavar along with the estimated spectral parameters.

While comparing all three locations off the west coast, it can be seen that the values of α are high during the monsoon period. This is because α is a constant which is determined by the total wave energy and the energy of waves is high during the monsoon period.

6.3.4 Gangavaram

The theoretical wave spectrum fitted to the measured wave spectrum at the location Gangavaram shows some discrepancies during the months of November and December (Figure 6.5). The values of α and ϒ of the JONSWAP spectrum vary from 2.9×10^{-5} to 1.2×10^{-3} and 1.1 to 1.6. Unlike the other three locations off the west coast, here, the maximum value of α is not observed during the monsoon period. For Donelan, spectrum α varies from 4.2×10^{-4} to 8.8×10^{-3} and ϒ varies from 1.1 to 2.4. Maximum values of ϒ for Donelan spectra are observed during May.

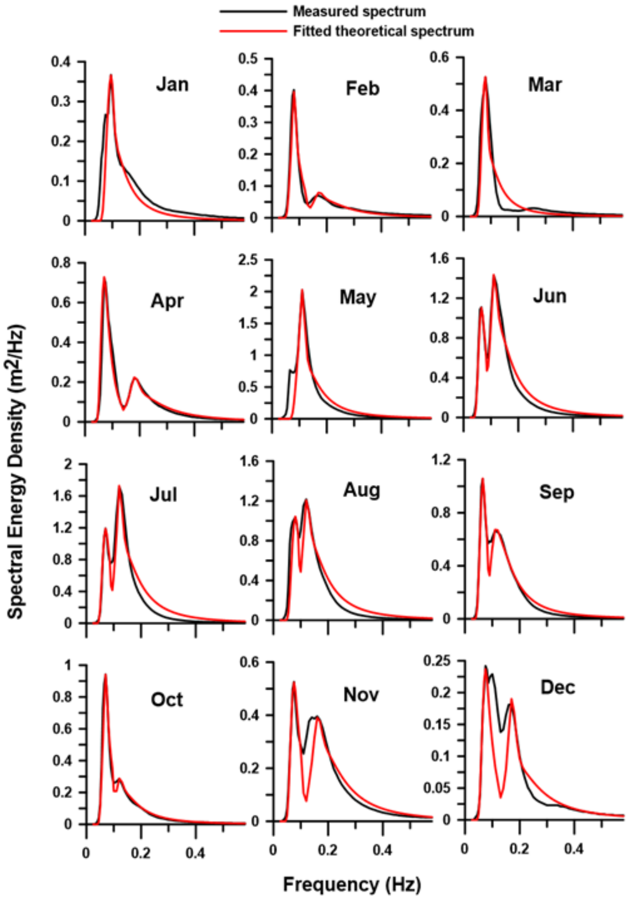

Months	JONSWAP		Donelan	
	α	ϒ	α	ϒ
Jan	1.5×10^{-4}	1.1	6.9×10^{-4}	1.9
Feb	4.6×10^{-5}	1.6	2.1×10^{-3}	1.4
Mar	9×10^{-5}	1.1	4.2×10^{-4}	2.2
Apr	6.3×10^{-5}	1.1	6.5×10^{-3}	1.6
May	1.2×10^{-3}	1.6	5.5×10^{-3}	2.4
Jun	6.6×10^{-5}	1.1	6.2×10^{-3}	1.5
Jul	1×10^{-4}	1.1	8.8×10^{-3}	1.8
Aug	1.8×10^{-4}	1.1	7.4×10^{-3}	1.5
Sep	5.8×10^{-5}	1.2	3.9×10^{-3}	1.1
Oct	6.4×10^{-5}	1.4	1.9×10^{-3}	1.4
Nov	6.4×10^{-5}	1.1	8.1×10^{-3}	1.4
Dec	2.9×10^{-5}	1.1	3.2×10^{-3}	2.2

Figure 6.5 Fitted theoretical wave spectrum to the monthly averaged measured spectrum during 2015 at Gangavaram along with the estimated spectral parameters.

6.3.5 Gopalpur

For the location Gopalpur, the theoretical wave spectrum matches well with the measured spectrum for all the months (Figure 6.6). The values of α and ϒ for the JONSWAP spectrum varies from 1.8×10^{-5} to 6.7×10^{-4} and from 1.1 to 1.6 respectively. The values of α are high from May to July. Whereas for Donelan spectrum, the α values vary between 4.7×10^{-4} and 1.8×10^{-2} and ϒ between 1.1 and 2.2. While comparing all the five locations, the maximum value of α for the Donelan spectrum is observed during April at Gopalpur.

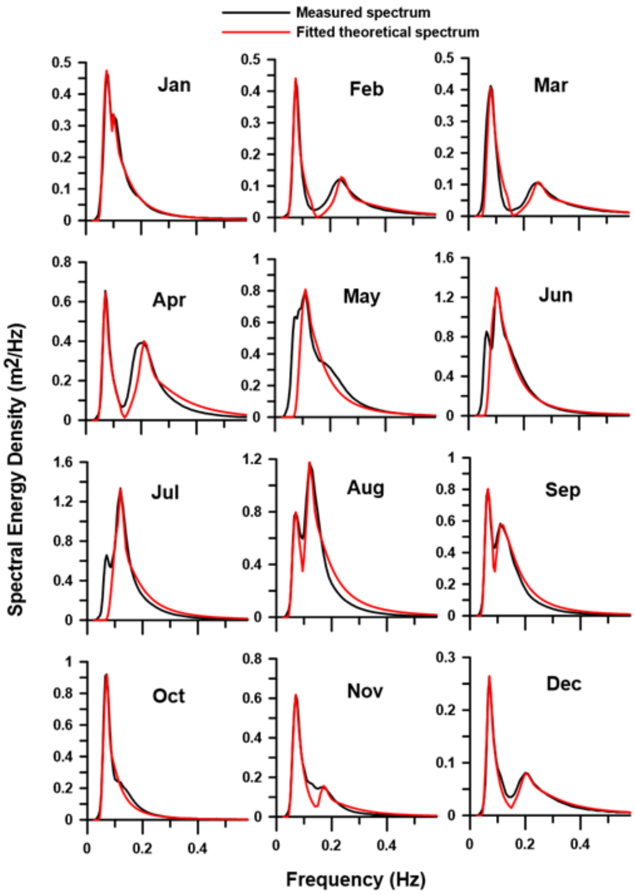

Months	JONSWAP		Donelan	
	α	ϒ	α	ϒ
Jan	5.8×10^{-5}	1.1	9.2×10^{-4}	1.6
Feb	3.7×10^{-5}	1.6	8.5×10^{-3}	2.2
Mar	6.3×10^{-5}	1.2	9.8×10^{-3}	1.9
Apr	4.4×10^{-5}	1.4	1.8×10^{-2}	1.9
May	6.7×10^{-4}	1.1	3.7×10^{-3}	1.4
Jun	4.5×10^{-4}	1.1	4.4×10^{-3}	1.3
Jul	6.6×10^{-4}	1.6	5.8×10^{-3}	2.1
Aug	6.9×10^{-5}	1.1	6.7×10^{-3}	1.6
Sep	4.8×10^{-5}	1.1	3.4×10^{-3}	1.1
Oct	7.9×10^{-5}	1.1	4.7×10^{-4}	2.1
Nov	4.9×10^{-5}	1.2	3×10^{-3}	1.9
Dec	1.8×10^{-5}	1.4	3.8×10^{-3}	1.5

Figure 6.6 Fitted theoretical wave spectrum to the monthly averaged measured spectrum during 2015 at Gopalpur along with the estimated spectral parameters.

6.4 Fitting theoretical wave spectra for waves at different water depths

Here theoretical wave spectrum is fitted to the measured wave spectrum at different water depths to find out the influence of water depth on the spectral shape and hence on the spectral parameters. The wave rider buoy data at three different water depths (5m, 9m, and 30m) off the location Honnavar along the west coast of India for the year 2015 is used in the study. The percentage of deep, shallow, and intermediate water waves for the three water depths were found out using d/L criteria (d=water depth, L=wave length). JONSWAP and Donelan spectra are fitted to the measured monthly averaged spectrum during June and July, and the spectral parameters are estimated. Table 6.1 shows the percentage of deep, shallow, and intermediate water waves present at the three water depths. Most of the waves observed at this location are shallow and intermediate water waves. At 5m depth, the percentage of shallow-water waves is high, whereas, at 9m, both shallow and intermediate water waves are present. Deep-water waves are very less at this location, and a very small percentage can be observed at 30m depth. There is a dominance of intermediate water waves at 30m depth where the shallow water waves are absent.

Table 6.1 Percentage of deep, shallow, and intermediate water waves

Depth	Month (2015)	Percentage of Shallow water waves $d/L_p < 0.05$	Percentage of Intermediate water waves $0.05 < d/L_p < 0.5$	Percentage of Deep water waves $d/L_p > 0.5$
5m	June	96.84	3.16	-
	July	100	-	-
9m	June	76.36	23.64	-
	July	34.61	65.39	-
30m	June	-	99.51	0.49
	July	-	100	-

Figure 6.7 shows the monthly averaged wave spectra fitted with the theoretical wave spectra for water depths 5m, 9m, and 30 m and the estimated spectral parameters. The spectra shown are for the months of June and July. Since it is the monsoon period and significant wave height and energy of the waves are very high, the measured spectral energy density is also very high, and it is single-peaked. From the figure, it is evident that the spectral energy density decreases as the depth decreases. For both the months, the maximum spectral energy observed is at 30m water depth (~ $5m^2/Hz$) which decreases at 9m depth, and it is the lowest at 5m depth. This decrease in the energy as depth decreases is because of the dissipation due to the effect of the bottom. There is no much variation in the peak frequency with respect to the depth, and it always lies around 0.1 Hz. From the figure, it can be seen that for the JONSWAP spectrum, the values of ϒ ranges from 1.1 to 2.3, whereas for the Donelan spectrum, the value of ϒ is between 1.6 and 2.09. Here the average values of α and ϒ for the JONSWAP spectrum observed are 9.37×10^{-4} and 1.6, respectively. A distinct variation in the spectral parameters with respect to depth is not observed here. Liu et al. (2017) found out that, in the South China Sea, during typhoon conditions, α decreases as water depth increases from 50m to 300m, whereas during non-typhoon conditions, α remained constant without varying according to the water depth. But in this study, α is not a constant though it is a non-typhoonic condition. It is discussed that, a stable spectral shape is caused by relatively constant wind energy input and the weak dissipations due to water breakings and bottom frictions. But in this study, since the water depth is less than 30m, the effect of dissipation

due to bottom friction is significant. Also, it was found that water depth doesn't have any influence on the Υ value.

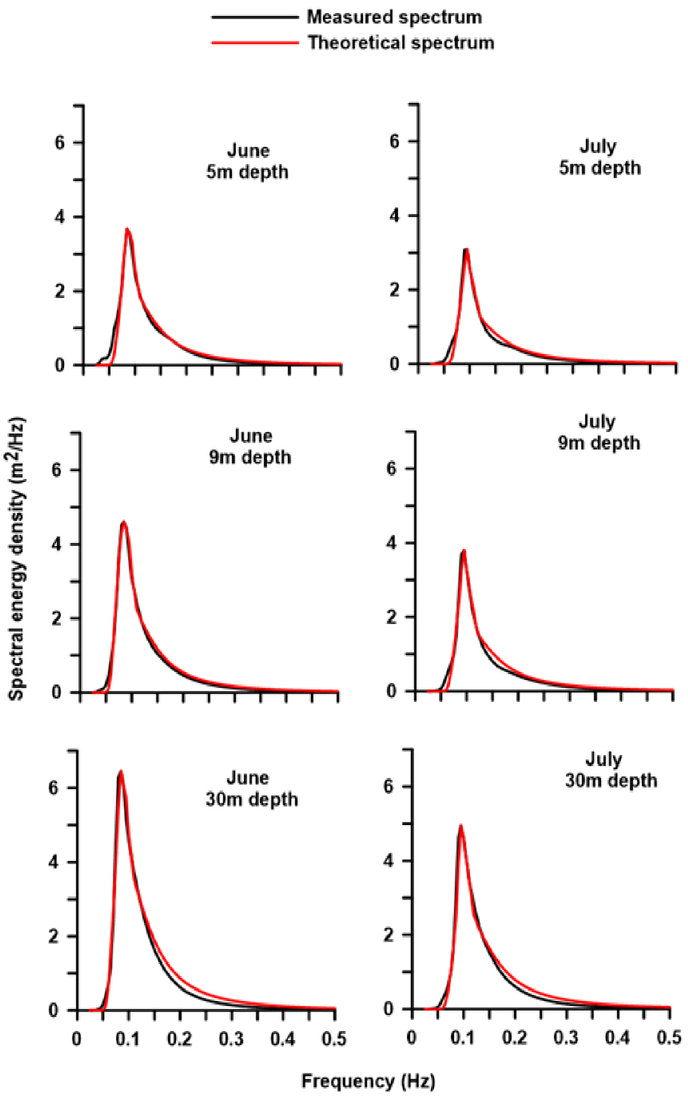

Depth	Month	Spectral parameters 2015			
		JONSWAP		Donelan	
		α	Υ	α	Υ
5m	**June**	**5.8×10^{-4}**	**1.6**	**5.4×10^{-3}**	**1.9**
	July	**9×10^{-4}**	**1.5**	**5.4×10^{-3}**	**2.1**
9m	**June**	**1.1×10^{-3}**	**1.1**	**6.6×10^{-3}**	**2**
	July	**1×10^{-3}**	**1.6**	**6.9×10^{-3}**	**2.1**
30m	**June**	**1.1×10^{-3}**	**1.5**	**1.1×10^{-2}**	**1.7**
	July	**9.4×10^{-4}**	**2.3**	**1.1×10^{-2}**	**1.9**

Figure 6.7 Theoretical wave spectrum fitted with the measured spectrum for different water depths

The slope of the high-frequency part of the wave spectrum at different water depths are given in Table 6.2. Here values of slope is in a range between 3.4 and 3.8. Like the spectral parameters the slope is also not changing according the variations in depth.

Table 6.2 Slope of the high frequency pat of the spectrum at different water depths

Depth	Exponent of high frequency tail (b)	
	Jun	Jul
5m	-3.80	-3.68
9m	-3.50	-3.46
30m	-3.46	-3.44

6.5 Fitting theoretical wave spectra to cyclone waves

Here JONSWAP spectrum is fitted to the single-peaked wave spectrum generated during the cyclone period. The measured wave spectrum at the locations Gopalpur and Karwar, off the east and west coast of India during the two cyclones, PHAILIN and KYARR, respectively, are used for spectral fitting. Figure 6.8 shows the theoretical wave spectrum fitted with the measured wave spectrum during the various stages of cyclone PHAILIN. It can be seen that JONSWAP spectra with modified parameters describe the wave spectra well at low frequencies and high frequencies, except when the spectrum is multimodal as in figure 6.8a &c. This is because JONSWAP spectrum fits well for the unimodal spectrum. The values for ϒ are found to be increasing as the spectral peak energy increases due to cyclones. The maximum value of ϒ obtained is 3.3 on 12 Oct, when the impact of the cyclone on the wave spectrum is the highest. But the maximum value of α is observed on 13 Oct (1×10^{-2}). Figure 6.9 shows the fitted theoretical wave spectrum and the estimated spectral parameters during the cyclone KYARR. As there are two spectral peaks in figure 6.9f, the second peak is considered for spectral fitting because JONSWAP spectrum can be used only for single-peaked spectrum. Here the maximum values of α and ϒ obtained are on 25 Oct 06:30 Hrs, when the wave energy density is maximum due to cyclone ($\alpha = 6.3\times10^{-3}$, ϒ = 3). The value of α and ϒ observed during the cyclone period are higher than the values observed during the normal conditions.

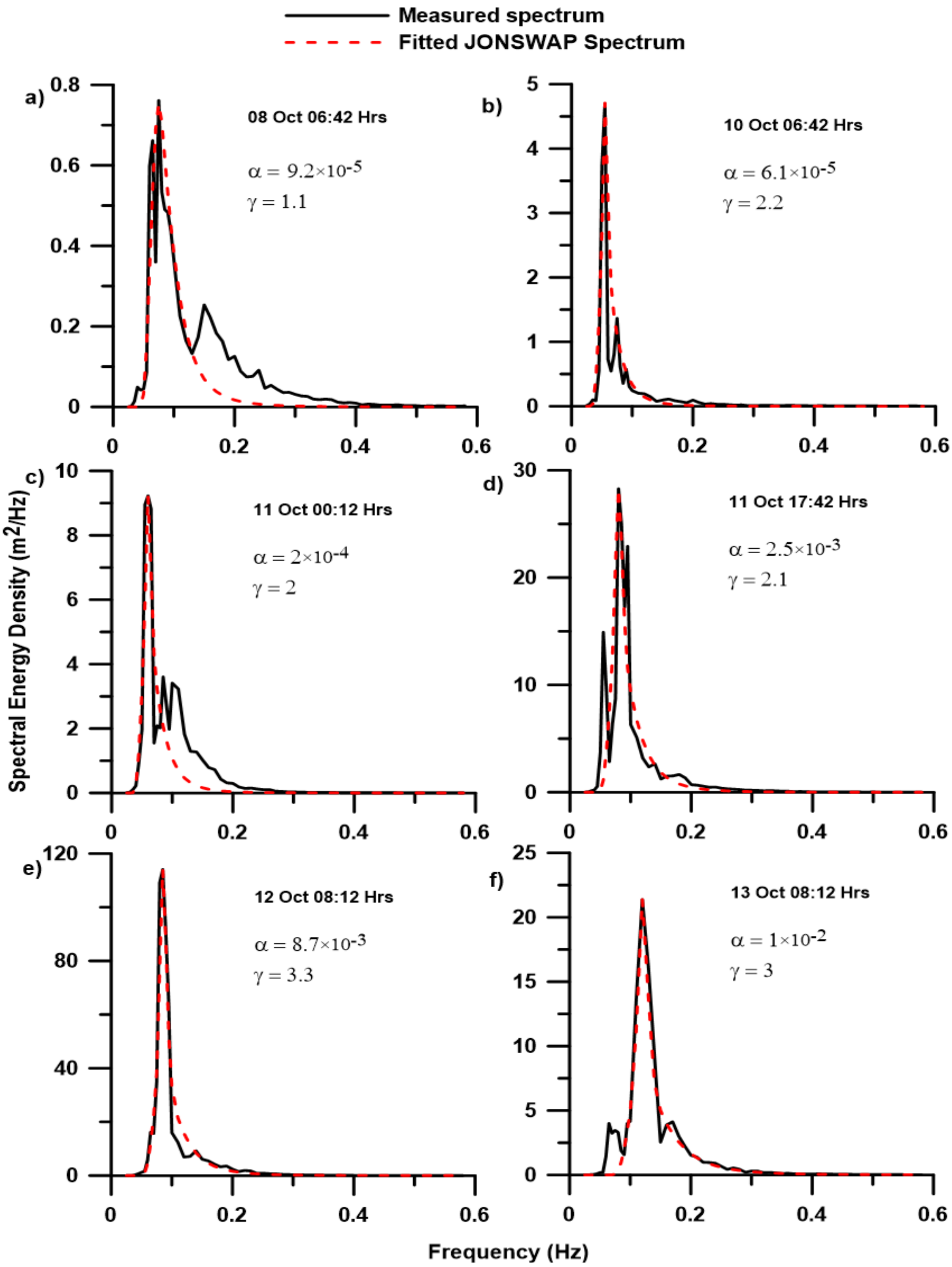

Figure 6.8 Theoretical wave spectrum fitted with the measured spectrum during the cyclone PHAILIN

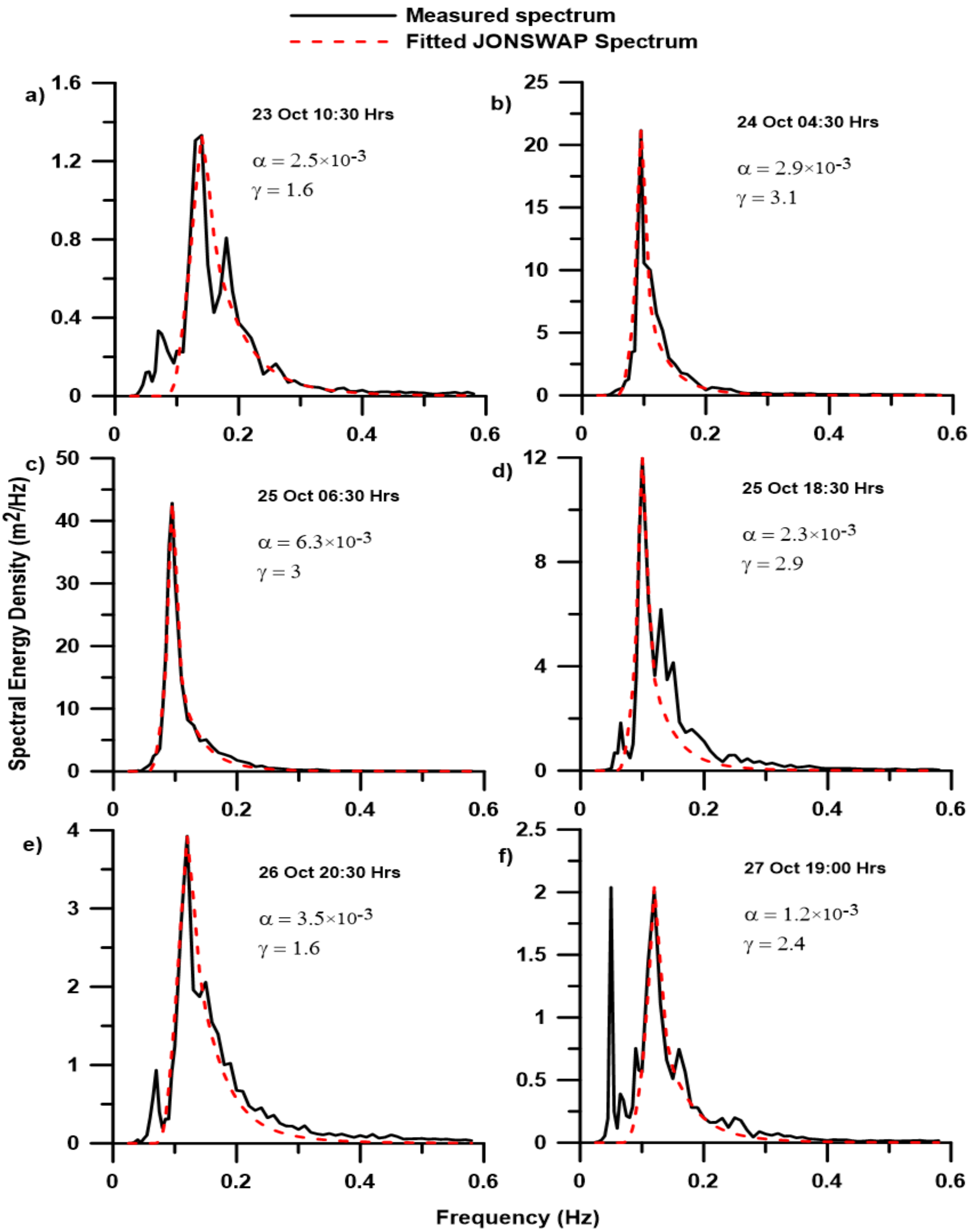

Figure 6.9 Theoretical wave spectrum fitted with the measured spectrum during the cyclone KYARR

The JONSWAP study (Hasselmann et al. 1973) proposed that α shows a dependence on the non-dimensional peak frequency through the following equation.

$$\alpha = 0.033\mathrm{v}^{0.67} \tag{6.1}$$

Here v is the non-dimensional peak frequency which depends on the wind speed and the peak frequency of the wave spectrum.

$$\mathrm{v} = \frac{f_p U_{10}}{g} \tag{6.2}$$

Young (2003) found out that the α values of the JONSWAP spectrum for the Hurricane waves (both wind-sea and swell) depend on the non-dimensional peak frequency and hence on the wind speed as suggested by Hasselmann et al.(1973). Whereas the ϒ values for the Hurricane waves are smaller than the JONSWAP values, and a mean value of 1.9 is suggested for the hurricane waves. In this study, the maximum value of ϒ observed during both the cyclones PHAILIN and KYARR agrees more with the value suggested by the JONSWAP study. Here the α value increases as the intensity of the cyclone increases showing its dependence on the wind speed.

Chapter 7: Summary and Conclusion

Spectral description of sea-state is an important factor in the design of marine structures as well as climatic studies. As the sea-state consists of one or more wind-sea or swell systems, only the spectral representation provides information about the different wave systems present at a location. The physical processes that influence the wave spectrum include local events like sea/land breeze systems and extreme events like tropical cyclones. This study provides a detailed description on the wave spectral characteristics and its evolution in the coastal waters of the east and west coasts of India by focusing on the impact of sea breeze and land breeze systems and tropical cyclones, in this process.

The wave spectral characteristics studied off the east and west coasts of India show that the wave spectra off the west coast of India are single-peaked during the monsoon period with the dominance of SW swells generated by monsoon winds and double-peaked during the non-monsoon period with long-period swells generated in the Southern Indian Ocean and wind-sea generated by the local winds. The wave spectra observed off the east coast of India are double-peaked during most of the time, including the monsoon period showing that long-period swells co-exist with the swells generated by the monsoon winds during the monsoon period. Long-period swells (T_p ~ 18 to 22 s), which are the swells generated in the Southern Ocean, are observed in all the locations. Due to the influence of the sea and land breeze, diurnal variations are observed in the wind-sea region of the spectra, especially during the non-monsoon period with high variation in the east coast compared to the west. The inter-annual variation observed in the swell part of the wave spectrum was due to many factors, including the strength of the SW monsoon, early onset of monsoon, and depressions or cyclones formed in the Arabian Sea and Bay of Bengal. In contrast, the variation in the wind-sea part of the spectrum was due to the variation in local winds and sea breeze. The exponent of high-frequency tail (slope) of the spectrum obtained for all the five locations for the year 2015 shows that the slope is steep (~ -3) during the monsoon time.

The evolution of the wave spectrum according to the changes in the wind system during a sea-land breeze cycle is examined by focusing on the source terms involved. The energy from wind input is present only when the wind speed due to sea breeze is significantly high and it is transferred to the lower frequency bin through non-linear interactions. There is no energy from wind input during the land-breeze phase since the wind speed is very low and hence the influence of land breeze on wave spectrum is not significant. It is only through non-linear interactions energy is transferred between different frequency bins during the land-breeze phase. The influence of white-capping observed is negligibly small in the evolution process.

The characteristics of wave spectrum at the near-shore and deep waters during the growth and decay of tropical cyclones off the east and west coasts of India are studied using the wave data during two cyclones PHAILIN and KYARR. The measured wave spectra partitioned at the near-shore waters show that a swell system propagating from the cyclone generation region, shore region, super-imposes with the pre-existing swells in the near-shore region to form a high energy single-peaked spectrum during the cyclone. The slope of the wave spectrum becomes steep (exponent ~ -4) during cyclone. The directional wave spectra observed near the eye and north, west, east and south of the cyclone has two separate peaks representing swells and wind-sea, where wind-sea direction aligns with the direction of the cyclone. In deep waters, waves generated due to tropical cyclones are young wind-sea and the youngest of waves are found in the left front and left back quadrants. The resulting wave-field generated by cyclonic winds in deep waters, do not exactly follow the wind field, and it has a dependence on the forward motion and the translation speed of the cyclone.

The combination of JONSWAP and Donelan spectrum with modified parameters describes the wave spectrum off the east and west coast of India. The values of α for JONSWAP spectrum lie within the range 1×10^{-5} to 1.2×10^{-3} and ϒ between 1.1 and 2.8. The values of α for Donelan spectrum varies between 4×10^{-4} and 1.8×10^{-2} and ϒ between 1.1 and 2.5. Most of the waves observed at the study location are shallow and intermediate water waves and the percentage of deep-water waves is very less. The spectral parameters of the wave spectrum at different water depths are similar. Wave spectrum during extreme wave conditions like cyclones can be better represented by the JONSWAP spectrum with modified parameters. The values of ϒ during the cyclone period are high (ϒ ≥ 3), whereas before and after cyclone ϒ values are in the range 1 to 2. The values of α obtained lie in the range 5×10^{-4} to 6×10^{-3}.

Scope for future studies

- Simulating waves with measured wind data during the sea-breeze cycle instead of modelled wind data.
- The dependence of JONSWAP spectral parameters on fetch and wind speed can be examined.
- Derivation of a theoretical wave spectra for multi-peaked spectrum

References

Abbs, D.J. and William, L., 1992. Sea-breeze observations and modelling: a review. sea, 50, p.95s.

Aboobacker, V.M., Rashmi, R., Vethamony, P. and Menon, H.B., 2011. On the dominance of pre-existing swells over wind seas along the west coast of India. Continental Shelf Research, 31(16), pp.1701-1712.

Aboobacker, V.M., Seemanth, M., Samiksha, S.V., Sudheesh, K., Kerkar, J. and Vethamony, P., 2014. Sea breeze-induced wind sea growth in the central west coast of India. Ocean engineering, 84, pp.20-28.

Alves, J.-H.G.M., Banner, M.L., 2003. Performance of a saturation-based dissipation-rate source term in modeling the fetch-limited evolution of wind waves. Journal of Physical Oceanography 33, 1274–1298.

Amrutha, M.M., Sanil Kumar, V. and Singh, J., 2016, February. Changes in nearshore waves during the active sea/land breeze period off Vengurla, central west coast of India. In Annales Geophysicae (Vol. 34, No. 2, pp. 215-226). Copernicus GmbH.

Amrutha, M.M., Sanil Kumar, V., Anoop, T.R., Nair, B., Nherakkol, A. and Jeyakumar, C., 2014, September. Waves off Gopalpur, northern Bay of Bengal during cyclone Phailin. In Annales Geophysicae (Vol. 32, No. 9, pp. 1073-1083). Copernicus GmbH.

Anoop, T.R., Kumar, V.S. and Shanas, P.R., 2014. Spatial and temporal variation of surface waves in shallow waters along the eastern Arabian Sea. Ocean Engineering, 81, pp.150-157.

Aparna, M., Shetye, S.R., Shankar, D., Shenoi, S.S.C., Mehra, P. and Desai, R.G.P., 2005. Estimating the seaward extent of sea breeze from QuikSCAT scatterometry. Geophysical Research Letters, 32(13).

Ardhuin, F., Herbers, T.H.C. and Watts, K.P., GP vanVledder, R. Jensen, and H. Graber (2007). Swell and slanting fetch effects on wind wave growth, J. Phys. Oceanogr, 37(4), pp.908-931.

Babanin, A.V., Hsu, T.W., Roland, A., Ou, S.H., Doong, D.J. and Kao, C.C., 2011. Spectral wave modelling of Typhoon Krosa. Natural Hazards and Earth System Sciences, 11(2), p.501.

Badulin, S.I., Babanin, A.V., Zakharov, V.E. and Resio, D., 2007. Weakly turbulent laws of wind-wave growth. Journal of Fluid Mechanics, 591, pp.339-378.

Booij, N.R.R.C., Ris, R.C. and Holthuijsen, L.H., 1999. A third-generation wave model for coastal regions: 1. Model description and validation. Journal of geophysical research: Oceans, 104(C4), pp.7649-7666.

Bouws, E., Günther, H., Rosenthal, W. and Vincent, C.L., 1985. Similarity of the wind wave spectrum in finite depth water: 1. Spectral form. Journal of Geophysical Research: Oceans, 90(C1), pp.975-986.

Bouws, E., Komen, G.J., 1983. On the balance between growth and dissipation in an extreme depth-limited wind-sea in the southern North Sea. J. Phys. Oceanogr. 13 (9), 1653–1658.

Cavaleri, L., Alves, J.H., Ardhuin, F., Babanin, A., Banner, M., Belibassakis, K., Benoit, M., Donelan, M., Groeneweg, J., Herbers, T.H.C. and Hwang, P.A.E.M., 2007. Wave modelling–the state of the art. Progress in oceanography, 75(4), pp.603-674.

Cavaleri, L., Fox-Kemper, B. and Hemer, M., 2012. Wind waves in the coupled climate system. Bulletin of the American Meteorological Society, 93(11), pp.1651-1661.

Chakrabarti, S., 2005. Handbook of Offshore Engineering (2-volume set). Elsevier.

Chen, G., Chapron, B., Ezraty, R. and Vandemark, D., 2002. A global view of swell and wind sea climate in the ocean by satellite altimeter and scatterometer. Journal of Atmospheric and Oceanic Technology, 19(11), pp.1849-1859.

Chu, P.C. and Cheng, K.F., 2008. South China Sea wave characteristics during Typhoon Muifa passage in winter 2004. Journal of Oceanography, 64(1), pp.1-21.

Dattatri, J., Raman, H. and Shankar, N.J., 1977. Comparison of Scott spectra with ocean wave spectra. Journal of the Waterway, Port, Coastal and Ocean Division, 103(3), pp.375-378.

Donelan, M.A. and Pierson Jr, W.J., 1987. Radar scattering and equilibrium ranges in wind-generated waves with application to scatterometry. Journal of Geophysical Research: Oceans, 92(C5), pp.4971-5029.

Donelan, M.A. and Yuan, Y., 1994. Wave dissipation by surface processes. Dynamics and Modelling of Ocean Waves, pp.143-155.

Donelan, M.A., Hamilton, J. and Hui, W., 1985. Directional spectra of wind-generated ocean waves. Philosophical Transactions of the Royal Society of London. Series A, Mathematical and Physical Sciences, 315(1534), pp.509-562.

Douglas, C. and Voulgaris, G., 2019, WavePART: MATLAB(r) software for the partition of directional ocean wave spectra.: Zenodo, doi:10.5281/zenodo.2638500

Dube, S.K., Rao, A.D., Sinha, P.C., Murty, T.S. and Bahulayan, N., 1997. Storm surge in the Bay of Bengal and Arabian Sea the problem and its prediction. Mausam, 48(2), pp.283-304.

Fan, Y., Ginis, I. and Hara, T., 2009. The effect of wind–wave–current interaction on air–sea momentum fluxes and ocean response in tropical cyclones. Journal of Physical Oceanography, 39(4), pp.1019-1034.

Feng, W.B., Yang, B., Cao, H.J. and Ni, X.Y., 2012. Study on wave spectra in south coastal waters of Jiangsu. In Applied Mechanics and Materials (Vol. 212, pp. 193-200). Trans Tech Publications Ltd.

Forristall, G.Z., 1981. Measurements of a saturated range in ocean wave spectra. Journal of Geophysical Research: Oceans, 86(C9), pp.8075-8084.

Francis, J.R.D., 1949. Laboratory experiments on wind-generated waves. J. Mar. Res, 8(2), pp.120-131.

Gagnaire-Renou, E., Benoit, M. and Forget, P., 2010. Ocean wave spectrum properties as derived from quasi-exact computations of nonlinear wave-wave interactions. Journal of Geophysical Research: Oceans, 115(C12).

Glejin, J., Sanil Kumar, V., Nair, B. and Singh, J., 2013. Influence of winds on temporally varying short and long period gravity waves in the near shore regions of the eastern Arabian Sea. Ocean Science, 9(2), pp.343-353.

Gunson, J. and Symonds, G., 2014. Spectral evolution of nearshore wave energy during a sea-breeze cycle. Journal of Physical Oceanography, 44(12), pp.3195-3208.

Hanson, J.L. and Phillips, O.M., 2001. Automated analysis of ocean surface directional wave spectra. Journal of atmospheric and oceanic technology, 18(2), pp.277-293.

Hasselmann, D.E., Dunckel, M. and Ewing, J.A., 1980. Directional wave spectra observed during JONSWAP 1973. Journal of physical oceanography, 10(8), pp.1264-1280.

Hasselmann, K., Barnett, T.P., Bouws, E., Carlson, H., Cartwright, D.E., Enke, K., Ewing, J.A., Gienapp, H., Hasselmann, D.E., Kruseman, P. and Meerburg, A., 1973. Measurements of wind-wave growth and swell decay during the Joint North Sea Wave Project (JONSWAP). Ergänzungsheft 8-12.

Hasselmann, S., Hasselmann, K., Allender, J.H., Barnett, T.P., 1985. Computations and parameterizations of the nonlinear energy transfer in a gravity-wave spectrum, Part II. J. Phys. Oceanogr., 15, 1378–1391.

Hersbach, H. and Dee, D. (2016) ERA5 reanalysis is in production. ECMWF Newsletter 622 147.7.

Holthuijsen, L.H., 2007. Waves in oceanic and coastal waters. Cambridge University Press, Cambridge. ISBN, 978-0521860284

Hughes, S.A., 1984. The TMA shallow-water spectrum description and applications. Technical Report. CERC 87 -7, U.S Army Corps of Engrs. (USAECE) Wtrwy. Experiment Station, Vicksburg, Miss.

Hwang, P.A., García-Nava, H. and Ocampo-Torres, F.J., 2011. Dimensionally consistent similarity relation of ocean surface friction coefficient in mixed seas. Journal of Physical oceanography, 41(6), pp.1227-1238.

Hwang, P.A., Walsh, E.J., 2016. Azimuthal and radial variation of wind-generated surface waves inside tropical cyclones. Journal of Physical Oceanography, 46(9), 2605-2621. https://doi.org/10.1175/JPO-D-16-0051.1

IMD, 2012. Annual Report 2012. Indian Meteorological Department. Ministry of Earth Sciences, Government of India.

IMD, 2013. Report on cyclonic distribution over the North Indian Ocean during 2013. Indian Meteorological Department. Ministry of Earth Sciences, Government of India. http://www.rsmcnewdelhi.imd.gov.in/uploads/report/27/27_14ab8f_rsmc-2013.pdf

IMD, 2019. Cyclonic storms and Depressions over the north Indian Ocean during 2019. Indian Meteorological Department. Ministry of Earth Sciences, Government of India.

Kahma, K.K., 1981. A study of the growth of the wave spectrum with fetch. Journal of Physical Oceanography, 11(11), pp.1503-1515.

Kawai, S., Okada, K. and Toba, Y., 1977. Field data support of three-seconds power law andgu* σ− 4-spectral form for growing wind waves. Journal of the Oceanographical Society of Japan, 33(3), pp.137-150.

King, D.B., Shemdin, O.H., 1978. Radar observation of hurricane wave directions. In Coastal Engineering 1978, 209-226. https://doi.org/10.1061/9780872621909.012

Kitaigordskii, S. A., Krasitskii, V. P. and Zaslavskii, M. M. , 1975. On Phillips's theory of equilibrium range in the spectra of wind-generated gravity waves. J. Phys. Oceanogr, 5, 410–420.

Komen, G.J., Hasselmann, S., Hasselmann, K., 1984. On the existence of a fully developed wind-sea spectrum. Journal of Physical Oceanography.14, 1271–1285.

Kumar, B.P. and Stone, G.W., 2007. Numerical simulation of typhoon wind forcing in the Korean seas using a spectral wave model. Journal of Coastal Research, 23(2 (232)), pp.362-373.

Kumar, V.S. and Kumar, K.A., 2008. Spectral characteristics of high shallow water waves. Ocean Engineering, 35(8-9), pp.900-911.

Kumar, V.S., Dubhashi, K.K. and Nair, T.B., 2014b. Spectral wave characteristics off Gangavaram, Bay of Bengal. Journal of Oceanography, 70(3), pp.307-321.

Kumar, V.S., Johnson, G., Dora, G.U., Chempalayil, S.P., Singh, J. and Pednekar, P., 2012. Variations in nearshore waves along Karnataka, west coast of India. Journal of earth system science, 121(2), pp.393-403.

Kumar, V.S., Shanas, P.R. and Dubhashi, K.K., 2014a. Shallow water wave spectral characteristics along the eastern Arabian Sea. Natural hazards, 70(1), pp.377-394.

Liu, A.K., Jackson, F.C., Walsh, E.J. and Peng, C.Y., 1989. A case study of wave-current interaction near an oceanic front. Journal of Geophysical Research: Oceans, 94(C11), pp.16189-16200.

Liu, Y., Li, S., Yi, Q. and Chen, D., 2017. Wind profiles and wave spectra for potential wind farms in South China Sea. Part II: Wave spectrum model. Energies, 10(1), p.127.

Long, C.E. and Resio, D.T., 2007. Wind wave spectral observations in currituck sound, north carolina. Journal of Geophysical Research: Oceans, 112(C5).

Longuet-Higgins, M.S., 1952. On the statisticaldistribution of the height of sea waves. JMR, 11, pp.245-266.

Masselink, G. and Pattiaratchi, C., 1998. Morphodynamic impact of sea breeze activity on a beach with beach cusp morphology. Journal of Coastal Research, pp.393-406.

Masselink, G., 1998. The effect of sea breeze on beach morphology, surf zone hydrodynamics and sediment resuspension. Marine Geology, 146(1-4), pp.115-135.

Miles, J.W., 1957. On the generation of surface waves by shear flows. Journal of Fluid Mechanics, 3(2), pp.185-204.

Miles, J.W., 1960. On the generation of surface waves by turbulent shear flows. Journal of Fluid Mechanics, 7(3), pp.469-478.

Mitsuyasu, H., 1968. On the growth of the spectrum of wind-generated waves, I. Rept. Res. Inst. Appl. Mech., Kyushu Univ., 16, pp.459-465.

Mitsuyasu, H., 1969. On the growth of the spectrum of wind-generated waves, Part II. Rept. Res. Inst. Appl. Mech., Kyushu Univ., 17, pp.235-243.

Mitsuyasu, H., Tasai, F., Suhara, T., Mizuno, S., Ohkusu, M., Honda, T. and Rikiishi, K., 1975. Observations of the directional spectrum of ocean WavesUsing a cloverleaf buoy. Journal of Physical Oceanography, 5(4), pp.750-760.

Munk, W.H., 1951. Ocean waves as a meteorological tool. In Compendium of Meteorology (pp. 1090-1100). American Meteorological Society, Boston, MA.

Narasimhan, S. and Deo, M.C., 1979. Spectral analysis of ocean waves-a study. Proceedings of the conference on civil engineering in oceans, vol 1. ASCE, New York, pp 877–892

Neetu, S., Shetye, S. and Chandramohan, P., 2006. Impact of sea breeze on wind-seas off Goa, west coast of India. Journal of Earth System Science, 115(2), pp.229-234.

Neumann, G., 1953. On ocean wave spectra and a new method of forecasting wind generated sea.

Ochi, M.K. and Hubble, E.N., 1976. Six-parameter wave spectra. In Coastal Engineering 1976 (pp. 301-328).

Ochi, M.K., 1993. On hurricane-generated seas. In Ocean wave measurement and analysis (pp. 374-387). ASCE.

Ochi, M.K., 2005. Ocean waves: the stochastic approach (Vol. 6). Cambridge University Press.

Parvathy, K.G., Umesh P.A. and Prasad K.B., 2017. Inter-seasonal variability of wind-waves and their attenuation characteristics by mangroves in a reversing wind system. International Journal of Climatology, 37(15), pp.5089-5106.

Pattiaratchi, C. and GOULD, B.H.J., 1997. Impact of sea-breeze activity on nearshore and foreshore processes in. Continental Shelf Research, 17(13), pp.1539-1560.

Phillips, O.M., 1957. On the generation of waves by turbulent wind. Journal of fluid mechanics, 2(5), pp.417-445.

Phillips, O.M., 1958. The equilibrium range in the spectrum of wind-generated waves. Journal of Fluid Mechanics, 4(4), pp.426-434.

Phillips, O.M., 1985. Spectral and statistical properties of the equilibrium range in wind-generated gravity waves. Journal of Fluid Mechanics, 156, pp.505-531.

Phillips, W.J., Graves, R.W. and Flumerfelt, R.W., 1980. Experimental studies of drop dynamics in shear fields: role of dynamic interfacial effects. Journal of Colloid and Interface Science, 76(2), pp.350-370.

Pierson, W.J. and Moskowitz, L., 1964. A proposed spectral form for fully developed wind seas based on the similarity theory of SA Kitaigorodskii. Journal of geophysical research, 69(24), pp.5181-5190..

Pierson, W.J., 1952. A unified mathematical theory for the analysis, propagation and refraction of storm-generated ocean surface waves, Part 1 and 2. NYU, Coll. of Eng., Res. Div., 461.

Portilla, J., Ocampo-Torres, F.J. and Monbaliu, J., 2009. Spectral partitioning and identification of wind sea and swell. Journal of atmospheric and oceanic technology, 26(1), pp.107-122.

Prasad, K.B., Nayak, S., Bonthu, S.R., Murty, P.L. and Sen, D., 2013. Performance and validation of a coupled parallel ADCIRC–SWAN model for THANE cyclone in the Bay of Bengal. Environmental Fluid Mechanics, 13(6), pp.601-623.

Remya, P.G. and Kumar, R., 2013. Impact of diurnal variation of winds on coastal waves off South East Coast of India. The International Journal of Ocean and Climate Systems, 4(3), pp.171-179.

Ris, R.C., Holthuijsen, L.H. and Booij, N., 1999. A third-generation wave model for coastal regions: 2. Verification. Journal of Geophysical Research: Oceans, 104(C4), pp.7667-7681.

Rogers, W.E., Hwang, P.A., Wang, D.W., 2003. Investigation of wave growth and decay in the SWAN model: three regional-scale applications. J. Phys. Oceanogr. 33 (2), 366–389. doi:10.1175/1520-0485(2003)0332.0.co;2.

Rusu, L., Pilar, P. and Soares, C.G., 2008. Hindcast of the wave conditions along the west Iberian coast. Coastal Engineering, 55(11), pp.906-919.

Sandhya, K.G., Nair, T.B., Bhaskaran, P.K., Sabique, L., Arun, N. and Jeykumar, K., 2014. Wave forecasting system for operational use and its validation at coastal Puducherry, east coast of India. Ocean Engineering, 80, pp.64-72.

Sanil Kumar, V. and Anjali Nair, M., 2015. Inter-annual variations in wave spectral characteristics at a location off the central west coast of India. In Annales Geophysicae (Vol. 33, No. 2, pp. 159-167). Copernicus GmbH.

Scott, J.R., 1965. A sea spectrum for model tests and long-term ship prediction. Journal of ship research, 9(04), pp.145-152.

Semedo, A., Sušelj, K., Rutgersson, A. and Sterl, A., 2011. A global view on the wind sea and swell climate and variability from ERA-40. Journal of Climate, 24(5), pp.1461-1479.

Siadatmousavi, S.M., Jose, F. and Stone, G.W., 2012. On the importance of high frequency tail in third generation wave models. Coastal Engineering, 60, pp.248-260.

Skamarock, W.C., Klemp, J.B., Dudhia, J., Gill, D.O., Barker, D.M., Wang, W. and Powers, J.G., 2008. A description of the Advanced Research WRF version 3. NCAR Technical note-475+ STR.

Soares, C.G., 1991. On the occurence of double peaked wave spectra. Ocean Engineering, 18(1-2), pp.167-171.

Soomere, T., 2008. Extremes and decadal variations of the northern Baltic Sea wave conditions. In Extreme Ocean Waves (pp. 139-157). Springer, Dordrecht.

Sverdrup, H.U. and Munk, W.H., 1947. Wind sea and swell, theory of relations for forecasting, US Navy Hydrographic Office. Techn. Report in Oceanography, (1), pp.1-44.

Thompson, E.F. and Vincent, C.L., 1983. Prediction of wave height in shallow water. In Coastal Structures' 83 (pp. 1000-1007). ASCE.

Toba, Y., 1973. Local balance in the air-sea boundary processes. Journal of the Oceanographical Society of Japan, 29(5), pp.209-220.

Umesh, P.A., 2015. Validation and Inter-comparison of Wave Hindcasts Using Third Generation Models in the North Indian Ocean (Ph.D. Thesis). Naval Physical and Oceanographic Laboratory, DRDO, Cochin, India, p. 499.

Umesh, P.A., Bhaskaran, P.K., Sandhya, K.G. and Nair, T.B., 2017. An assessment on the impact of wind forcing on simulation and validation of wave spectra at coastal Puducherry, east coast of India. Ocean Engineering, 139, pp.14-32.

Ursell, F., 1956. Wave generation by wind. Surveys in mechanics, pp.216-249.

van der Westhuysen, A.J., Zijlema, M., Battjes, J.A., 2007. Nonlinear saturation-based whitecapping dissipation in SWAN for deep and shallow water. Coast Eng. 54 (2), 151–170. doi:10.1016/j.coastaleng.2006.08.006.

Vethamony, P., Aboobacker, V.M., Menon, H.B., Kumar, K.A. and Cavaleri, L., 2011. Superimposition of wind seas on pre-existing swells off Goa coast. Journal of Marine Systems, 87(1), pp.47-54.

Wuest, W., 1949. Beitrag zur Entstehung von Wasserwellen durch Wind. ZAMM-Journal of Applied Mathematics and Mechanics/Zeitschrift für Angewandte Mathematik und Mechanik, 29(7-8), pp.239-252.

Xu, F., Perrie, W., Toulany, B. and Smith, P.C., 2007. Wind-generated waves in Hurricane Juan. Ocean Modelling, 16(3-4), pp.188-205.

Yan, L., 1987. An improved wind input source term for third generation ocean wave modelling. De Bilt, The Netherlands: KNMI.

Young, I.R and Babanin, A.V. eds., 2020. Ocean Wave Dynamics. World Scientific.

Young, I.R. and Babanin, A.V., 2006. Spectral distribution of energy dissipation of wind-generated waves due to dominant wave breaking. Journal of Physical Oceanography, 36(3), pp.376-394.

Young, I.R. and Verhagen, L.A., 1996. The growth of fetch limited waves in water of finite depth. Part 2. Spectral evolution. Coastal Engineering, 29(1-2), pp.79-99.

Young, I.R., 1998. Observations of the spectra of hurricane generated waves. Ocean Engineering, 25(4-5), pp.261-276.

Young, I.R., 2003. A review of the sea state generated by hurricanes. Marine structures, 16(3), pp.201-218.

Young, I.R., 2006. Directional spectra of hurricane wind waves. Journal of Geophysical Research: Oceans, 111(C8).

Zhang, L., Oey, L., 2019. An observational analysis of ocean surface waves in tropical cyclones in the western North Pacific Ocean. Journal of Geophysical Research: Oceans, 124(1), 184-195. https://doi.org/10.1029/2018JC014517

Zijlema, M., Van Vledder, G.P., Holthuijsen, L.H., 2012. Bottom friction and wind drag for wave models. Coast Eng. 65, 19–26. doi:10.1016/j.coastaleng.2012.03.002.

List of publications from thesis

Nair, M.A. and Kumar, V.S., 2016. Spectral wave climatology off Ratnagiri, northeast Arabian Sea. Natural Hazards, 82(3), pp.1565-1588.

Anjali Nair, M. and Sanil Kumar, V., 2017. Wave spectral shapes in the coastal waters based on measured data off Karwar on the western coast of India. Ocean Science, 13(3), pp.365-378.

Nair, M.A., Kumar, V.S. and Amrutha, M.M., 2018. Spectral wave characteristics in the near-shore waters of northwestern Bay of Bengal. Pure and Applied Geophysics, 175(8), pp.3111-3136.

Nair, M.A., Kumar, V.S. and George, V., 2021. Evolution of wave spectra during sea breeze and tropical cyclone. Ocean Engineering, 219, article number 108341.

Conferences in which the findings from thesis research were presented

Anjali Nair, M. and Sanil Kumar,V. "Growth and decay of wave spectrum during tropical cyclone Hudhud". Proceedings of 6th National Conference on Coastal, Harbour and Ocean Engineering, INCHOE-2018, CWPRS, Pune, 26-28 Sepetember, 2018.

Anjali Nair, M et al. "Evolution of wave spectra during sea breeze event – study based on numerical model". Proceedings of the Ocean Society of India Conference (OSICON–19), CMLRE (MoES), Kochi, 12-14 December, 2019.